SuperCam calibration targets on board the perseverance rover: Fabrication and quantitative characterization

Agnès Cousin, Violaine Sautter, Cécile Fabre, Gilles Dromart, Gilles Montagnac, Christophe Drouet, Pierre-Yves Meslin, Olivier Gasnault, Olivier Beyssac, Sylvain Bernard, et al.

SuperCam Calibration Targets on Board the Perseverance Rover: Fabrication and Quantitative Characterization

A.Cousin, V. Sautter, C. Fabre, G. Dromart, G. Montagnac, C. Drouet, P.Y. Meslin, O. Gasnault, O. Beyssac, S. Bernard, E. Cloutis, O. Forni, P. Beck, T. Fouchet, J. R. Johnson, J. Lasue, A.M. Ollila, P. De Parseval, S. Gouy, B. Caron, J.M. Madariaga Mota, G. Arana, M. Bo Madsen, J. Laserna, J. Moros , J.A. Manrique, G. Lopez-Reyes, F. Rull, S. Maurice, R.C. Wiens

Abstract

The Perseverance rover is exploring Jezero crater on Mars since February 2021. SuperCam instrument is part of the scientific payload, combining five different techniques in order to characterize the targets to sample: LIBS (Laser-Induced Breakdown Spectroscopy), Raman and Visible and Infrared (VISIR) spectroscopies, Sound Recording and a colored Imager. Thirty-six calibration targets have been developed for this instrument. Twenty-three of these calibration targets are dedicated to the LIBS technique, corresponding to rocks and/or minerals. Their mineralogical signature is also of interest with Raman and VISIR techniques. The choice and the fabrication of these calibration targets have been made in order to fulfill the science intents of the mission, but also the technical and science intents of each of the SuperCam technique. These calibration targets have been spectrally characterized and they have shown to be chemically homogeneous at the SuperCam LIBS scale. Their elementary compositions are given, using two different quantitative

methods. The composition of the calibration targets will be used as reference for future assessment of the quantitative capability of the SuperCam LIBS technique.

Keywords: Mars, SuperCam, Mars2020, Perseverance, LIBS

Contents

1. Introduction

The Mars2020 *Perseverance* rover was launched on July 30th, 2020, and landed at Jezero crater on February 18, 2021. This mission is contributing to the four long-term science goals of NASA's Mars Exploration Program. In short form, these goals consist of [1]: 1)Search for habitability, 2)Characterize climate evolution, 3)Characterize the geology of Mars, and 4)Prepare for human exploration. The prime objective of this mission is the search for signs of past microbial life on Mars, specifically:

1. Look for habitability, *by identifying if past conditions were capable of supporting microbial life*
2. Seek biosignatures, *by searching for any signs of past microbial life in such an environment*
3. Cache samples, *by selecting, drilling and collecting rocks and soils of interest*
4. Prepare for human explorations, *by testing production of oxygen from the CO_2-rich martian atmosphere*

On-board the *Perseverance* rover, the SuperCam instrument [2, 3] is being used as a remote-sensing facility to analyze rocks and soils that are up to 7 m from the rover (and up to infinity for the imager and visible/near-infrared (VISIR) techniques). This instrument has heritage from the successful ChemCam instrument [4, 5] on-board the Curiosity rover of the Mars Science Laboratory (MSL) mission, which landed in 2012 in Gale crater. SuperCam is the first instrument to examine both the elementary and mineralogical analysis of a target on Mars. It does so by using a suite of five coaligned techniques : just like ChemCam, it uses the Laser Induced Breakdown Spectroscopy (LIBS) technique to determine the elemental composition of the targets, but it also uses Raman (for the first time in planetary science) and VISIR (for the first time *in situ* near-infrared spectroscopy in the 1.3-2.6 µm range) spectroscopic methods in order to access some mineralogical and structural information. A microphone provides a mean to study the physical parameters of the sampled rocks (such as hardness [6]) as well as to some atmospheric parameters (wind direction [7]). The context for these chemical and mineralogical analyses is provided by a color Remote Micro-Imager.

More details about each technique can be found in [2, 3, 8]. The SuperCam sampling footprint varies between 0.3 mm for LIBS at close range (1.56 m, distance of the calibration targets) to 1 cm for IR at 7 m distance, and larger at longer distances.

In order to monitor the instrument's health over time as well as to assess the quality of the data, there is an on-board suite of SuperCam Calibration Targets (SCCT). Thanks to the ChemCam experience, SuperCam's LIBS targets are more comprehensive and better prepared than ChemCam's, and additional targets address each of the new techniques. They are located at 1.56 m from the instrument entrance window. The SCCT sample holder is significantly larger than that on ChemCam. An overview of the mechanical aspects and environmental testing of the targets is given in [9]. These SCCTs have been selected and prepared in accordance with the landing-site mineralogies observed from orbital data, in order to address the several science intents of the mission.

This paper focuses on the LIBS (also called "geological") SuperCam Calibration Targets. Considering our experience with the ChemCam instrument and the major importance of the calibration for quantitative LIBS characterization, most of these targets are dedicated to this technique, even though some of them will be used as well for the Raman and VISIR spectroscopy techniques. We first describe the selection of each type of targets, depending on the different objectives. The fabrication process, which is relatively new [10], is also explained in detail. Then, a summary of all the qualitative characterizations is presented, along with an overview of the SCCTs'

spectral signature as seen by all of the SuperCam techniques. The main part of the paper focuses on the quantitative analyses of these targets with third-part techniques as Laser Ablation coupled with a Inductively Coupled Plasma Mass Spectrometry (LA-ICP-MS) and Electron Micro Probe Analyser (EMPA). They are well known for their accuracy and precision, and are fundamental to determine the reference composition of these calibration targets. Finally, the use of the SCCTs on Mars is presented.

2. Overview of the SuperCam Calibration Targets

The on-board calibration targets were designed and implemented to achieve several technical and science objectives related to each technique (Imager, VISIR, Raman, LIBS, microphone). Even though SuperCam has been extensively tested and calibrated before launch, it is important to continue those calibration activities on Mars. The overarching objectives of the on-board calibration targets are the following:

1. To perform a health check and performance status after launch, cruise, entry-descent-landing, and mast deployment;
2. To evaluate the actual performance in a real operational environment, first and foremost the effects of temperature, pressure, and dust;
3. To track any performance drift with time due to component aging and dust accumulation;
4. To provide a "ground truth" solution for SuperCam LIBS quantitative models.

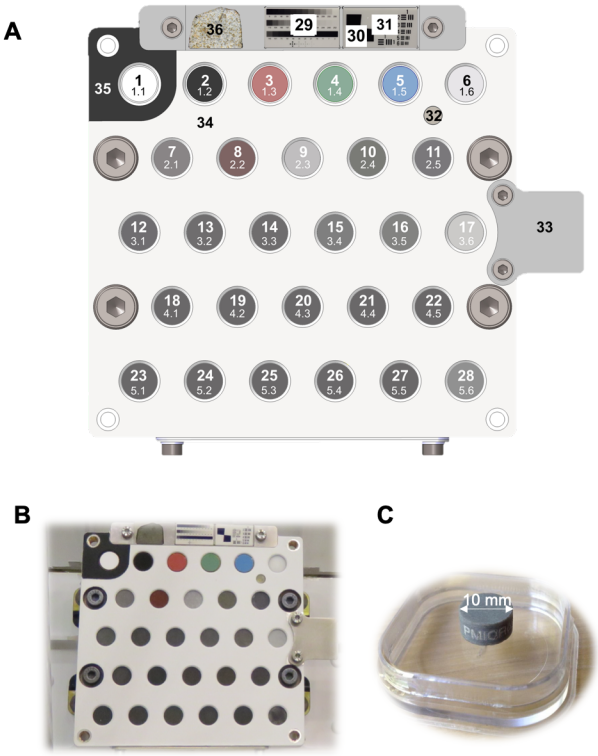

Figure 1: SuperCam Calibration targets on their sample holder. A: Sketch with position number and target number; B: Picture of the Flight Model, mounted on the Rover at JPL. C: Picture of the PMIOR0507 target (Orthoclase, target number 12) before being mounted.

The number of targets was constrained by the total mass budget allocated to the SuperCam calibration target set [9]. A total of 36 targets were selected, as shown in Figure 1. In this section, we review the overall objectives of the calibration targets for each technique, with a particular focus on the LIBS targets.

2.1. Remote Micro Imager dedicated targets

Evaluation of the SuperCam Remote Micro Imager (RMI) makes use of five specific targets. Two geometric plates are dedicated to 1) diagnosing the resolution and the modulation transfer function (MTF: target 29 in Figure 1 ; 2) characterize dynamic performance and point spread function (PSF) (targets 30 and 31 in Figure 1). There are also three colored targets for the color balance and for analysis of hot pixels (targets 3: Red, 4: Green and 5: Cyan - Figure 1). More details about these targets can be found in [9], and about the RMI implementation and performance in [2].

Another particular target, a slice of a martian meteorite (ref. North West Africa, NWA 10170, target 36 - Figure 1), is of interest for the imager. This meteorite is classified as an olivine-phyric shergottite, as it contains olivine phenocrysts [11, 12]. In fact, this meteorite was carried into space by the French astronaut T. Pesquet to the International Space Station (ISS) from November 2016 to June 2017. Following its return to Earth, a slice was incorporated into the SCCT holder, close to the two RMI geometric plates. This target is a tribute to the sample return that the Mars2020 mission is preparing. More details about the story of this meteorite can be found in [2].

2.2. VISIR dedicated targets

The VISIR (Visible and Infra-Red) targets are used for radiometric calibrations. There are two main standards: a white target (target 1 - Figure 1) used for the white balancing of images, and to obtain relative reflectance spectra by ratioing two successive spectra of the sun-lit white target and the

scientific target; and a black target (target 2 - Figure 1) used for VISIR boresight registration. More details can be found in [9] and [13, 8]. In particular, the laboratory characterization of the VISIR-dedicated SCCT presented in Section 5.2 was designed to match the spectral range and resolution of the body unit and mast unit spectrometers.

2.3. Raman dedicated targets

Remote time-resolved Raman spectroscopy is expected to yield information on the mineralogy and crystalline structure of the targeted rocks. The technical and scientific objectives of the Raman calibration targets are: 1) monitoring the health of the instrument, 2) monitoring the intensity of Raman signal of some reference mineral on-board in a true martian environmental context, 3) testing the detection of organic compounds once on Mars, 4) documenting the impact of UV radiation on the spectroscopic properties of organic compounds on Mars surface. To achieve these objectives, Supercam features two Raman-dedicated targets: a diamond and an organic sample (targets 32 and 6, respectively in Figure 1).

The diamond displays a sharp and intense band at 1332 cm^{-1}, and is used for three main purposes: to verify the wavelength calibration with the band position, to check the alignment between the incident laser beam and the telescope field of view by checking the band intensity, and to monitor the instrument's spectral resolution by checking the FWHM of the 1 332 cm^{-1} band .

The organic sample is a polyethylene terephthalate (PET, $C_{10}H_8O_4)_n$) exhibiting a strong Raman signature including aromatic, aliphatic and es-

ter/carboxylic functional groups. Such molecular groups are expected to be found in organic compounds trapped in ancient rocks, and therefore could be searched by SuperCam. Its main objective is to evaluate the capacity of SuperCam to detect organics at the surface of Mars. The ertalyte target can also be used to check the time-synchronization of the instrument by doing time-sweep experiments: the laser pulse is scanned through time and the intensity of the Raman signal is plotted against the moment the ICCD gate opens. Another objective is to perform aging experiments by monitoring the possible degradation of the target under UV radiation. This material was also selected as the calibration target of the Raman Laser Spectrometer (RLS) onboard the ExoMars Rover [14], and will therefore also be used to compare SuperCam to RLS performance. In addition to these two Raman-dedicated targets, the sample holder paint (target 34) constitutes a third opportunistic target, especially interesting as it shows some spectral signatures below 1000 cm^{-1}, a spectral range not covered by the two other targets but of high interest for mineralogy.

Some of the targets devoted to the LIBS technique (next section) are also used for the Raman technique as reference minerals (see part 5.3).

2.4. LIBS targets

The LIBS calibration targets, which are the most numerous, have several instrumental and science objectives. In terms of instrument diagnostics, five main objectives are highlighted in this manuscript: 1) The calibration targets are used to monitor any performance change by frequently analysing the targets using the same instrument parameters. 2) The LIBS technique is sensitive to the atmospheric pressure and composition, so on-board calibration

targets are important to compare the spectra obtained on Mars with those acquired on Earth by mimicking Mars conditions. 3) These calibration targets are also useful to better understand the data acquired on Mars targets (rocks and soils), as several parameters inherent to the LIBS technique need to be investigated on Mars (laser energy, focus, gain). 4) The targets represent a subset of the terrestrial database and are being used to correct any difference between martian and terrestrial spectra on identical targets; this is of great importance to understand the differences between the lab data and the Mars data (and avoid potential biases), and to validate the quantification models that are being developed for chemical composition [15, 16]; 5) One target, the Ti-plate, is mainly dedicated to the wavelength calibration, as on ChemCam. The terrestrial database corresponds to more than 330 samples that have been analysed with SuperCam setup [comprising an Engineering and Qualification Model (EQM) for the Mast Unit coupled with the Flight Model (FM) for the Body Unit] at the LANL laboratory (Los Alamos, NM), under a Mars-like atmosphere during the calibration campaign of SuperCam [3, 2].

SuperCam contributes to all of the Mars2020 science objectives: investigating the geology and geochemistry, studying past environments, and seeking signs of biosignatures at Jezero crater. Therefore the on-board SuperCam calibration targets help fulfill these objectives. Here we point out the scientific purposes of the LIBS calibration targets. 1) Geology: selected calibration targets represent a wide range of rock compositions (silicate-, carbonate-, sulfate-, phosphate-bearing), including a subset of igneous minerals, that are consistent with the geological expectations at Jezero, and are also consistent

with observations at previous landing sites; 2) Geochemical processes: minor elements are powerful probes to better constrain geochemical processes that rocks may have undergone. Therefore, the LIBS targets, both natural and synthetic, have been selected to cover a wide range in minor and trace element proportions, to assess the limits of detection (LOD) on Mars and to anchor the abundance calibration curves; 3) Past environments and climate change: some targets correspond to carbonate, hydrated silicate and alteration products, some others are enriched in sulfate; 4) Astrobiology: the LIBS technique is sensitive to the CHNOPS elements, which are important for life, and therefore several targets contain these elements, along with Cl. Also, high Mn concentrations were identified on Mars at Gale crater with Curiosity [17, 18]; this elements is of great importance to probe oxidizing conditions at the time of their formation. Si-rich targets are also important to account for the astrobiological aspect of amorphous silica, which has been observed already at several landing sites [19, 20, 21, 22, 23, 24, 25, 26];

2.5. Lessons learned from ChemCam

ChemCam on-board *Curiosity* was the first instrument to use the LIBS technique to measure the elemental compositions of Mars samples. To monitor the quality of the LIBS spectra acquired during the mission, calibration targets were mounted on board the Curiosity rover. Their LIBS spectra are regularly compared with spectra obtained in the laboratory of the same targets and in similar environmental conditions. The ChemCam calibration targets also fulfill two additional objectives. First, they are used to create partial calibration curves that are compared with models developed from the Earth database, as a check on the Earth-based quantitative models; Second,

they are used to check any change in the instrument's performance, by repeating the measurements on the same target over the course of the mission.

There are ten ChemCam calibration targets, each 2 cm wide. They correspond to samples whose compositions are supposed to mimic that of rocks expected on Mars from orbital and previous *in situ* missions, whether magmatic [27] or sedimentary [28, 29]. Three are synthetic glass targets with basaltic compositions ranging from picritic, noritic, shergottitic and with variable abundances of trace elements; one is a felsic (alkali, aluminum and silicon-rich, iron and magnesium-poor) natural magmatic glass that is a macusanite from Peru [27]; and four are sulfate-bearing ceramic targets from low to high sulfur contents to mimic Martian sediments [28, 29]. One other target is a graphite, chosen for carbon peak detections, and the last one is a titanium plate for wavelength calibration.

Since Curiosity's landing in 2012, the calibration targets have been widely used, with more than 200 observations on each of them. The titanium plate is used the most frequently, every 14 sols (martian days), for wavelength calibration. Besides their role to validate the quantitative models developed from the terrestrial database [30], they have been used for the investigation of the dust composition [31], as well as for the investigation of LIBS physical effects, such as the signal obtained depending on the distance of the target [32, 33].

What we learned from the ChemCam instrument operating on Mars since 2012 is that optimal on-board standards should meet the following requirements: mechanical integrity (i.e. low porosity and ability to survive launch,

space and landing environments); low surface roughness; identical physical matrix; homogeneity of texture and composition, and wide range of compositions. For example, it is best to select calibration targets that are homogeneous both chemically and texturally throughout their surface in order to obtain the same signal independent of the sampling location on the target. Also, rough opaque surfaces are better than smooth transparent ones to avoid any problem with surface adsorption of the laser photons, needed to create a LIBS plasma. Matrix effects are also important in LIBS and it is desirable to have a similar physical matrix for all the targets [34, 35, 36].

3. Geological Calibration Targets

Perseverance's landing site is a 50-km diameter impact crater which is located on the North West edge of Isidis Basin and North East of the Syrtis area region, in one of the unique carbonate-bearing geological units detected on Mars [37]. Jezero is a Noachian-aged crater, that is interpreted to be an open-basin lake system, with two inlet valleys and one outlet valley [38, 39, 40]. Some remnants of fluvial deltas flank the crater rim's interior. The western delta is to be explored during the prime mission [41]. Jezero's total watershed area has been estimated at more than 10 000 Km^2 [38, 42], meaning that deposits found in Jezero can be sourced from the units around, which is very important for the overall context.

After multiple mapping efforts [38, 43, 44, 45], several units with different mineralogies have been distinguished in orbital data [37, 46, 47]. The salient mineralogies correspond to phyllosilicates, i.e. Fe-Mg smectites, present in the delta deposits and indicative of aqueous alteration [48], olivine/Mg-rich

carbonates-bearing units [37] that have been detected inside the crater, but also regionally outside the crater [38, 45, 49, 50, 51], a mafic mineralogy (mainly high-Ca pyroxenes) mainly associated with the crater floor (but also in the deltas and rim). There are several hypotheses as to how these carbonate-bearing formed, either by serpentinization process or hydrothermalism [37, 38, 47, 52, 53]. Marginal Mg-carbonate deposits have been observed along the west inner rim of the crater. They show the strongest and most diverse carbonate signature observed within the crater and may have an origin related to the lacustrine activity [54]. Finally, impact mega-breccias (with high-Ca pyroxene signatures) have also been detected on the western crater rim, and some of the blocks inside could represent pre-Noachian igneous crust, as it is interpreted to predate the Isidis basin formation [55]. Details about the mineralogy and stratigraphic relationships between units can be found in [45]. In summary, Jezero crater is a unique place exhibiting primary and secondary mineralogies, along with carbonate-bearing deposits of intriguing origin. This site records the past environment of Mars, its climate evolution, and therefore is of great interest in the search for biosignatures and organic compounds, *in situ* and for sample return.

A set of 23 LIBS targets has been selected in order to fulfill both instrumental calibration needs and science objectives for the LIBS technique. The list of the on-board calibration targets is given in Table 1, along with their short description, their technical name and their position on the holder. The convention for these technical names was as follows: 1) the length has to be less than 10 digits; 2) first letter (except for Titanium and Shergottite)

Position	Target #	TargetName	Description	Science Intent
2.1	7	TSRICH0404	BHVO-2 basalt and K sulfate mixture	Sulfur detection
2.2	8	LCMB0006	Chert	Past acqueous environment and astrobiology interest
2.3	9	LCA530106	Calcite	Carbonate calibration
2.4	10	PMIFS0505	Ferrosilite	Stoichiometric reference
2.5	11	TAPAG0206	Fluoro-Chloro-Hydro Apatite	Volatile detection, phosphate
3.1	12	PMIOR0507	Orthoclase	Stoichiometric reference
3.2	13	PMIDN0302	Diopside	Stoichiometric reference
3.3	14	PMIFA0306	Olivine	Stoichiometric reference
3.4	15	PMIAN0106	Andesine	Stoichiometric reference
3.5	16	PMIEN0602	Enstatite	Stoichiometric reference
3.6	17	TSERP0102	Serpentine/Talc	Hydrated silicate, alteration product
4.1	18	LBHVO20406	BHVO-2 standard basalt	Mars analog, basaltic composition
4.2	19	LJSC10304	JSC-1 standard	Mars soil analog
4.3	20	LANKE0101	Ankerite	Carbonate calibration
4.4	21	LSIDE0101	Siderite	Carbonate calibration
4.5	22	LJMN10106	JMN-1 standard Mn nodule	Mn enrichment, coating detection
5.1	23	NTE010301	Basalt dopped in minor elements	Calibration and quantification of Cu, Zn
5.2	24	NTE020106	Basalt dopped in minor elements	Calibration and quantification of Mn, Ba, Cr
5.3	25	NTE030106	Basalt dopped in minor elements	Calibration and quantification of Zn
5.4	26	NTE040106	Basalt dopped in minor elements	Calibration and quantification of Li, Sr
5.5	27	NTE050301	Basalt dopped in minor elements	Calibration and quantification of Ni
5.6	28	SHERG02	Shergottite	ChemCam cal. target replicate, cross calibration
/	33	TITANIUM	Titanium	Wavelength calibration

Table 1: List of the SuperCam geological targets on-board *Perseverance*, with their position on the sample holder.

indicates the city of sample laboratory, or where the replicate was sintered (see part 4); 3) three to five characters for the proper name of sample; 4) two digits for the batch number for the sintering; 5) two digits for the replicate number. Among these 23 calibration targets, there is a titanium plate dedicated to the wavelength calibration just as for ChemCam. More details about this target can be found in [9]. The 22 geological targets are split into 5 groups depending on the science intent as well as the calibration purpose:

3.1. Primary Igneous Minerals

From the ChemCam experience, targets with well-known stoichiometric compositions (such as minerals) are needed in order to validate the prediction models that are developed from a laboratory database. Such stoichiometric

compositions are useful to calibrate key elemental ratios including Al/Si, (Fe+Mg)/Si, (Na+K)/Si, (Ca+Na)/Si, Na/K. From a LIBS perspective, the use of these ratios can check and potentially correct for matrix effects and variation in ablated mass, which is the prerequisite to realize robust calibration curves. Moreover, they are used for geochemical comparison between measurements made on Mars and in the laboratory on Earth, and can assist in a mineralogical assessment of the martian sampled targets.

To fulfill this need, several igneous minerals have been chosen: feldspars, olivine and pyroxenes, which are widespread on Mars both in igneous rocks but also in sedimentary rocks (mostly as detrital minerals). Igneous minerals involve various solid solutions between end-members: Na-Ca in plagioclase, Na-K in K-feldspar, Fe-Mg in olivine, and Ca-Fe-Mg in pyroxene. Due to the constraint concerning the number of targets, it was not possible to select all of the end-members. Also, a few of them would not have been relevant to the martian geology and therefore six igneous minerals have been carefully selected. We made the following compromise in selecting them: a) three targets are solid solutions frequently observed on Mars ([56, 57] and references therein): orthoclase and andesine for feldspar solid solutions; and Forsterite65 (Fo_{65}) for olivine. b) three pyroxene targets on the other hand have been chosen close to end-member compositions: Ca-Mg (diopside), Mg (enstatite) and Fe (ferro-hypersthene). Within the pyroxene quadrilateral composition domain, the field covered by those three mineral compositions encompasses a majority of pyroxene compositions found in Martian meteorites as well as by *in situ* analyses of ChemCam on Curiosity ([56, 57]). Also, the ferro-hypersthene plays an important role for the Fe quantification,

as it represents the highest Fe content among the on-board calibration set.

Jezero crater was thought before landing to have a mafic floor unit [37, 38, 44, 45, 46, 47, 49]. Whether it does or not, it is important to have targets that address igneous compositions. Observations at Gale crater suggest that much of Mars' sedimentary material may consist of fine-grained igneous material with varying amounts of clay matrix [58].

All these targets correspond to natural crystals. The two feldspars are sourced from centimeter-sized single crystals. The plagioclase presents an andesine composition and comes from Purdy mine Ontario (Canada); the K-feldspar with orthoclase composition is from Alto Ligonha in Mozambique. Olivine Fo_{65} has been extracted from polycrystalline aggregates (millimeter-sized crystals) within a dunite sample from Bushveld stratified complex (Australia) [59]. The pyroxenes (diopside, enstatite and ferro-hypersthene) are centimeter-sized single crystals that come respectively from the Ecole des Mines collection in Paris (France), from Andranondambo outcrop in Maromby (Madagascar) and from metamorphic rocks of Mansjöbeg südlich Los Härjedalenin (Sweden).

3.2. Targets enriched in minor elements

The terrestrial laboratory database covers a wide range of compositions and rock types. Minor elements are also well covered. However, this database has been developed mainly to quantify the major elements, and therefore in these standards the trace/minor elements do not always permit the construction of calibration curves or limit of detection (LOD) determination. Also, because many of these elements have relatively few emission lines, many of which are low in intensity, it is important to have a reference for LIBS spectra

acquired on Mars.

Five different targets have been selected to address this goal, being doped in several elements in various amounts: Li [10-80 ppm], Cr [500-3000 ppm], MnO [500-4000 ppm], Ni [500-5000 ppm], Cu [50-2000 ppm], Zn [1000-10000 ppm], Rb [10-1000 ppm], Sr [50-1500 ppm], and Ba [50-2000 ppm]. The range and contents of these elements have been chosen based on ChemCam's observations at Gale crater [60, 61] (Figure **??**), and the expected geology to be encountered in Jezero crater, along with some laboratory investigations (this is the case for Ni). With such targets, the LOD on Mars of all these elements can be well identified, along with their quantification model. These trace and minor elements are of interest in terms of geological processes undergone by the analyzed rocks. Some are being used as clues for a magmatic history, others for water/rock ratios in sedimentary processes, or also to distinguish different meteoritic falls [62, 63]. These five targets have an overall basaltic composition. These, combined with the igneous mineral calibration targets and others, are useful to characterize targets of igneous composition and may help to study weathering processes in a sedimentary context.

3.3. Standard targets

Standard targets are interesting as their bulk chemistry can be used as Mars analog compositions. Three standards have been selected: a basalt (BHVO-2) Basalt, Hawaiian Volcanic Observatory [64], a Mars regolith analog (JSC Mars-1) [65], and a manganese nodule (JMn-1) [66].

Concerning their calibration purpose, they all have a specific interest. First of all, they have very distinct chemical compositions, which are im-

portant to encompass the chemical matrix effects that can be observed with LIBS [67]. Also, the JSC-1 soil (Mars regolith) analog contains the highest TiO_2 content of the targets, which is important to validate the earth-based quantification model(s). The JMn-1 target is special due to its MnO content, up to 30 wt%. This represents the highest MnO abundance among the SCCT and it helps constraining the prediction model(s), as high Mn values may interfere with the iron predictions based on ChemCam experience. Targets with a Mn-rich coating have been sampled with ChemCam at Gale crater [17, 18], along with Mn-rich vein filling material and Mn-rich nodules [68]. This JMn-1 standard also has the highest Ni abundance among the targets, which is important due to the elevated LOD of this element. Those standards provide great insights concerning the past atmosphere on Mars, as Mn requires water and highly oxidizing conditions to precipitate as an oxide [69, 70]. On Earth, coatings are also related to some biological processes (microbes can colonize a pre-existing coating, or they can create the coating themselves). Such targets are therefore of particular interest in terms of astrobiological potential of the planet, which is one of the main goal of the Mars2020 mission. The BHVO-2 basalt comes from the USGS collection and is considered as an analog for the martian basaltic floor, and could be a good reference to compare with data obtained on the mafic floor of Jezero. It comes from the pahoehoe lava from the Halemaumau crater within the Kilauea caldera, in Hawaii (USA) [64]. The JSC Mars-1 material comes from the Johnson Space Center and has been collected in a palagonitic tephra in the Pu'u Nene cinder cone in Hawaii (USA) [65]. The JMn-1 manganese nodule originates from the collection of the Geological Survey of Japan. This

Mn-rich sample comes from the floor of the southern Central Pacific Basin, at a depth of around 5 Km below the water sea level [66].

3.4. Natural rocks

Natural rocks are part of the calibration data set, and correspond to five different targets: one chert, three carbonate-bearing rocks (limestones) and one serpentine/talc.

For an instrumental point of view, these compositions fulfill the need of having a wide variety of rock types to minimize potential chemical matrix effects. These rock types are clearly different from each other, with limestones containing almost no Si and instead contain a significant amount of carbon in the form of carbonates, whereas the chert is almost pure SiO_2, and serpentine is a hydrated silicate. The quantification of the SiO_2 content in a relatively pure SiO_2 target is really fundamental, as for example amorphous silica (like opaline) is known to have a role in microbial fossils preservation [71] and therefore is of interest for astrobiological perspectives. Chert therefore accounts for the Si-rich end-member for calibrations. The carbonates and chert correspond to end-members with respect to their SiO_2 and FeO content.

Carbonate minerals have been observed in several locations on Mars and on Mars meteorites. However, most of the time their abundance is low, such as in Mars meteorites (<1 wt % [72]), or in the dust from orbital and *in situ* measurements [73]. *In situ* measurements revealed a carbonate-rich material at Comanche outcrop, explored by the Spirit rover (with up to 30 wt % of carbonates [74]). At Gale crater, only hints of carbonates have been detected [75], but siderite has been detected recently in the clay-rich unit [76].

However, orbital data observed carbonate-bearing rocks at Jezero crater and overall in the Syrtis area [37, 54], along with some hydrated silicates such as serpentine [52]. Carbonates may not be easy to discriminate with LIBS when they are mixed with other material [77, 78]. Also, carbon content has not been quantified for ChemCam, and the C lines observed in the spectra mainly come from the breakdown with the atmospheric CO_2 [77, 78]. Therefore, to better enable detection of carbonates with SuperCam, we have selected 3 samples: calcite (Ca), ankerite (Ca, Fe, Mg) and siderite (Fe). The calcite comes from the Paleozoic "Lunel limestone" formation in the quarry of Ferques (northern France). The ankerite comes from the Dome Mine in Timmins in Ontario (Canada), and the siderite comes from Antler Mine in Mohave County, Arizona (USA). The Jezero crater carbonate-bearing rocks, observed through orbital data, correspond mainly to Mg-carbonates, exposed in different contexts [45, 54]. They are mainly spatially associated with olivine and serpentine [54, 79]. This assemblage suggests an *in situ* deposition, possibly a serpentinization product of the ultramafic igneous floor, even though this origin could also be detrital [38, 44, 79]. In this context, a serpentine has also been selected as a calibration target. The selected serpentine comes from the Jeffrey Mine in Quebec (Canada). However, after the sintering process and its exposure to high temperature (see part 4), the serpentine target structure turned into talc, but with no change in terms of elemental composition. [80]. With both carbonate and serpentine (at least in chemical composition), the onboard calibration set contains both major products formed by olivine alteration under aqueous conditions, although it does not contain iron oxides, which are also by-products.

Finally, hydrated silica appears to be relatively common on Mars, as it has been detected both from orbit and *in situ*. From orbit, it has been detected in terrains from the Noachian to the Amazonian, all over the surface in various geological settings, from hydrothermal origin [81], but also from alteration processes [82, 83]. *In situ* observations of hydrated silica are also numerous, in diverse environments as well. The Opportunity rover team detected enriched silica (possibly hydrated) on the western rim of Endeavour crater, mixed with some Al-rich smectite, suggesting an acidic diagenetic origin [19, 20]. The Spirit team also detected some enriched silica hypothesised to be opaline silica formed by hydrothermal activity [21, 84, 22, 23], at Home Plate. At Gale crater, Si-rich rocks were also detected in the forms of detrital tridymite in mudstone suggested to come from silicic volcanism [24], and of some amorphous silica in fracture halos [25], suggested to be opaline silica from their hydration level [26]. Hydrated silica on Mars is an indicator of past aqueous conditions of the planet (diagenetic or hydrothermal events). It may also represent a particular interest in terms of astrobiological potential [85, 86, 87], which is an important aspect for the Mars2020 mission.

As mentioned earlier, a chert target has been selected for the SuperCam calibration targets. This natural target ensures that SuperCam will correctly quantify high SiO_2 abundances. The selected chert comes from the 3.46 Ga Marble Bar Chert Member of the East Pilbara Craton (Western Australia) [88].

3.5. Synthetic targets

Taking into account all the targets presented above, some geochemical elements and targets of interest are still missing in the on-board calibration

dataset, such as sulfates, chlorides, and halogens. Therefore, some synthetic targets have been specifically prepared in order to make sure that these elements are present in these calibration targets and well detectable by SuperCam at the different levels of concentration, allowing all science objectives to be addressed.

Besides the hydrated silica mentioned earlier, remote-sensing and *in situ* observations have provided extensive evidence for the presence of other hydrated minerals such as phyllosilicates and sulfates on Mars. These hydrated minerals are important for understanding Mars's climate and its past habitability. First, clear orbital signatures have shown the presence of Ca and Mg hydrated sulfates in light-toned layered sediments [89, 90]. Sulfates have now been observed from orbit in many different types of outcrops ([91] and references therein). Gale crater was chosen as the Curiosity landing site from orbital detection of a transition between clay-bearing to sulfate-bearing rocks, suggesting a significant change in climate [82, 92]. *In situ* analyses at Gale, approaching the sulfate-bearing unit capping Mount Sharp, revealed a vast network of Ca sulfate filling veins at certain regions [93, 94, 95], and most of them correspond to bassanite [96], even though anhydrite is also present ([97] and reference therein). Primary Mg sulfates were also detected more recently [98]. A sulfate-bearing calibration target was therefore important to include with SuperCam, even if no sulfates have been identified within Jezero crater from orbit. Unfortunately, Ca and Mg sulfates were not possible to include in the calibration targets. Mg sulfates are hygroscopic, whereas the mechanical structure of Ca sulfates changes with temperature, along with their hydration state. These properties were not in accordance

with the fabrication process chosen for the calibration targets, nor with the validation steps needed for delivery at JPL [9]. As featuring a pure sulfate calibration target was not necessary, the team decided to create a mixture between a basaltic material and a non-hygroscopic sulfate material that is also stable with temperature. The final choice was a mixture between the BHVO-2 basalt (see above section), and a K sulfate called arcanite. Natural arcanite is relatively rare on Earth and not really relevant for Mars geological settings and past habitability, but it addresses the need of detecting sulfur-bearing targets with SuperCam, as well as of validating the quantification model.

Phyllosilicates are also extensively observed from orbit ([91] and references therein). These hydrated minerals reflect a past environment where water on Mars was abundant. Unfortunately, no phyllosilicate such as clay minerals could be part of the calibration targets on-board, as their physical properties made them fail all the mechanical tests [9] required for such flight models. Therefore, such targets are only included in the laboratory database. However, the serpentine represents an hydrated alteration product.

Apatite is an ubiquitous magmatic mineral found in SNC meteorites. It is a significant reservoir of halogens in these meteorites and has been used to estimate the halogen budget of Mars [99]. While apatites in Mars meteorites are mainly enriched in Cl and H [100, 101, 102], apatites identified in sandstones and pebbles at Gale crater by ChemCam [103, 104] are F-rich. Determining the composition of apatite-bearing Martian rocks is important to understand the behavior of volatiles during planetary differentiation [101] and apatite is an important mineral for geochronological dating. A wide va-

riety of apatites, including possible hydroxyapatites, may thus be expected. Therefore, providing a synthetic fluorinated and chlorinated hydroxy-apatite as a calibration target appears especially pertinent. One apatite composition was selected to give a reference for P, Cl, F and H abundances. While Cl and F are important in order to estimate the halogen budget of the Martian mantle, P and H are also relevant for organic detections. Besides its geochemical importance, this target is used as a reference for the detection of P, Cl, F and H, as this is the only target containing these elements, and having them well quantified. Since this is also the only phosphate, it will help validate the quantification model, and will be useful whenever P is present in significant abundance in a sample.

Finally, the SuperCam calibration set also includes a "ChemCam replicate", which is the ChemCam shergottite-composition synthetic glass calibration target [27]. It is used as a reference for cross-calibration between both instruments. It also represents a certain Martian rock type, as it is a basaltic shergottite that has a chemistry similar to Bounce Rock ejecta observed at Meridiani Planum and to basaltic shergottite EETA79001B [105, 106].

We emphasize that SuperCam's LIBS calibration targets should address the instrument's purposes and also the science objectives of the mission. With that, SuperCam should be able to determine the igneous chemistry of the putative mafic floor, characterize the chemistry of the carbonates observed from orbit within and around, and therefore give insight to the relationship between the olivine and some of its alteration products such as serpentine or Mg/Fe carbonates along with some phyllosilicates. More-

over, these calibration targets help identify diagenetic products (for example Mn/Fe oxides, Si-rich deposits), and also aid the search for biosignatures thanks to their content in specific elements such as Mn, Cl and the C, H, N, O, P, S.

4. Fabrication Process

The choice of the fabrication process for the SuperCam LIBS Calibration targets has been driven primarily by the lessons learned from ChemCam. ChemCam's calibration target assembly [27, 28, 29] was composed of two types of material: glassy targets to simulate igneous compositions, and some pressed powders sintered at 800 degrees C with a small amount of lithium tetraborate to simulate Mars sediments. However, the synthetic silicate glasses had a different physical matrix than igneous rock (resulting in physical matrix effects that have hindered their use in calibration), and the sintered material were quite heterogeneous at the scale of the laser beam [36].

Given that background with ChemCam, a renewed effort was made to produce more representative and more homogeneous on-board targets for SuperCam. Homogeneous targets are easiest to produce by vitrifying crushed powder. However, it is well known that the laser-matter interaction during ablation can be significantly different on glass and on crystalline material, as they have different optical properties as well as physical properties such as hardness. Powder pellets obtained by conventional uniaxial pressing would be usable for all the SuperCam spectroscopies, but such pellets cannot handle the mechanical and thermal constraints induced by launch and landing.

Natural rocks are generally more robust, but they are rarely homogeneous at the sub-millimeter resolution of the SuperCam techniques, due to the mineral-grain distribution. Therefore, with all these constraints, the choice was to make most targets by a sintering process, using a flash consolidation technique, namely the Spark Plasma Sintering (SPS) process. Only three targets have not been sintered (titanium, shergottite and chert - see below).

The SPS technique is a sintering process involving high pressure along with an electrical current passing through the powdered sample [107, 108]. It is a well known way to significantly improve the mechanical properties of the sintered samples compared to usual pressing techniques [109]. This technique reaches a better density and compaction for a wide range of materials, and improves the bonding quality [110] thanks to a mechanical grain-to-grain rearrangement, the growth of the finest grains and lattice dislocation. In that way, sintered pellets have no risk of outgassing in vacuum (or under Mars environment) and have mechanical properties that are in accordance with NASA requirements [10]. The effect of heat has been investigated in different matrices and even though some mineral phases may be modified, no important bulk chemical changes or reduction in homogeneity have been noticed after SPS [10]. Also, [111] have shown the high repeatability of the technique. The added value and quality of such a technique is discussed in a large number of studies cf. [112]. The SPS technique is fast, as it takes only a few minutes to sinter materials. The overall process consists in using fine-grained powders. This powder is placed into a graphite die in a treatment chamber that may be put under vacuum or a controlled atmosphere (*e.g.*

argon). A pulsed current is then applied, and passes through the sample via electrodes and the conductive die. At the same time, a uniaxial mechanical pressure is applied to the die for a few minutes. Both current and pressure are then released (this step being controlled if needed). The sample is then left to cool down for a few minutes.

The SPS process has been performed by two laboratories: Mateis laboratory, INSA, Lyon (France) using an SPS HP D25 machine (FCT®, Germany), and CIRIMAT laboratory (PNF2 national CNRS platform) in Toulouse (France), using an SPS Sumitomo Dr Sinter 2080 apparatus. Two different methodologies were used. In Lyon, for each composition, one pellet of 40 mm diameter was made and then cored to extract 6 pellets of 10 mm each in diameter. As it is known to have a thermal gradient from the center to the edge of the sample [111], the 6 cores have been extracted from the same distance from the center. On the other hand, in Toulouse, for each composition, 6 individual pellets of 11 mm in diameter each were fabricated. The pellets were then slightly ground in order to remove any graphite from the die, and to adjust the diameter to 10 mm. The machining process was performed either at Société Audoise de Précision (SAP) in Ambres (France) or at SCERAM ™ in Lyon (France), with no oil and no water to avoid any contamination of the samples. Table 2 gives the detailed parameters for each target, from Lyon and Toulouse.

Only the standard targets (BHVO-2, JSC-1, JMn-1) were purchased in the form of powders, while, for all the other selected targets, several steps had to be performed before the sintering.

The igneous minerals were coarse single crystals that experienced slow

		SPS conditions		
Target	**Description**	***Temperature (Celcius)***	***Pressure (Mpa)***	***Duration (min)***
PMIEN060x	Enstatite	1375	100	3
PMIOR050x	Orthoclase	1150	100	5
PMIAN010x	Andesine	1200	100	3
PMIFSI050x	Ferrosilite	1050	100	3
PMIFA010x	Forsterite	1150	100	10
PMIDN030x	Clinopyroxene	1200	100	3
NTE01030x	Trace elements	800	75	3
NTE02010x	Trace elements	800	75	3
NTE03010x	Trace elements	800	75	3
NTE04010x	Trace elements	800	75	3
NTE05030x	Trace elements	800	75	3
LCA53010x	Calcite C53	750	75	3
LJSC1030x	Mars soil sim.	750	75	3
LBHVO2040x	Basalt	1000	75	3
LJMN1010x	Mn-rich	750	75	3
TAPAG030x	Apatite	950	50	5
LANKE010x	Ankerite	750	75	3
LSIDE010x	Siderite	750	75	3
TSERP010x	Serpentine	750	100	3
TSRICH040x	S-rich	1000	100	3

Table 2: SPS parameters (temperature, pressure, and duration of constraints) used for each of the sintered LIBS SCCTs.

cooling to reach such a size (mm-cm). As temperature decreased, exsolution lamellae may be formed within some of the crystals. Therefore, it was necessary to crush them down to fine powders (grain size smaller than average exsolution lamellae) to produce mechanically and chemically homogeneous samples. The grain size of the powders is estimated to be less than 50 µm. After this grinding step, the SPS technique was performed as referred in Table 2.

The natural targets (chert, carbonates, serpentine) were natural rocks that have been finely crushed, the same way as the igneous minerals, with grain sizes below 50 µm before the SPS process. The sintering process was attempted on the chert. This rock, mainly composed of SiO_2 quartz, yielded crumbly pellets by SPS at low temperatures. The sintering was successful only above 1700°C by melting SiO_2 [10]. The pressure and temperature the sintering process were thus similar to those of chert formation. In the end, we used chert in its original state, after coring the main rock to get six samples from it.

The minor-doped targets were produced the same way as the glassy ChemCam calibration targets [27]; they were synthesized by mixing powders of carbonates, silicates, oxides and sulfates in order to get the same bulk composition for the six replicates done for each doped targets, adding minor and trace elements as listed above. These mixtures went through several melting, cooling, and crushing cycles in order to obtain a homogeneous glassy material. The actual composition of the synthetic silicate glasses was then checked by LA-ICP-MS measurements in order to make sure the desired major-element composition along with the minor/trace element contents was

reached. This glassy material was then crushed one last time prior to performing the SPS process.

Concerning the sintered targets, each sample followed its own specific process. The sulfur-rich target (TSRICH) is simply a mixture of 30 % of the BHVO-2 standard powder with 70 % of the arcanite (K sulfate) commercial powder, before being sintered.

The ternary F, Cl, OH-apatite target was synthesized in full at CIRIMAT, Toulouse. The aim here was to prepare an apatite phase simultaneously containing OH^-, F^- and Cl^- ions in the hexagonal crystal structure. Two F^-OH^-apatite and Cl^-OH^-apatite precursor powders were first obtained by tuned fluorination and chlorination, respectively, starting from stoichiometric OH^-apatite. The process was carried out in a tubular furnace under argon flow (1 atm) in the temperature range 900-950°C, and NH_4F or NH_4Cl were selected as halogen reagents. The sublimation/decomposition of these compounds led to gaseous HF and HCl molecules able to partially dehydroxylate the OH-apatite. The F^-OH^-apatite and Cl^-OH^-apatite precursor powders were then mixed (for 4 hours) in the desired proportions selected to produce the targeted F, Cl, OH composition. Electron microprobe analyses have been performed in order to check if the desired composition was achieved. Then, the sample was sintered as presented in Table 2. The sintering process applied to this apatite target was different to that of the other targets in two respects. First, the applied mechanical pressure was slightly lower than that of other targets. But most importantly, the sintering process was carried under Argon (instead of vacuum) in order to minimize the loss of Cl. This led to a ternary F, Cl, OH apatite phase corresponding to the chemical formula

$Ca_5(PO_4)_3(OH_{0.08},F_{0.49},Cl_{0.43})$ as assessed by electron microprobe analyses.

Finally, for the shergottite ChemCam replicate [27], in order to avoid any contamination or change in composition during crushing and the SPS processes, this sample was only cored to the right size directly from the replicate. As it is a glassy material, this process was tricky and we were able to get only two samples with the correct dimensions from the material remaining from ChemCam. Finally, the titanium target is a plate from a commercial supplier [9], and as mentioned above, the Chert (natural target) was cored directly from the rock.

5. Spectral characterization of the geological samples

In this section we use qualitative observations to investigate the homogeneity of the targets. Quantitative compositions will be given in Section 6.

5.1. Geological Targets' Homogeneity to LIBS

Targets that are dedicated to the LIBS technique are used as references once on Mars. It is therefore of prime importance to characterize them in terms of homogeneity (chemical and mineralogical) in order to make sure that each pellet presents a homogeneous elemental spatial distribution, and that each replicate (the one on-board Perseverance and the others on different labs) is similar for every given composition. A summary of all the techniques used for each target and replicate is presented in Table 3. This section is only a short summary of [80], and therefore details with tables and figures can be found in [80].

Target Name	Description	EMPA	LA-ICPMS	XRF and microRaman	LIBS in Spain	LIBS in France	SuperCam-like Raman	VISIR in Canada	VISIR in France
TSRICH040x	BHVO-2 basalt and K sulfate mixture	None	None	All replicates	CR replicate	All replicates but FM and FS	Lab replicate	CR replicate	Lab replicate
LCMB000x	Chert	All replicates	FM and FS replicates	All replicates	CR replicate	All replicates but FM and FS	Lab replicate	CR replicate	Lab replicate
LCAS3010x	Calcite	All replicates	FM and FS replicates	All replicates	CR replicate	All replicates but FM and FS	Lab replicate	CR replicate	Lab replicate
PMIFS050x	Ferrosilite	All replicates	FM and FS replicates	All replicates	CR replicate	All replicates but FM and FS	Lab replicate	CR replicate	Lab replicate
TAPAG020x	Fluoro-Chloro-Hydro Apatite	All replicates	FM and FS replicates	All replicates	CR replicate	All replicates but FM and FS	Lab replicate	CR replicate	Lab replicate
PMIOR050x	Orthoclase	All replicates	FM and FS replicates	All replicates	CR replicate	All replicates but FM and FS	Lab replicate	CR replicate	Lab replicate
PMIDN030x	Diopside	All replicates	FM and FS replicates	All replicates	CR replicate	All replicates but FM and FS	Lab replicate	CR replicate	Lab replicate
PMIFA030x	Olivine	All replicates	FM and FS replicates	All replicates	CR replicate	All replicates but FM and FS	Lab replicate	CR replicate	Lab replicate
PMIAN010x	Andesine	All replicates	FM and FS replicates	All replicates	CR replicate	All replicates but FM and FS	Lab replicate	CR replicate	Lab replicate
PMIEN060x	Enstatite	All replicates	FM and FS replicates	All replicates	CR replicate	All replicates but FM and FS	Lab replicate	CR replicate	Lab replicate
TSERP010x	Serpentine/Talc	All replicates	FM and FS replicates	All replicates	CR replicate	All replicates but FM and FS	Lab replicate	CR replicate	Lab replicate
LBHVO2040x	BHVO-2 standard basalt	All replicates	FM and FS replicates	All replicates	CR replicate	All replicates but FM and FS	Lab replicate	CR replicate	Lab replicate
LJSC1030x	JSC-1 standard	All replicates	FM and FS replicates	All replicates	CR replicate	All replicates (including FM) but FS	Lab replicate	CR replicate	Lab replicate
LANKE010x	Ankerite	All replicates	FM and FS replicates	All replicates	CR replicate	All replicates but FM and FS	Lab replicate	CR replicate	Lab replicate
LSIDE010x	Siderite	All replicates	FM and FS replicates	All replicates	CR replicate	All replicates but FM and FS	Lab replicate	CR replicate	Lab replicate
LJMN1010x	JMN-1 standard Mn nodule	All replicates	FM and FS replicates	All replicates	CR replicate	All replicates but FM and FS	Lab replicate	CR replicate	Lab replicate
NTE01030x	Basalt dopped in minor elements	All replicates	FM and FS replicates	All replicates	CR replicate	All replicates but FM and FS	Lab replicate	CR replicate	Lab replicate
NTE02010x	Basalt dopped in minor elements	All replicates	FM and FS replicates	All replicates	CR replicate	All replicates but FM and FS	Lab replicate	CR replicate	Lab replicate
NTE03010x	Basalt dopped in minor elements	All replicates	FM and FS replicates	All replicates	CR replicate	All replicates but FM and FS	Lab replicate	CR replicate	Lab replicate
NTE04010x	Basalt dopped in minor elements	All replicates	FM and FS replicates	All replicates	CR replicate	All replicates but FM and FS	Lab replicate	CR replicate	Lab replicate
NTE05030x	Basalt dopped in minor elements	All replicates	FM and FS replicates	All replicates	CR replicate	All replicates but FM and FS	Lab replicate	CR replicate	Lab replicate
SHERG0x	Shergottite	All replicates	FM and FS replicates	All replicates	None	All replicates but FM and FS	Lab replicate	CR replicate	Lab replicate

Table 3: Summary of all characterization techniques used on the calibration targets. FM, FS and CR replicates stand for Flight Model, Flight Spare and Calibration Replicate, respectively. EMPA and LA-ICP-MS have always been performed on the bottom of the targets.Quantitative results from those techniques will be given in Section 6

Different techniques have been used to evaluate the homogeneity of the calibration targets: µXRF "mapping" for the elemental spatial distribution, continuous Raman spectroscopy imaging for the structural variability and mineralogical heterogeneity, and LIBS individual analysis for a more sensitive comparison to our needs. More details concerning these different methodologies can be found in [80].

XRF and Raman analyses were performed at the University of Basque Country in Bilbao (Spain). Concerning the µXRF technique, sixteen single-spot analyses (4×4 grid), with a pixel resolution of 25 µm, were done to simulate a single 100 µm analysis. A total of 10 randomly distributed spots were therefore analyzed on each sample and each replicate was analysed the same way. The homogeneity was evaluated by averaging the 10 spots, and calculating the relative standard deviation ("RSD" in %) for each element detected. The distribution of the elements was considered homogeneous when

the RSD was lower than 10 %, quasi-homogeneous when RSD was between 10 and 20 %, and heterogeneous when RSD is higher than 20 %. This homogeneity gradation concerns only the major constituents, as minor elements that are present at less than 1 wt% can display higher RSD values.

Raman hyperspectral mapping was used to check the target structural and mineralogical homogeneity. For this technique, a 532 nm continuous-wave laser was used with the same wavelength as the SuperCam instrument. The analyzed spectral range was 100-3200 cm^{-1}. All replicates of each target have been mapped.

LIBS measurements were made at IRAP in Toulouse (France), as well as at University of Malaga (Spain). Measurements in Toulouse were acquired using the ChemCam laboratory unit [4, 5, 113, 96], which is very similar to the Flight Model onboard Curiosity. The mast unit is placed in a climatic chamber at $-10°C$ in order to get the best energy for the laser. The spot size on the target was around 300 µm at 1.5 m from the instrument. More details about the setup can be found in [96]. Nine random points of 30 shots were performed on 4 of the replicates (Flight Model and Spare were preserved). Samples were placed in the Mars chamber, filled with 6 mbar of Mars-like atmosphere (95.7 % CO_2, 2.7 % N_2, 1.6 % Ar). LIBS spectra were then processed using the same methods as the Mars ChemCam spectra [114].

LIBS analyses in Malaga were performed using a laboratory LIBS setup that was tuned in order to have similar characteristics as the ChemCam setup. The main difference is the spot size that is slightly bigger (350 µm). For each target, eleven sampling points were distributed over an inner circumference of 6.0 mm in diameter: 9 points of 30 shots to evaluate surface

homogeneity and 2 of 90 shots to evaluate the in-depth homogeneity. Targets were placed under a Mars-similar atmosphere (only CO_2) at 7 mbar, at a distance of 1.5 m. Only one replicate was sampled by LIBS for each target in Malaga.

XRF mapping. Most of the targets have a homogeneous distribution of their major elements, with RSD less than 10 %. However, the JSC Mars-1 target (regolith analogue) and the JMn-1 target (Mn nodule) present some chemical heterogeneity, but only for elements below 2 wt% in content (Na_2O, K_2O, TiO_2). This heterogeneity observed for the minor elements is not a special concern, as the JMn-1 target has been specifically chosen for its high Mn content, which is seen very homogeneous by XRF. More details about the methodology and results can be found in [80].

Raman imaging. The SuperCam calibration targets have been established mainly for LIBS analysis purposes, and therefore some of them are not easily characterized by the continuous-wave laser Raman spectroscopy used for these homogeneity investigations. This is the case for the targets enriched in minor elements as they are amorphous materials. As previously discussed, during the sintering process some targets have shown a mineralogical transformation including phase transition [10]. It was the case of siderite (Fe carbonate), which led to a calcite and magnetite mixture; and of ankerite (initially containing some silicates) that changed into calcite and quartz. Fortunately, the mineral targets (Andesine, Diopside, Enstatite, Olivine, and Orthoclase), as well as the calcite, the chert, and the sulfate-rich target (TSRICH) were not transformed into another phase and are mineralogically

homogeneous according to the Raman imaging done on the entire surface of the targets. Additionally, several targets were confirmed to be homogeneous in terms of structure and mineralogy at micro scale, and could clearly be used as reference for the Raman technique as well once on Mars. More details about Raman characterization of the targets can be found in [80].

LIBS analysis. In Spain, LIBS analysis was performed on one replicate of each calibration target. The LIBS spectra have been processed and the net intensity has been retrieved for some elemental lines, in order to calculate their RSDs. Taking into account the RSDs obtained [80], only the TSRICH target was considered as heterogeneous for some major elements. Nevertheless, as the purpose of that target is to monitor its sulfur signal (that could not be detected in Malaga's set up), this overall heterogeneity is not such a concern. Moreover, its S content was classified as homogeneous from the XRF results. Then, to a lower extent, three other targets showed some heterogeneity, but only for one element each and with the RSD always below 30 %. In France, several mathematical treatments were used on the LIBS spectra to check the homogeneity of the targets. In order to do so, the elemental lines of interest (major elements of each target) were fitted in order to get their peak areas. First, the GINI Index [115] was calculated from these peak areas. A GINI index below 0.25 means the target is considered homogeneous, between 0.25 and 0.5 it is fairly homogeneous, and above 0.5 it is heterogeneous. Using this technique, only the TSRICH target was again identified as heterogeneous (GINI index at 0.6). All the other targets have a GINI index below 0.25 for all their major elements [80]. Additionally, the RSD has been computed from the peak areas. Again, the TSRICH tar-

get presents the highest variability with a RSD around 26% for sulfur peak, which was acceptable given the difficulty to fit the S line. Two targets were fairly heterogeneous: JSC and TSERP, which is consistent with the previous LIBS study. The homogeneity has been also checked using some Independent Component Analysis [116, 117, 118] and only the TSRICH target showed a heterogeneous result.

Finally, coupling all these techniques to investigate the homogeneity of the targets with LIBS, it has been concluded that only the TSRICH target was heterogeneous at the LIBS spatial scale for most of the elements, besides SO_3 and K_2O that represent more that 70 wt% of the target. Therefore, heterogeneous elements in this sample do not constitute a major part of the target. LIBS analyses have shown that all the other targets are homogeneous at the LIBS scale (300µm, corresponding to the laser beam size), which is the main purpose of this work. The detailed results about homogeneity of the targets can be found in [80].

5.2. VISIR Spectra of geological targets

VISIR spectra were acquired in two laboratories, the University of Winnipeg (Canada) and the Institut de Planétologie et d'Astrophysique de Grenoble (IPAG) at Université Grenoble-Alpes (France). Different replicates of the calibration target materials were used in each laboratory, and the separate spectral acquisition methods are described below.

At the University of Winnipeg, reflectance spectra were collected with a Malvern-Panalytical Analytical Spectral Devices (ASD) LabSpec 4 Hi-Res

reflectance spectrometer. This ASD spectrometer consists of three separate detectors that cover the 350–1000 nm (Si photodiode array), 1000–1830 nm, and 1830–2500 nm (InGaAs detectors with moving gratings) intervals. A single 2 m long fiber optic cable was used to collect the reflected light from samples. This cable consists of 44 separate silica fibers with internal diameters of 200 µm each. The full diameter of the bundle was 1.85 mm. This fiber optic cable was fed to an optical scrambler that ensured light from each fiber was combined and equally fed to all three optical paths that fed the detectors. The Si photodiode array was then fed by a fiber optic bundle consisting of 19 separate 100-µm diameter silica fibers. The two InGaAs detectors were fed by separate fiber bundles consisting of 9 separate 200-µm diameter silica fibers. These offsets were removed by multiplicatively scaling the low (350–1000 nm) and high (1830–2500 nm) wavelength portions of the spectrum to the middle portion. The instrument has a spectral resolution that ranges between 3 nm for the photodiode array and 6 nm for the InGaAs detectors. Dark currents were removed from all spectra during correction to reflectance. These spectra were corrected for the absorption properties of the Spectralon reflectance standard, but were not corrected for the non-Lambertian behaviour of Spectralon. An in-house light source was used for illumination that consists of a quartz-tungsten-halogen (QTH) bulb illuminating a set of reflectors that feed the light through a pipe at a divergence of $<$1.5 degrees. The filament was operated at a temperature that provided sufficient output over the 350-2500 nm range. The measured spot was centered close to the center of the SCCT targets. Spectra were collected on the "unpolished" side of each target, even though it was done prior to the 9 LIBS

point analysis.

At IPAG laboratory, reflectance spectra of SCCTs were measured at IPAG using the Shadows instrument [119]. We used the standard mode of the instrument (around 7 mm diameter illumination spot) and spectra were measured under nadir illumination and using an observation angle of 30 ° (phase angle=30 °). Spectra were normalized to Spectralon and Infragold and corrected for the non-lambertian behavior of spectralon [120]. Spectra were acquired at a 10 nm sampling in the 400-4200 range, with a spectral resolution of 4.8 nm (<670 nm), 9.7 nm (670–1300 nm), 20 nm (1300–2500 nm) and 40 nm (2500–4200 nm).

The calibration targets acquired in laboratories with some of the most useful VISIR spectral signatures are shown in Figure 2. The RMI Red color target exhibits strong visible-wavelength "red" slopes whereas the Cyan target shows a major band centered near 1460 nm. Among the geologic targets, chert shows a hematite-like visible spectrum (with a peak near 750 nm followed by a strong downturn), resulting from minor hematite in the sample. The pyroxenes (Ferrosilite, Enstatite, and Clinopyroxene) exhibit characteristic bands in the 2000 nm region whose centers depend on Fe/Mg content and mineral structure [121]. Calcite includes signature bands near 2340 nm and 2530 nm. The orthoclase has few spectral features, except for a notable increase in reflectance toward shorter visible wavelengths. Finally, the Serpentine spectra exhibit a similar "blue" slope in the visible, hydration bands near 1400 nm 1910 nm, and a major band near 2312 nm and minor bands

near 2291 nm and 2391 nm that reflect contributions from both serpentine and talc (e.g., [122]). SuperCam VISIR spectra acquired from Mars are also shown for comparison in Figure 2. Even though these preliminary spectra are slightly more noisy, the same spectral features can be observed.

5.3. Raman Signature

Remote time-resolved Raman spectroscopy (SuperCam-like) spectra have been acquired at Institut de minéralogie, de physique des matériaux et de cosmochimie (IMPMC) of Sorbonne Université in Paris (France), with a Remote sensing and time-resolved Raman spectrometer in a SuperCam-like configuration. The remote configuration of a customized time-resolved Raman and luminescence spectrometer built at IMPMC was used for the present study [123, 124]. Relying on a conventional Schmidt-Cassegrain telescope (Celestron-C8 202 mm diameter Schmidt plate), this instrument allows analysis of the Raman and luminescence signals by using time-resolution spectroscopy. The laser is a nanosecond pulsed 532 nm DPSS laser (1.2 ns FWHM, 1 mJ per pulse) with a 10 to 2000 Hz repetition rate. The fine control and synchronization of both time delay and gating time of the ICCD allows sub-nanosecond time resolution experiments. For the present study, the laser beam was collimated at the sample surface (at 8 m from the telescope Schmidt plate) on a spot of $\sim$ 6 mm in diameter, with an irradiance on the sample of about $\sim 10^{10}$W.m^{-2} similar to that of SuperCam [124]. The Raman signal was collected by the telescope from a surface with slightly lower diameter than the co-aligned incident laser beam (field of view of the optical fiber of about 4.5 mm at 8m). A notch filter was used to cut off the Rayleigh scattering below 90 cm^{-1} and the signal was collected by an op-

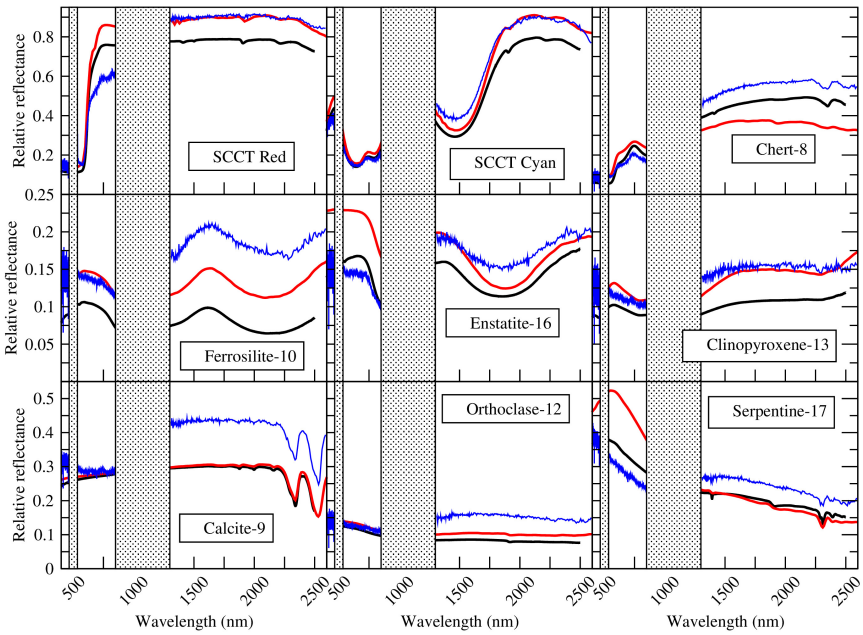

Figure 2: Laboratory and Mars spectra of SuperCam calibration targets that exhibit useful spectral features in the 400-2600 nm wavelength range (cf. Figure 1, Table 1). Spectra in black were acquired at the University of Winnipeg, and those in red were acquired at IPAG, Université Grenoble-Alpes. Blue spectra are those acquired on Mars. Stippled boxes represent regions where SuperCam does not collect data. All laboratory spectra were acquired at normal incidence and 30° emission angle. Differences in overall reflectance may occur owing to inherent differences in the target samples used by the different laboratories, and/or differences in corrections for the non-Lambertian nature of the Spectralon reference material (see text).

tical fiber and sent into a modified Czerny-Turner spectrometer (Princeton IsoPlane 320) coupled with an intensified Princeton PIMAX4 ICCD camera. This spectrometer has three motorized gratings that can be selected depending on the spectral window and spectral resolution requested for the analysis. Here we used the 600 lines/mm grating yielding a spectral resolution of 10-13 cm^{-1} similar to that of SuperCam. Here, we collected the spectra by using a 5 ns ICCD gate centered on the laser pulse. In order to maximize the signal-to-noise ratio, we accumulated the signal corresponding to hundreds of thousands of laser shots.

Not all the geological targets show a clear signal using remote time-resolved Raman spectroscopy. This can be due to their mineralogy, but also their structure and texture (*e.g.* grain size). For example, all the minor-doped targets are amorphous material and time-resolved Raman spectroscopy is not sufficiently sensitive to this material. Figure 3 shows a spectrum of all the targets that present the best signal: these are the calcite, the apatite, and the Sulfur-rich targets.

In the case of calcite, both internal (712 and 1087 cm^{-1}) vibrational modes and external lattices modes (282 cm^{-1}) are clearly observed. In the other carbonates, ankerite and siderite, only the most intense CO_3 internal symmetric stretching mode ν_1 at 1085–1090 cm^{-1} is clearly detected. Similarly, in apatite, the principal internal symmetric stretching mode ν_1 of PO_4 is observed at 960 cm^{-1} as well as other peaks corresponding to other internal vibrations of the PO_4 group. Last, the sulfur-rich target exhibits several peaks corresponding to the internal modes including an intense one at Ca,

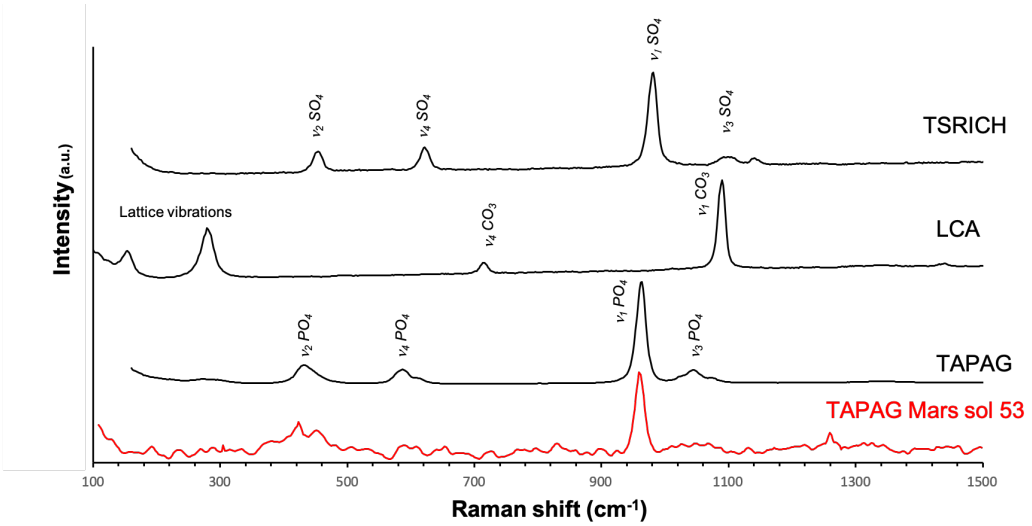

Figure 3: Time-resolved Raman spectra acquired remotely in a SuperCam-like configuration on the Apatite, Calcite and Sulfur-rich "TSRICH" calibration targets (in black). Spectrum of the apatite acquired on Mars is shown in red for comparison.

while the 1000-cm^{-1} line corresponds to the SO_4 internal symmetric stretching mode ν_1. The rover paint (not shown) is also interesting as it has a strong Raman signature with several bands at frequencies lower than 1000 cm^{-1}.

Since landing, Raman on SCCT has been used a few times, but only on the Apatite and Ertalyte (organic) targets. Figure 3 shows the apatite spectrum acquired on Mars as well. The apatite spectrum shown here was measured with 100 laser shots. The resulting spectrum is satisfying. The SNR is lower compared to the laboratory spectrum but this is likely due to the much lower number of laser shots used on Mars. However the main internal symmetric stretching mode ν_1 of PO_4 is clearly observed at 960 cm^{-1} as well as some other internal modes.

5.4. LIBS Spectra

One complete set of replicates (CR) were analyzed at Los Alamos National Laboratory (LANL) in New Mexico (USA) during the calibration campaign, using the FM BU and the EQM MU [2, 3]. They were placed at 1.56 m from the instrument (some of them were also sampled at 2.86 and 4.25 m), under Mars atmosphere (7 Torr of CO_2). The instrument was placed in a cold chamber, at $-15°C$. However, we present here only the spectra acquired on Mars for more clarity. The average LIBS spectrum obtained for some targets is presented in Figure 4 from UV to near infra-red, normalized to the total intensity. Only a few targets are presented for clarity, to visualize the diversity of signal obtained from one target to another.

The bottom spectrum, in dark blue corresponds to the calcite sample, where only Ca emission lines are observed (along with weak C lines and O, from the atmosphere). The ankerite, which is also a carbonate, is shown just above, in light blue. Along with the intense Ca peaks, the Fe and Mg emission lines are observed. The TSRICH target (in orange) is unusual, as it is a mixture between a basalt BHVO-2 and the K sulfate. Therefore, all the major elemental lines are observed, with huge K lines. Sulfur lines are weak compared to others and therefore are shown in a close-up (Figure 5).

BHVO-2 (pink in Figure 4) has a basaltic composition and therefore all major elements are present, with a complex LIBS signal. Orthoclase and Andesine targets (dark and light green, resp.) show mainly emission lines produced by alkali elements, Si, Ca and Al. Orthoclase shows higher K lines compared to the andesine. The apatite target (purple) has one of the highest Ca emission lines, and its spectrum in the UV (240-340 nm) and VIO (380-

470 nm) ranges is quite flat except for these peaks (such as for the calcite). However, its Tspec spectrum shows a clear CaF molecular band. Figure 5 also shows its Cl and P emission lines. This target is the unique one with such elements. Finally, the chert presents significant emission lines from only two major elements, Fe and Si. However, Fe is one of the elements with the highest number of emission lines, mainly in UV and VIO.

The targets doped in minor and trace elements show a wide range of signal concerning Sr, Rb, Cr, Li, and Ba due to their different doping in each of them (see section 3.2).This can be observed in the LIBS spectra in Figure 6), where they are shown with no offset in order to highlight their diversity. Unfortunately, no Ni peaks are detected in these targets, which suggests that their content is below the LOD. However, all the other minor and trace elements are clearly observed, with the signal intensity being consistent with the doping of each of these targets, as seen in Table 5.

6. SCCT compositions

Access to actual compositions of all the replicates is a necessity, as these targets will be used to check the quantitative models performed from the terrestrial database [30, 15, 16].

All the targets were analyzed with quantitative techniques in order to get their reference compositions for major and minor elements (Table 3. Electron Microprobe Analyses (EMPA) were performed at the micro-characterization center of Raimond Castaing, Université Paul Sabatier in Toulouse (France)

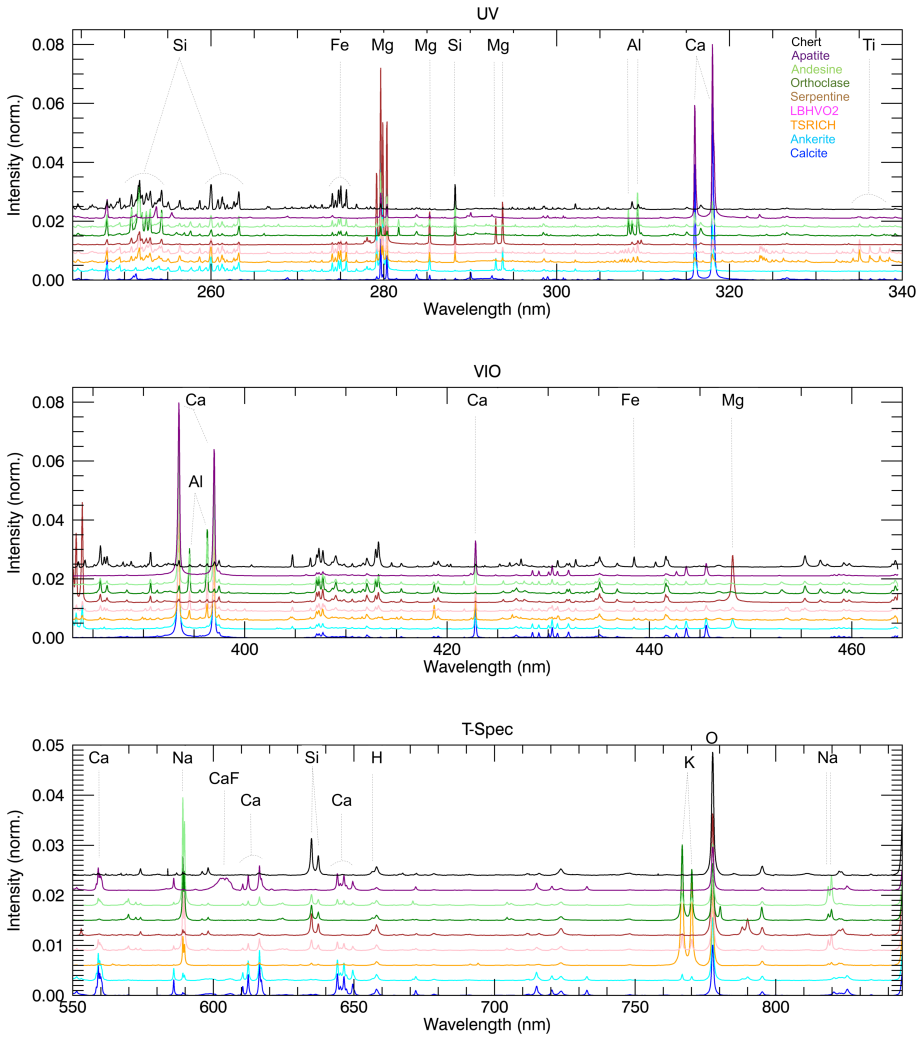

Figure 4: LIBS spectra (from UV to T-spec range) obtained on some of the SCCTs on Mars. Only a few examples are shown, to illustrate the diversity in LIBS signal.

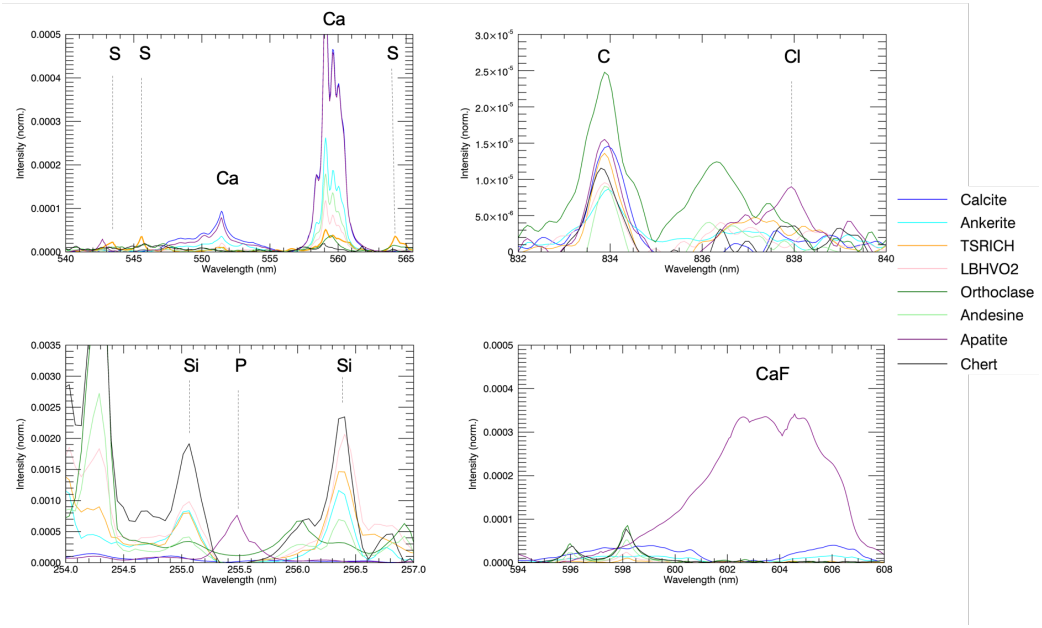

Figure 5: Close-up of some LIBS spectral portions to show specific signatures, particularly for the apatite (purple) and TSRICH (orange) targets.

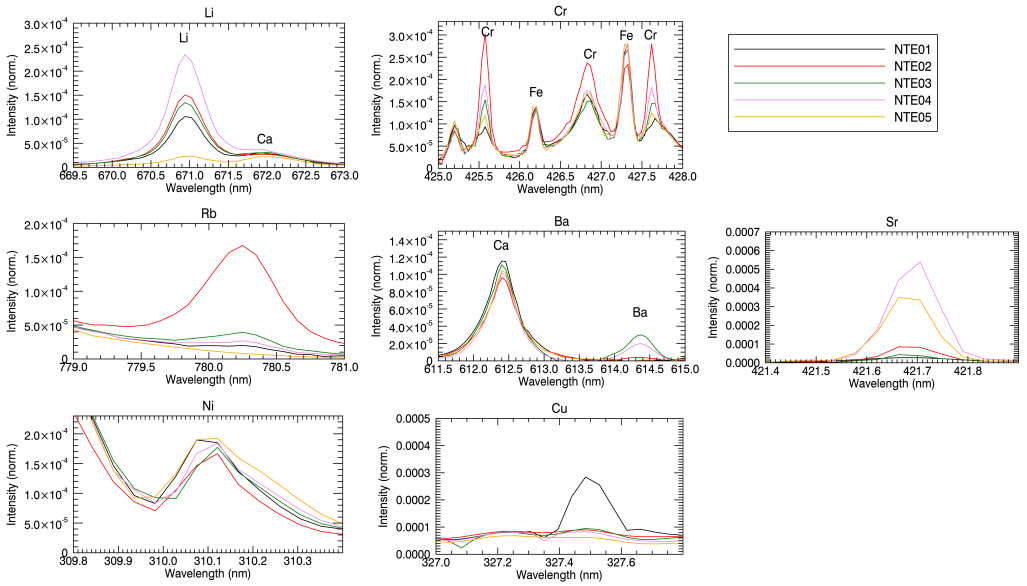

Figure 6: Close-up of spectral regions of the minor-doped targets for: Li, Cr, Rb, Ba, Sr, Ni, and Cu ranges.

and the Laser Ablation - Inductively Coupled Plasma - Mass Spectrometry (LA-ICP-MS) measurements were performed at ISTeP, ALIPP6 platform in Sorbonne Université in Paris (France).

The electron microprobe measurements were performed with a Cameca SXFive model. All the six replicates for each calibration target were analyzed, on the back of the target to prevent the surface. The analysis of all the six replicates was important in order to get the composition of all of them, and to make sure they were similar (because one is on-board, and the others are distributed in collaborating laboratories). The uncertainties of the EMPA technique are given in supplementary material, Table S2. To be consistent with the future LIBS analysis, and considering that the LIBS spot

size is around 250 µm, microprobe analyses were done over 3 random squares of 100 × 100 µm with a 2 µm analysis spot size. In each square, nine point analyses were performed. 10 to 15 manually selected points were performed as well, in order to make sure that all the different phases were sampled at least once. Thus, a total of 37 to 42 points were analyzed on each replicate. The average composition of the replicate was calculated from the average of the mean value calculated from each random square and from each series of 10–15 points. The standard deviation is calculated from these four averages. Finally, the RSD, used to assess the homogeneity of the sample, is calculated from the average composition and the standard deviation of the sample. This methodology gives a worst case scenario for the homogeneity compared to data from the LIBS analyses.

The LA-ICP-MS measurements were performed with a "QQQ" technique or triple quadrupole mass spectrometre (8800 Agilent), coupled with an ablation laser excimer 193 nm (Teledyne Analyte G2).The advantage of the triple quadrupole mass spectrometer is to strongly limit the isobaric interferences (oxides MO^+ and double charged M^{++}) due to the coupling with the laser ablation. Indeed, the passage of ions through two successive mass spectrometers, allows a doubled selection. We performed analyses along 8 lines of 1 mm, with a laser spot size of 200 µm. These lines give a better assessment of the composition (major and minor elements) than individual points. This technique is more sensitive for the detection of trace and minor elements than EMPA, but also the spot size is closer to the LIBS spot size. Thus LA-ICP-MS results will give a better comparison with LIBS data. As

previously checked by EMPA, all the replicates for each sample are similar [80] [see appendix], and therefore only the back of the Flight and Spare model replicates were analyzed with this technique. The average composition and the RSD obtained for each sample correspond to the average and deviation calculated on the 8 analyzed lines.

All the flight targets (except one, see below) were analyzed both with the EMPA and the LA-ICP-MS techniques. Figure 7a shows the major element compositions obtained for the flight targets from both techniques. Most of the points plot on the 1:1 line (in red), showing the very good agreement between the two techniques. Some analyses are farther away from the 1:1 line and correspond mainly to the standard targets (triangles) and natural targets (diamonds). However, when looking at the RSDs obtained from each quantitative technique (Figure 7b), these targets have much higher RSDs from the microprobe technique compared to those from the LA-ICP-MS/MS. We will conclude that this result is mainly due to the difference of the fields of view (2 µm compared to 200 µm) relative to the size of the grains/minerals constituting the sample.

This section will describe the differences observed between the two quantitative analyses, followed by the final compositions of the Flight Model calibration targets.

6.1. Standard targets

Among the 23 SCCTs, three of them correspond to standards: BHVO-2 (basalt - [64]), JMn-1 (Mn nodule - [66]) and JSC-1 (Mars soil analogue -

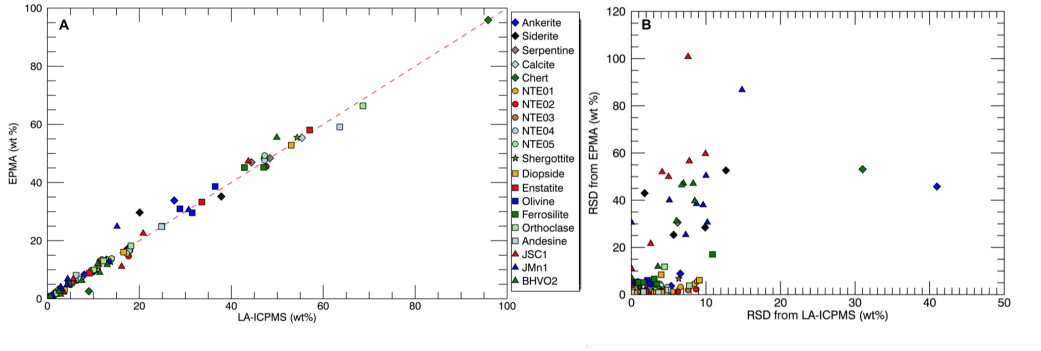

Figure 7: Comparisons of the results obtained between microprobe and LA-ICP-MS techniques. All major elements are shown here (SiO_2, TiO_2, Al_2O_3, FeOT, MgO, Na_2O, K_2O). Left: EMPA composition versus LA-ICP-MS compositions for all of the LIBS SCCTs. Right: RSDs obtained from the EMPA analyses vs RSDs obtained from the LA-ICP-MS analyses, for all major elements. RSD values represent the average scatter from the average composition obtained for the three squares and the 10 to 15 independent points; for the LA-ICP-MS results, RSD represents the variations of the average obtained from the eight scan lines.

[65]) samples.

We observed some discrepancy for these targets between the EMPA and LA-ICP-MS analyses, as seen in Figure 7a. Moreover, from the EMPA technique, RSDs from the accepted values can be as high as 60 % whereas with LA-ICP-MS the RSDs are much lower, less than 10 %. The reason is explained below, for each of the standard target.

Concerning the BHVO-2 target (green triangles in Figure 7), RSDs from the EMPA results go up to 50 % for most of the major elements. Indeed, Figure 8a shows a Back-Scatter Electron detector (BSE) image of this target (on the left), where at least 3 different phases can be easily detected: plagioclase (darker grains), pyroxene and olivine (brighter grains). The orange cross represents the EMPA spot size, which is clearly smaller than these three different mineral types, therefore explaining this high heterogeneity and the deviation to the composition deduced from EMPA compared to LA-ICP-MS/MS. Moreover, black areas between the grains represent voids, signifying that the surface state was not perfect. This is probably due to the presence of multiple phases in that sample; the polishing of the surface was difficult as many grains were being excavated during this process. The presence of these voids can affect the quality of the quantification, as they return a biased composition. The composition obtained from LA-ICP-MS is however in very good agreement with the known reference composition (Figure 9b).

Concerning the JMn-1 standard (blue triangles in Figure 7), a BSE image is shown in Figure 8b. Dark areas of more than 30 µm wide are observed

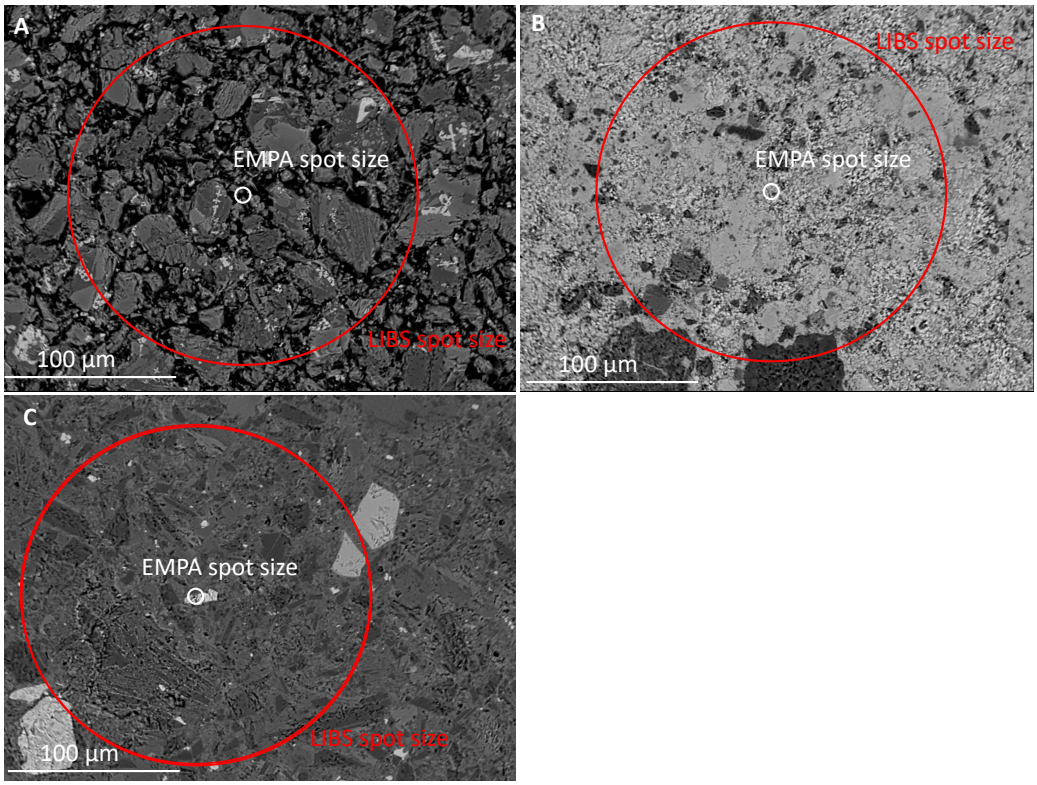

Figure 8: BSE images obtained on the Flight target of: A/BHVO-2; B/JMn-1; C/JSC-1. White circle represents the microprobe spot size, and red circle represents the LIBS spot size.

and correspond to quartz and feldspars. Even though the silicate phases are the most present, lots of very small bright grains are observed, which correspond to Fe or Mn oxides (this sample being chosen for these Mn oxides). When considering all the data points from the EMPA's predictions (Figure 10), we can observe a good agreement with the BSE image. Mn oxides are widespread, along with some Fe oxides, and these Mn oxides are enriched in Cu and Ni. Some feldspars can be detected as the SiO_2 is mainly correlated with Al_2O_3 and alkalis, even though some pure quartz has been

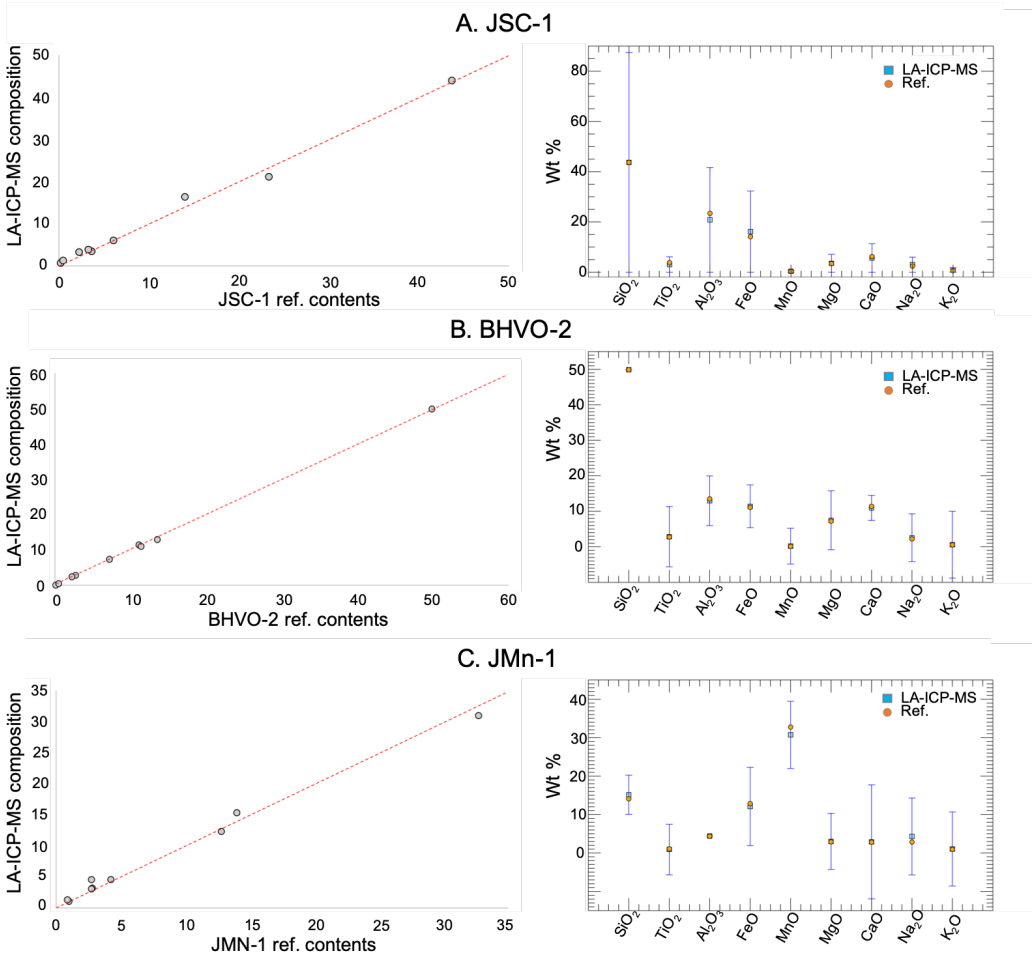

Figure 9: Comparison between compositions obtained from LA-ICP-MS on the Flight Model replicate and from their reference compositions. A. JSC-1 standard; B. BHVO-2 standard; C. JMn-1 standard. In the left column, red dashed line correspond to the 1:1 line. In the right column, the blue error bars correspond to the RSDs obtained from LA-ICP-MS/MS. Reference values come from [66] for the JMn, [64] for BHVO-2, and [65] for JSC. Details can be found in Table S1

sampled (but still quite rare). This reveals at least four different phases in this sample, most of them giving a sum of oxides far from 100 wt %. These observations can explain the higher Si content (25 wt%) obtained from the EMPA technique compared to the result from the LA-ICP-MS (15 wt % SiO_2), that is more representative of the bulk. The EMPA technique, even though performed with 40 to 50 points on this specific target emphasizes this heterogeneity that is clearly linked to the poly-crystallinity of that sample, with a high abundance of Mn oxides.

Due to its larger spot analysis, the LA-ICP-MS results are more consistent with the bulk composition. Figure 9c shows the comparison with its reference composition [66]. Most elements are on the 1:1 line, even though a few small differences can be observed mainly for the SiO_2 and MnO contents, and to less extent for Na_2O and FeO contents. However, the reference composition is within the variations observed in the LA-ICP-MS measurements.

The JSC-1 standard (red triangles in Figure 7) differs mainly about its iron content that is higher from the LA-ICP-MS compared to the EMPA results (17.9 wt % for 11 wt %, resp.), but this is the target with the highest dispersion for all its major elements from the EMPA analyses. In LA-ICP-MS/MS, its RSDs are acceptable, lower than 10 %. The variability observed in EMPA is mainly explained by the presence of Fe and Ti oxides in that sample, that are clearly observed on the BSE image (Figure 8c, bright small grains) and the EMPA analyses. The LA-ICP-MS composition are more representative of its bulk, even though some differences are observed from the reference composition (Figure 9a). The main differences concern the Al_2O_3

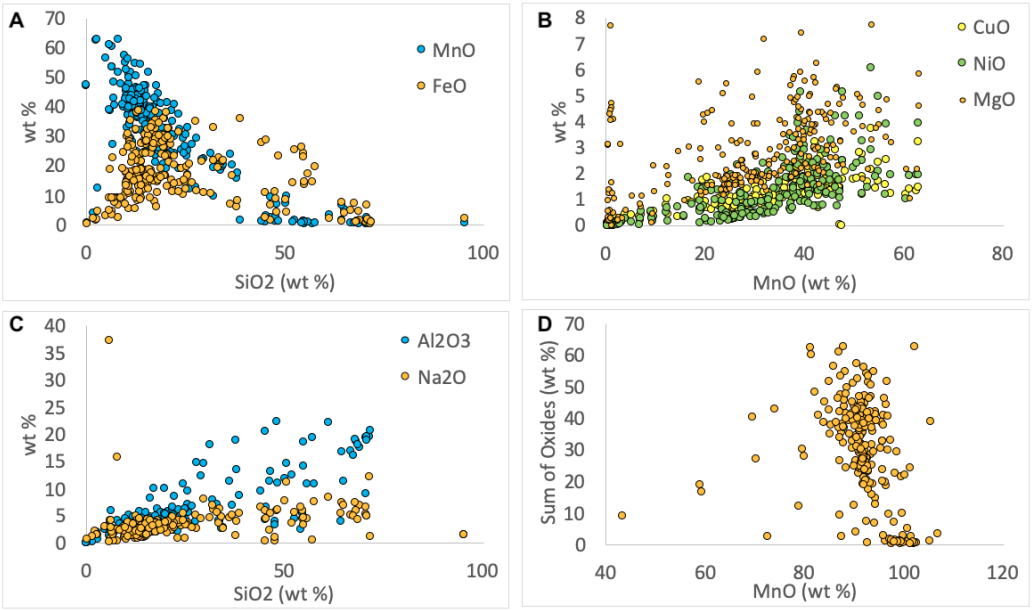

Figure 10: EMPA results obtained for JMn. All the 35 points are shown, for several elements. High values of MnO and FeO are observed for low SiO_2 content. These high Mn locations are also enriched in Ni and Cu.

and FeO contents, but the variations observed in LA-ICP-MS data are larger than the difference between our measurement and the reference value.

The JMn-1 target is the worst sample in terms of chemical quantification, which was expected as this sample was chosen for its content of Mn oxides, whereas BHVO-2 and JSC-1 samples also show much more variability than expected in terms of mineral phases. That is why only the LA-ICP-MS values are reported in Table 4, as the scanning lines are more representative of the bulk chemistry for these poly-crystalline targets. Comparison of the LA-ICP-MS quantifications for these targets with their reference values (Figure 9) reveals that they are really close to each other, reinforcing our choice for

the LA-ICP-MS technique for these particular targets. The table of compositions from the literature and from LA-ICP-MS is shown for these three standards in the supplementary material (Table S1).

Figure 11 from LA-ICP-MS data shows that the major elements for these standard targets (represented by triangles) have a RSD < 10 %, except for the JMn-1 with the CaO that has a RSD at 14.8 %. However, with RSD <15 %, these targets are homogeneous at the LA-ICP-MS scale. Even the minor elements of these targets have RSD overall <15 %, except Cr that is up to 40 %. JSC-1 has 0.1 wt % of Sr (RSD 8.8 %), JMn-1 contains 0.18 wt % of Ba (RSD 12 %), 1.47 % Ni (RSD 9.7 %), 1.35 % Cu (RSD 10.4 %), and 0.1 % Zn (RSD 11.6 %).

6.2. Natural rocks

Among the natural targets (calcite, ankerite, siderite, serpentine and chert), the ankerite, siderite and chert have LA-ICP-MS results that differ from the microprobe ones, as can be observed on Figure 7a (diamonds).

The ankerite and siderite have LA-ICP-MS and EPMA results that differ mainly for their CaO content, which is higher in microprobe than in LA-ICP-MS (33 wt % vs 27.6 wt % for ankerite, 29.6 wt % vs 20 wt % for siderite, Table 4). In the case of the siderite, the two techniques also differ for the FeO content, which is higher in LA-ICP-MS/MS. Their RSDs are also clearly higher from the EMPA analyses, even for the main element of these samples. These differences in composition and variability are also related to several phases in these samples. The siderite shows from the EMPA analyses (Figure 12a) that at least three different phases have been sampled: Fe ox-

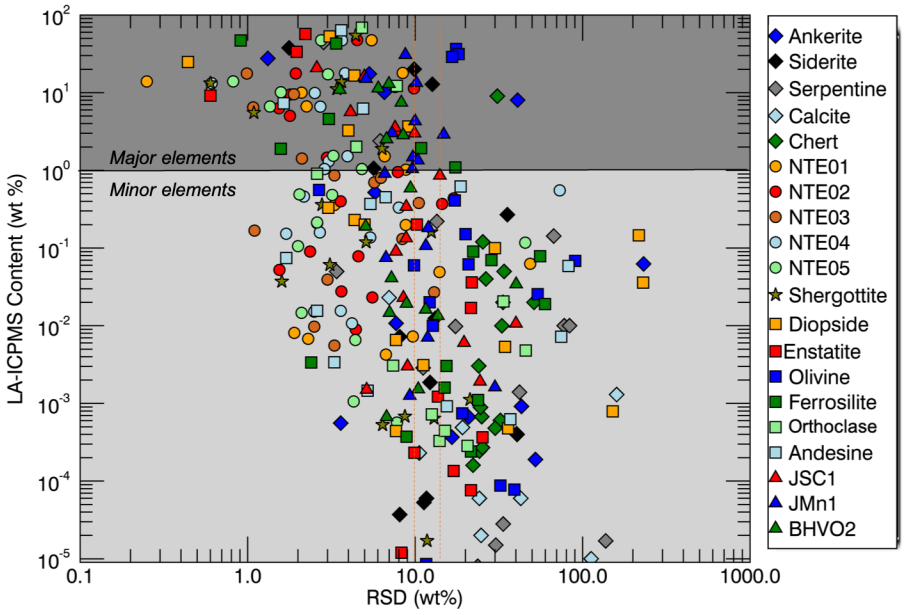

Figure 11: RSDs obtained from the LA-ICP-MS technique depending on the elemental content. All quantified major and minor elements are shown (Si, Ti, Al, Fe, Mn, Mg, Ca, Na, K, Si, Li, Rb, Cr, Ba, Ni, Cu, Zn). Red dashed vertical lines correspond to 10 % and 15 % RSD for clarity.

ides, a silicate phase, and a calcite. This can be explained by two factors: i) the siderite chosen is not pure, *i.e.* it contains some silicates; ii) during the flash-sintering process, the siderite mineral dissociated to become calcite with some Fe oxides. This phenomena is explained in [10], and the consequences are also observed in the Raman signal for that target [80]. Concerning the Ankerite, high RSD is observed for SiO_2 only, as observed by both techniques (even though lower in LA-ICP-MS/MS). EMPA data show that this target actually contains some quartz grains (Figure 12b), as observed with Raman as well [80].

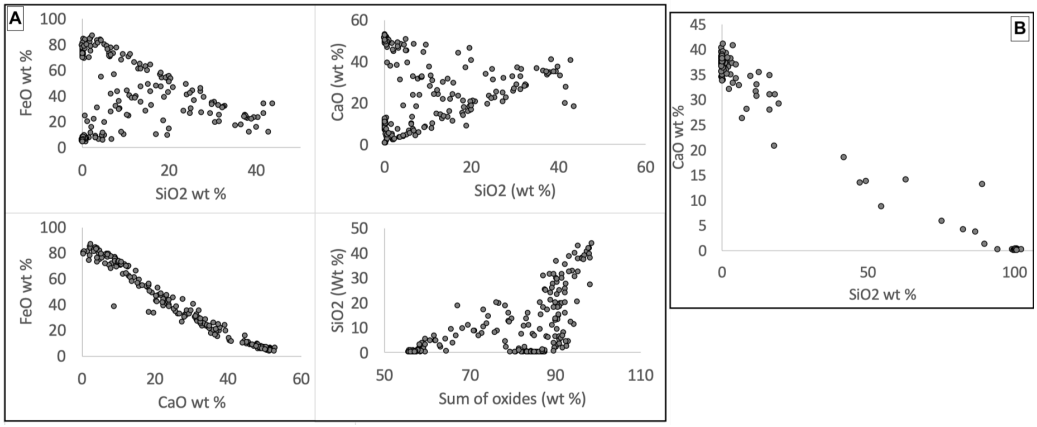

Figure 12: Microprobe data obtained in the siderite (A) and in ankerite (B).

The chert is the only target that is not from a sintering process. Therefore some impurities and variations in composition are possible. Its LA-ICP-MS and EMPA data differ (Figure 7, green diamond), especially regarding its iron content, which was expected as the Marble bar chert has a lot of jaspar bands running through it 13. This target, almost pure SiO_2, contains

a significant amount of FeO with an elevated RSD (31 % from LA-ICP-MS vs 53 % from EMPA - Figure 7b). EMPA data, due to the very small scale analysis, revealed some points enriched in FeO, and low in SiO_2 (Fig 13). The FeO content is too low to come from a sampling of pure Fe oxides (< 30 %), but is anticorrelated with all other possible elements (as shown with SiO_2). Moreover, the BSE image shows very small bright spots (<1µm) that correspond to Fe oxides and that are scattered all over the target surface. Therefore these higher abundances in FeO in some points correspond to some mixtures between the chert and Fe oxides, too small to be sampled individually even with the EMPA technique. This explains the overall lower FeO content (but higher RSD) obtained with the EMPA technique, compared to the results from LA-ICP-MS/MS. The LA-ICP-MS technique, with a bigger spot size and a scanning line, is more representative of the bulk composition.

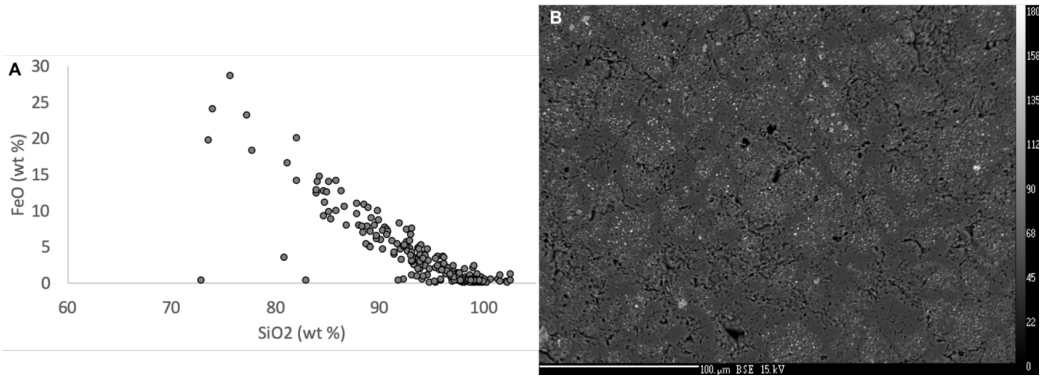

Figure 13: Microprobe data (FeOT vs SiO2) obtained in the chert (A) and BSE image of this target (B).

Microprobe data for the calcite target show that it is almost entirely pure Ca carbonate, with no silicate or Fe oxides. RSDs are very low for the CaO

(< 3 %, Table 4). The CaO content is 55.4 wt %, which is stoichiometrically consistent with a natural calcite. The CO_2 content can therefore be estimated at 43.9 wt%. The CaO being the only major element of that target, it was used as the internal standard for the LA-ICP-MS data normalization, and therefore is not reported in Table 4.

The last natural target is the serpentine. Compositions from EMPA and LA-ICP-MS are very close to each other (Figure 7 and Table 4), with RSD values much lower from the LA-ICP-MS analyses. However, the main difference concerns the MgO content that is lower from the LA-ICP-MS compared to EMPA (44.4 wt % compared to 46 wt % respectively), with comparable RSDs (Table 4). This target is of great interest also for its H_2O content. It has been measured using Thermal Gravity Analysis (TGA) technique at IPAG (Grenoble, France) and estimated as well using the ChemCam-LIBS technique, with the same methodology as the one developed in [96]. The water content is between 1 and 3 wt% H_2O, which is consistent with the overall composition obtained from LA-ICP-MS and EMPA (the sum of oxides is at 95-98 wt% from LA-ICP-MS and 100-102 wt% from EMPA, when taking into account the H_2O content).

6.3. Minor-element-enriched targets and shergottite

These targets (NTE01, NTE02, NTE03, NTE04 and NTE05) show similar major-element results for LA-ICP-MS and microprobe analyses, with very low RSD for major elements (<10 %, Table 4). Moreover, they all have a similar composition in terms of major elements, except NTE02 that has a lower content in most of them to compensate its MnO enrichment (> 4 wt

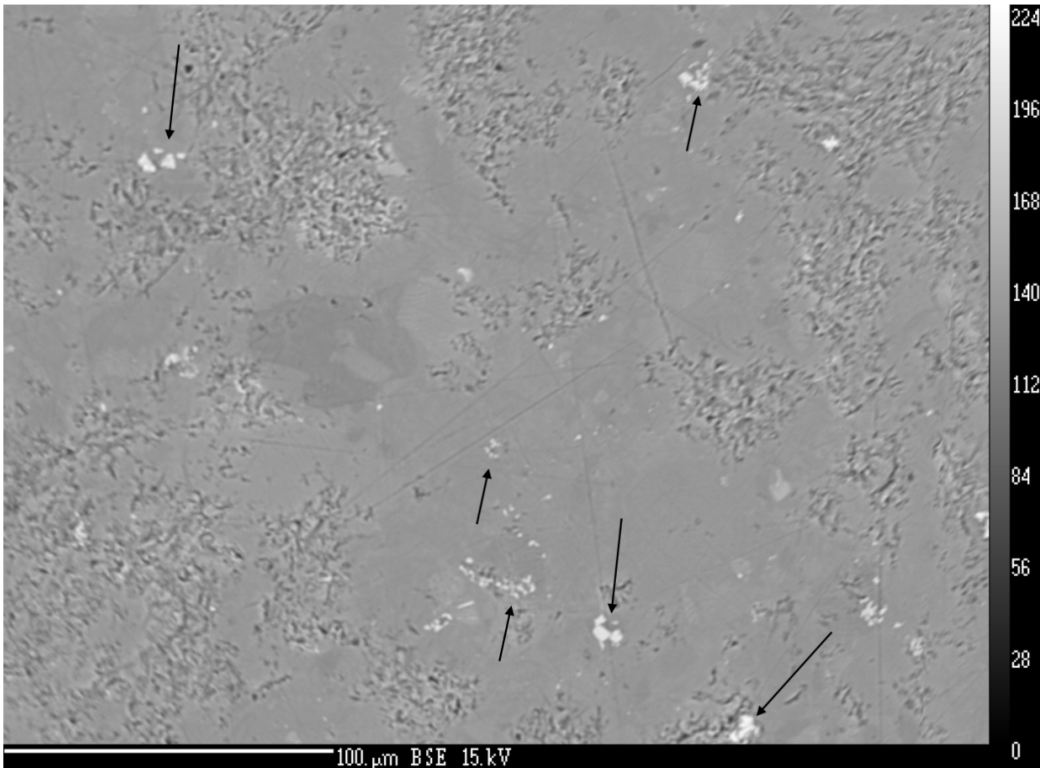

Figure 14: BSE image from the NTE04 flight model. Bright spots correspond to Cr oxides.

%). In Figure 11, these targets are represented by circles. Even for their minor element concentrations, their RSDs are lower than 20 % except for a few exceptions, such as the Cr for NTE04 (light blue circle). In this target, there is 0.55 wt % of Cr_2O_3, which is the highest amount of Cr in all the calibration targets. Cr is known to form chromites when its content is elevated [27], which can explain the elevated RSD at 73 % for the Cr content. Chromites are indeed observed in the BSE image (Figure 14), corresponding to the bright spots. Nevertheless, besides Cr, the RSDs obtained for the minor elements in these targets are mostly below 10 wt %, which make them very useful for the minor elements' calibration.

Minor and trace element's quantification is given in Table 5, for these particular targets along with all the others.

The shergottite target is a replicate from ChemCam Calibration targets [27]. Besides the SPS process, it has been made from the same methodology as the minor-doped targets, and therefore is a glassy material, and very homogeneous. Both quantitative techniques give very comparable results. Observed differences are smaller than the RSDs of both techniques, as seen for the Si and Ca contents (1 wt% difference for the SiO_2 content, with RSDs between 2 and 4% and 1 wt% difference in the CaO content with 3% RSD for both techniques.

6.4. Primary Igneous Minerals

Quantitative analyses of these targets (Andesine, Diopside, Enstatite, Olivine, Ferrosilite) are presented in Table 4. The LA-ICP-MS compositions are similar to the EMPA results (squares in Figure 7-1). A few differences can still be observed, as these samples correspond to natural minerals and therefore a few impurities can still be present. Nevertheless, LA-ICP-MS measurements give generally smaller RSDs, as the analysis spot size is wider.

Figure 15ab shows the quantitative values of these feldspars, pyroxenes and olivine in their respective ternary diagram, where the LA-ICP-MS values are represented by squares and the EMPA values by circles. It can be observed that the composition (obtained from both techniques) falls into the appropriate field for each target. Olivine is calculated to be a Fo_{64} from LA-ICP-MS and Fo_{65} from EMPA, which is in concordance with the description of this natural target. One difference can be noted though, concerning the an-

desine: the Ca content is higher from the EMPA than from the LA-ICP-MS result (8.07 wt% vs 6.24 wt%, rep). To a lesser extent, the EMPA results for the orthoclase target also show a slight enrichment in K_2O compared to the LA-ICP-MS predictions (13.03 vs 12.23 wt%, resp.). This can be observed as well in Table 4, and in Figure S1 in supplementary material. In both cases, the EMPA technique gives Si and alkali contents closer to the theory. Besides the fact that both techniques give appropriate results with a sum of oxides around 100 wt%, it seems in this case that the EMPA technique gives results more consistent with the expected stoichiometry. However, in Figure 15c it can be noted that both techniques give a similar result in the Al/Si vs (Fe+Mg)/Si plot. One reason to include mineral targets among the SCCT was to enable creation this type of reference plot, in order to better constrain our quantitative models for Martian igneous rocks. In that sense, both techniques give consistent compositions and can be used for reference.

In Figure 11, these mineral targets are represented by squares. It can be observed that the RSD values for major elements (>1 wt%) are below 10% relative error. Concerning the minor elements, some show a high RSD, such as the diopside (orange square) with a RSD $>$ 100 % for the Cr, Ni and Cu elements (1461, 360 and 7.8 ppm, resp.), but most of the minor elements have a RSD below 40 % for the Orthoclase (light green squares), with only 20 % RSD for Sr, present at 2.9 ppm. Rb, which substitutes easily with K, is elevated (0.9 wt %) and has a low RSD (2.6 %). Also, for minor elements are all $<$ 25 % for the Enstatite target (red squares).

In summary, these results show that these minerals are overall homogeneous with very few impurities.

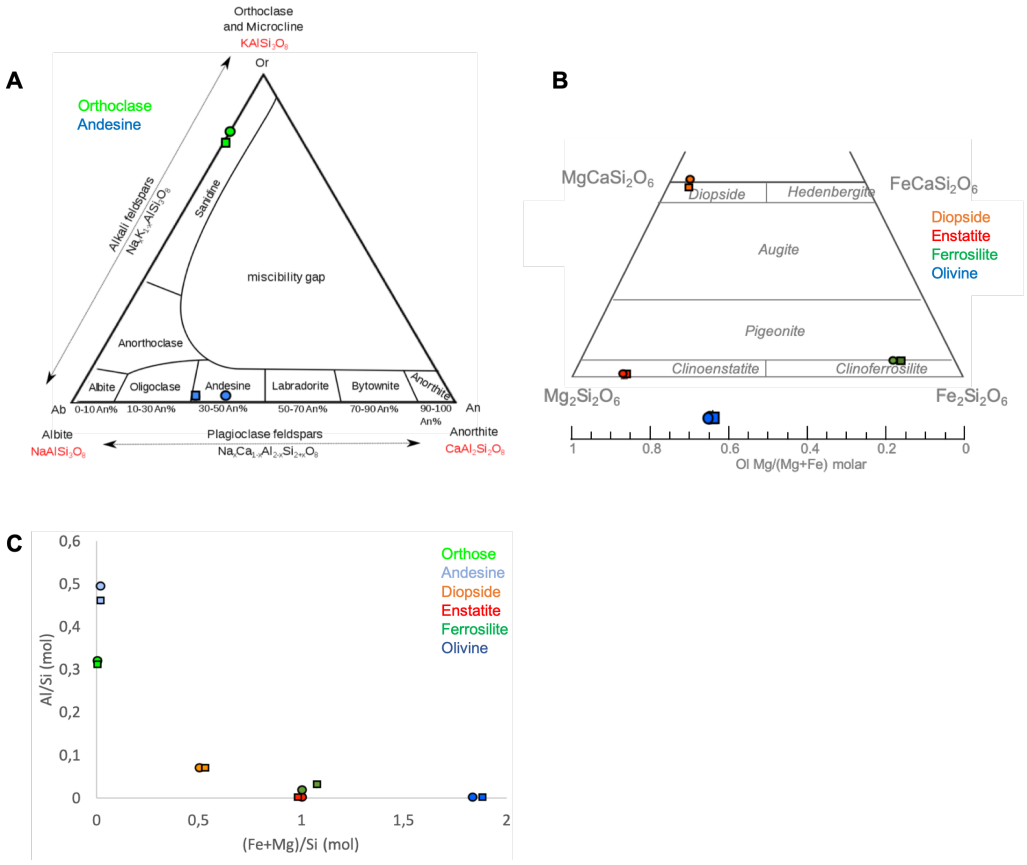

Figure 15: A.Ternary diagram for feldspars; B. Ternary diagram for pyroxenes and Mg number for olivines; C. Al/Si vs (Fe+Mg)/Si plot in molar ratios to show the reference compositions of these minerals. LA-ICP-MS values are represented by squares and EMPA values by circles.

6.5. Synthetic targets

The synthetic targets (TSRICH and Apatite) were not sampled with the LA-ICP-MS technique. The Apatite being a phosphate, this would have required a different setup for the LA-ICP-MS method due to the important isobaric interferences on mass ^{31}P. Moreover, as this target was designed stoichiometrically, its composition was checked frequently using the EMPA technique, which demonstrated a very homogeneous sample with RSDs < 12 % (Tables 4, 5, and Figure 11). Besides the calcium, it contains 41.65 wt% P_2O_5, with 2.98 wt% Cl, 1.82 wt% F, along with 0.016 wt% H. The apatite chosen for the flight model (called "TAPAG") is represented in a ternary diagram where the apatites found in meteorites are overplotted [101], as well as apatites observed with ChemCam on MSL (blue area) [103] (Figure 16).

The TSRICH target was not analysed by LA-ICP-MS technique either (nor with EPMA), due to technical issues and the lack of reference for the sulfur content. However, a good estimation of its composition can be made from the known composition of its components, which are the BHVO-2 basalt and a commercial K sulfate. Even though this target has been shown to be relatively heterogeneous for most of its elements from LIBS and XRF analysis [80], K and S are overall homogeneous in this sample, at least at the LIBS scale (see part 5.1). Table 4 shows that it contains almost 40 wt% K_2O and 32 wt % SO_3 based on its theoretical content. Even though these contents are only theoretical (not measured), they are nonetheless consistent with the XRF observations [80].

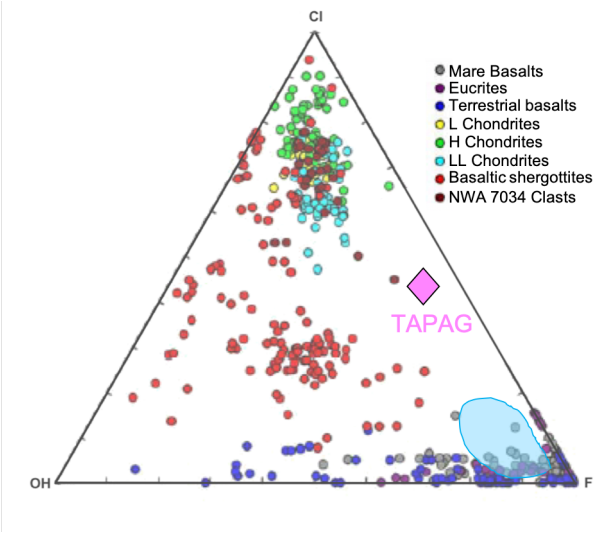

Figure 16: Cl, F, H ternary diagram modified from [101]. Apatites found on the Moon, terrestrial basalts and Mars meteorites are shown in circles [125, 126, 127, 128, 129, 130]. Apatites found by ChemCam at Gale crater are represented by the blue area [103]. The TAPAG sample, on-board the Perseverance rover, is represented by a pink diamond.

		SiO2				TiO2				Al2O3				FeO				MnO				MgO				CaO				Na2O				K2O			
		LA-ICPMS		EPMA		LA-ICPMS		EPMA		LA-ICPMS		EPMA		LA-ICPMS		EPMA		LA-ICPMS		EPMA		LA-ICPMS		EPMA		LA-ICPMS		EPMA		LA-ICPMS		EPMA		LA-ICPMS		EPMA	
Type	Target_Name	wt %	*RSD (%)*	wt %	*RSD (%)*	wt %	*RSD (%)*	wt %	*RSD (%)*	wt %	*RSD (%)*	wt %	*RSD (%)*	wt %	*RSD (%)*	wt %	*RSD (%)*	wt %	*RSD (%)*	wt %	*RSD (%)*	wt %	*RSD (%)*	wt %	*RSD (%)*	wt %	*RSD (%)*	wt %	*RSD (%)*	wt %	*RSD (%)*	wt %	*RSD (%)*	wt %	*RSD (%)*	wt %	*RSD (%)*
Ankerite	LANKE0101	8.03	*40.97*	8.32	*45.78*	0.00	/	/	/	0.44	*27.27*	0.42	*104.88*	10.14	*6.56*	9.46	*8.92*	0.52	*5.77*	0.49	*1.27*	17.46	*5.33*	17.25	*3.68*	27.59	*1.32*	33.83	*1.62*	0.03	*33.33*	0.03	*50.36*	0.11	*36.36*	0.10	*25.90*
BHVO2	LBHVO20406	49.90	/	-		2.84	*8.49*	-		12.98	*6.98*	-		11.39	*6.03*	-		0.19	*5.04*	-		7.47	*8.28*	-		10.96	*3.55*	-		2.53	*6.75*	-		0.59	*9.39*	-	
Calcite	LCA530106	0.05	*68.30*	0.02	*73.14*	0.00	/	/	/	0.01	*0.00*	0.01	*58.90*	0.01	*31.07*	0.01	*44.89*	0.00	/	0.02	*47.25*	0.22	*6.63*	0.19	*15.45*	/	/	55.38	*2.33*	0.01	*16.45*	0.02	*58.05*	0.00	/	0.01	*55.25*
Chert	LCMB0006	/	/	95.90	*1.92*	0.00	/	0.00	*74.94*	0.12	*25.40*	0.04	*64.90*	9.02	*31.04*	2.59	*53.12*	0.00	*33.04*	0.01	*16.30*	0.04	*26.54*	0.00	*25.47*	0.05	*34.17*	0.07	*111.37*	0.02	*33.50*	0.00	*47.98*	0.02	*51.30*	0.01	*63.47*
JMn1	LJMN10106	15.14	*5.09*	-		0.91	*6.59*	-		4.41	*0.00*	-		13.41	*10.18*	-		30.73	*8.75*	-		3.02	*7.28*	-		2.90	*14.83*	-		4.30	*10.00*	-		1.04	*9.62*	-	
JSC1	LJSC10304	43.70	/	-		3.05	*7.76*	-		20.83	*2.59*	-		16.15	*4.98*	-		0.34	*8.86*	-		3.55	*7.60*	-		5.65	*4.12*	-		3.00	*9.93*	-		0.86	*14.06*	-	
Siderite	LSIDE0101	12.85	*12.68*	13.46	*52.60*	0.00	/	/	/	0.02	*0.00*	0.03	*62.93*	37.82	*1.77*	35.21	*42.97*	0.05	*0.00*	0.06	*36.46*	1.06	*5.66*	1.26	*25.33*	20.07	*9.89*	29.69	*28.45*	0.02	*0.00*	0.03	*45.04*	0.01	*0.00*	0.03	*20.88*
NTE01	NTE010301	47.30	*5.50*	48.04	*1.26*	0.49	*2.04*	0.53	*2.74*	10.01	*2.10*	9.79	*1.53*	17.94	*8.44*	16.56	*4.51*	0.12	*0.00*	0.12	*3.92*	6.66	*2.25*	6.58	*1.55*	13.95	*0.25*	13.73	*1.72*	1.52	*6.58*	1.12	*3.24*	1.02	*8.82*	1.01	*5.63*
NTE02	NTE020106	47.62	*4.51*	45.51	*1.20*	0.37	*14.51*	0.46	*2.05*	9.47	*1.80*	8.98	*2.17*	17.67	*1.94*	14.66	*5.33*	5.03	*1.79*	4.81	*5.56*	6.31	*1.54*	6.22	*1.54*	11.37	*9.85*	12.94	*2.30*	1.46	*2.98*	1.14	*5.58*	0.95	*7.89*	0.99	*7.53*
NTE03	NTE030106	47.13	*3.59*	48.37	*0.73*	0.38	*10.53*	0.50	*2.25*	9.54	*1.89*	9.82	*1.56*	17.64	*0.99*	16.85	*0.87*	0.70	*5.71*	0.70	*1.05*	6.47	*1.08*	6.60	*3.84*	11.84	*7.60*	13.51	*1.93*	1.42	*2.11*	1.10	*4.24*	0.80	*6.25*	0.85	*4.32*
NTE04	NTE040106	47.24	*3.66*	47.64	*3.53*	0.46	*2.17*	0.50	*4.98*	9.91	*2.52*	9.72	*2.67*	17.81	*3.82*	16.55	*4.52*	1.31	*3.05*	1.38	*2.57*	6.61	*2.72*	6.62	*2.06*	13.22	*0.61*	13.38	*4.21*	1.52	*3.95*	1.22	*3.92*	1.04	*2.88*	1.03	*5.61*
NTE05	NTE050301	47.26	*2.75*	49.26	*1.29*	0.49	*2.04*	0.52	*2.17*	10.13	*1.58*	9.95	*1.01*	17.25	*3.02*	15.60	*3.86*	0.15	*0.00*	0.15	*9.65*	6.64	*1.36*	6.62	*1.30*	13.97	*0.82*	13.86	*1.18*	1.54	*3.25*	1.18	*1.92*	1.04	*4.81*	1.09	*3.18*
Andesine	PMIAN0106	63.60	*3.62*	59.09	*0.93*	0.02	*100.00*	0.02	*45.64*	24.84	*0.00*	24.84	*0.98*	0.62	*18.70*	0.59	*30.18*	0.04	*0.00*	0.04	*13.68*	0.45	*6.67*	0.48	*10.13*	6.24	*4.89*	8.07	*1.96*	7.30	*1.64*	6.68	*1.21*	0.37	*5.41*	0.45	*8.36*
Diopside	PMIDN0302	53.04	*3.09*	52.84	*0.82*	0.23	*4.35*	0.27	*7.22*	3.26	*3.99*	3.13	*8.43*	3.68	*9.12*	3.05	*6.11*	0.33	*3.03*	0.29	*11.07*	16.60	*4.34*	16.04	*0.98*	24.89	*0.44*	24.96	*0.61*	0.20	*5.00*	0.15	*8.26*	0.10	*30.00*	0.02	*41.03*
Enstatite	PMIEN0602	57.05	*2.21*	58.08	*0.11*	0.02	*0.00*	0.03	*34.90*	0.09	*22.22*	0.11	*33.91*	9.14	*0.60*	8.81	*4.90*	0.04	*0.00*	0.04	*24.45*	33.59	*1.96*	33.27	*1.32*	0.20	*10.26*	0.26	*26.31*	0.01	*0.00*	0.02	*41.99*	0.00	/	0.01	*30.12*
Olivine	PMIFA0306	38.62	/	38.62	*5.23*	0.02	*0.00*	0.03	*79.70*	0.06	*25.52*	0.06	*156.55*	31.50	*2.15*	29.59	*6.06*	0.44	*3.02*	0.40	*3.58*	31.10	*2.51*	30.94	*4.51*	0.61	*20.80*	0.60	*125.45*	0.01	*21.01*	0.02	*121.12*	0.00	/	0.01	*36.80*
Ferrosilite	PMIFS0505	42.87	*3.38*	45.14	*4.59*	0.02	*0.00*	0.03	*10.03*	1.09	*17.43*	0.62	*33.66*	47.04	*0.91*	45.24	*5.20*	1.90	*1.58*	2.00	*5.15*	4.58	*3.06*	5.11	*6.62*	1.93	*10.88*	1.92	*17.02*	0.09	*22.22*	0.04	*26.45*	0.07	*28.57*	0.04	*34.93*
Orthoclase	PMIOR0507	68.64	*4.81*	66.37	*0.75*	0.00	/	0.00	*54.81*	18.18	*0.00*	18.18	*0.75*	0.41	*17.28*	0.30	*31.93*	0.01	*0.00*	0.02	*45.47*	0.04	*50.00*	0.02	*60.16*	0.05	*66.67*	0.02	*41.16*	2.02	*4.46*	1.82	*11.81*	12.23	*7.77*	13.03	*3.77*
Shergottite	SHERG02	54.33	*4.42*	55.48	*2.04*	0.36	*2.78*	0.36	*5.65*	11.14	*3.41*	10.93	*0.40*	13.24	*0.60*	12.84	*4.56*	0.00	/	0.01	*41.53*	5.51	*1.09*	5.58	*4.01*	13.73	*3.64*	12.68	*2.95*	1.89	*6.35*	1.82	*6.73*	0.16	*12.50*	0.17	*8.49*
Serpentine	TSERP0102	48.39	/	48.39	*4.16*	0.01	*77.91*	0.00	*141.41*	0.22	*13.49*	0.68	*135.14*	2.40	*6.19*	3.20	*30.56*	0.05	*3.40*	0.05	*21.45*	44.40	*2.84*	46.95	*3.17*	0.01	*83.61*	0.01	*50.05*	0.00	/	0.01	*44.74*	0.00	/	0.01	*33.28*
Apatite	TAPAG0205	/	/	/	/	/	/	/	/	/	/	/	/	/	/	/	/	/	/	/	/	/	/	/	/	/	/	54.85	*0.37*	/	/	/	/	/	/	/	/
		SiO2 (wt %) - theoretical				TiO2 (wt %) - theoretical				Al2O3 (wt %) -theoretical				FeO (wt %) - theoretical				MnO (wt %) - theoretical				MgO (wt %) - theoretical				CaO (wt %) - theoretical				Na2O (wt %) - theoretical				K2O (wt %) - theoretical			
S-rich basalt	TSRICH0404	14.97				0.82				4.05				3.32				/				2.17				3.42				0.67				37.99			

Table 4: LA-ICP-MS/MS and EMPA compositions for major elements in all the LIBS SCCT targets (except for the TSRICH target that is theoretical). '-' refer to measurements not shown in table (only LA-ICP-MS given). '/' refers to not measured elements.

Type	Target_Name	Sr	RSD (%)	Li	RSD (%)	Rb	RSD (%)	Cr	RSD (%)	Ba	RSD (%)	Ni	RSD (%)	Cu	RSD (%)	Zn	RSD (%)	H (wt %)
Ankerite	LANKE0101	107.4	7.7	5.6	3.6	4.0	40.7	9.2	43.2	6.7	20.9	3.7	16.6	1.9	52.4	625.5	231.6	
BHVO2	LBHVO20406	410.7	7.2	6.7	6.8	15.3	10.5	342.4	40.2	192.6	8.9	134.0	13.7	162.1	11.6	147.2	7.0	
Calcite	LCA530106	232.9	7.0	0.2	24.8	0.1	112.6	13.0	159.9	2.3	10.6	0.6	24.2	0.6	42.8	4.9	19.2	
Chert	LCMB0006	2.4	**24.2**	1.6	**22.2**	6.1	**32.3**	2.7	**25.8**	6.8	**25.0**	8.9	**24.6**	4.8	**30.1**	30.4	**24.0**	
JMn1	LJMN10106	750.3	6.7	70.5	11.9	12.6	9.3	16.2	30.0	1814.2	12.0	14735.3	9.7	13470.8	10.4	1069.7	11.6	
JSC1	LJSC10304	1343.4	8.8	15.0	5.1	30.1	9.0	106.1	40.0	904.6	7.7	60.5	19.6	19.1	24.4	229.6	8.5	
Siderite	LSIDE0101	72.2	8.1	0.6	11.7	0.4	8.1	4.1	40.4	18.6	12.3	0.5	11.3	124.5	13.2	2687.9	35.6	
NTE01	NTE010301	67.8	2.3	42.5	6.7	72.7	9.7	626.9	48.7	80.9	1.9	490.8	14.0	1982.0	8.8	3582.7	3.3	
NTE02	NTE020106	231.4	6.2	89.6	4.8	3994.6	3.6	4359.9	16.9	523.2	2.7	901.2	2.4	276.1	3.2	783.3	3.4	
NTE03	NTE030106	97.3	2.5	55.6	3.3	269.7	13.0	1308.1	8.4	2090.1	2.6	1677.0	1.1	392.5	3.0	8608.6	3.3	
NTE04	NTE040106	1528.5	1.7	155.4	3.6	151.7	2.5	5523.4	73.1	1588.0	2.7	3316.2	8.0	107.2	4.2	1369.3	5.4	
NTE05	NTE050301	1057.4	2.0	10.6	4.3	5.7	7.8	1173.3	45.5	146.6	2.1	4827.5	3.2	65.5	4.4	2133.3	2.6	
Andesine	PMIAN0106	744.4	1.7	33.8	3.3	14.6	5.2	587.4	82.4	155.8	2.6	72.3	74.6	6.3	37.1	9.2	15.5	
Diopside	PMIDN0302	65.7	7.7	4.4	7.7	4.8	35.9	1461.0	217.0	53.4	34.5	360.3	230.1	7.9	151.6	31.1	11.2	
Enstatite	PMIEN0602	0.8	21.6	2.3	9.9	0.1	8.3	361.8	21.8	1.4	17.0	169.6	21.6	3.7	25.3	12.2	13.7	
Olivine	PMIFA0306	0.8	29.8	7.5	19.1	0.1	15.6	255.1	54.0	0.9	32.3	1512.9	20.0	682.5	90.4	616.4	20.9	
Ferrosilite	PMIFS0505	30.4	15.4	3.7	8.9	2.4	21.6	785.5	55.9	15.9	15.0	190.1	59.7	11.0	23.8	33.7	2.4	
Orthoclase	PMIOR0507	2.9	20.6	7.2	12.6	9054.6	2.6	205.0	33.7	30.7	7.4	48.1	45.8	3.3	14.0	4.5	15.1	
Shergottite	SHERG02	608.0	3.1	6.4	13.0	0.2	11.8	5.3	6.4	1189.7	5.1	370.9	1.6	11.2	21.3	6.8	8.7	
Serpentine	TSERP0102	0.2	30.4	0.1	23.7	0.2	137.5	980.9	17.4	0.3	33.6	1427.1	67.4	14.0	42.1	28.7	11.2	3.3
		P2O5 (%)	Cl (%)	F (%)														
Apatite	TAPAG0205	41.61	2.98	1.82														0.016
		SO3 (%)																
S-rich basalt	TSRICH0404	32.17																

Table 5: LA-ICP-MS/MS compositions for minor elements (in ppm except when % is mentioned) in all the LIBS SCCT targets (except for the apatite, compositions come from EMPA, and TSRICH target that is theoretical)

6.6. Comparison between Flight targets and Calibration Replicates

The set of calibration replicates (CR) discussed here is the one that was analysed with the FM/EQM setup in LANL, during the calibration campaign of SuperCam [3, 2]. These replicates were only quantified using EMPA. This set of CR and the flight targets are homogeneous and qualitatively they present similar compositions [80]. The flight targets can be used to validate the quantification models (developed using the CR calibration targets acquired in LANL) [15, 16].

Quantitative results from EMPA for these two sets of replicates are presented in Figure 17. The average content for each element is shown for both CR and FM replicates, along with their RSDs as error bars. The compositions deduced from EMPA on the CR and the FM replicates are in excellent agreement. A few differences are only observed for Si, Fe and Ca, but the

RSDs always overlap between the two replicates. The main difference is for the SiO_2 in the Chert sample, with relatively low RSDs that overlap only partially. However, the shift observed in SiO_2 content is lower than the RMSE observed on ChemCam (which is around 11 wt % for this SiO_2 content - [30]). Therefore, there are no differences in quantitative values between the two sets of replicates (LANL calibration and flight) that could impact the accuracy of the modeling.

6.7. Summary

The distribution of the major and minor element concentrations (Figure 18) covers a wide range of contents, and often larger than those observed on Mars with ChemCam up to sol 2500. The iron content in the SCCT is not as elevated as seen on Mars, but the values higher than 50 wt % at Gale crater correspond either to iron meteorites [131] or to iron oxide-rich diagenetic features [132, 133]. Some gaps in the range can still be observed, for example the SiO_2 content, with no target between 70 wt% and 95 wt%. Such high SiO_2 is not uncommon in nature, but will be covered by the wide terrestrial database [30]. Ca, K and Mn each have a single high value well above the other standards, and the terrestrial database will fill the gaps. These calibration targets cover a wide range, from a mafic to felsic silicate composition, to a carbonate or a phosphate-type of sample. Extreme compositions such as pure Fe or Mn oxides will be covered by the terrestrial database, as well as phyllosilicates or pure sulfates samples.

Minor and trace elements from the SCCT also show a wide range of distributions (more details can also be found in supplementary material, Figure S2). Compared to the terrestrial database, Li, Rb and Cu go beyond its range

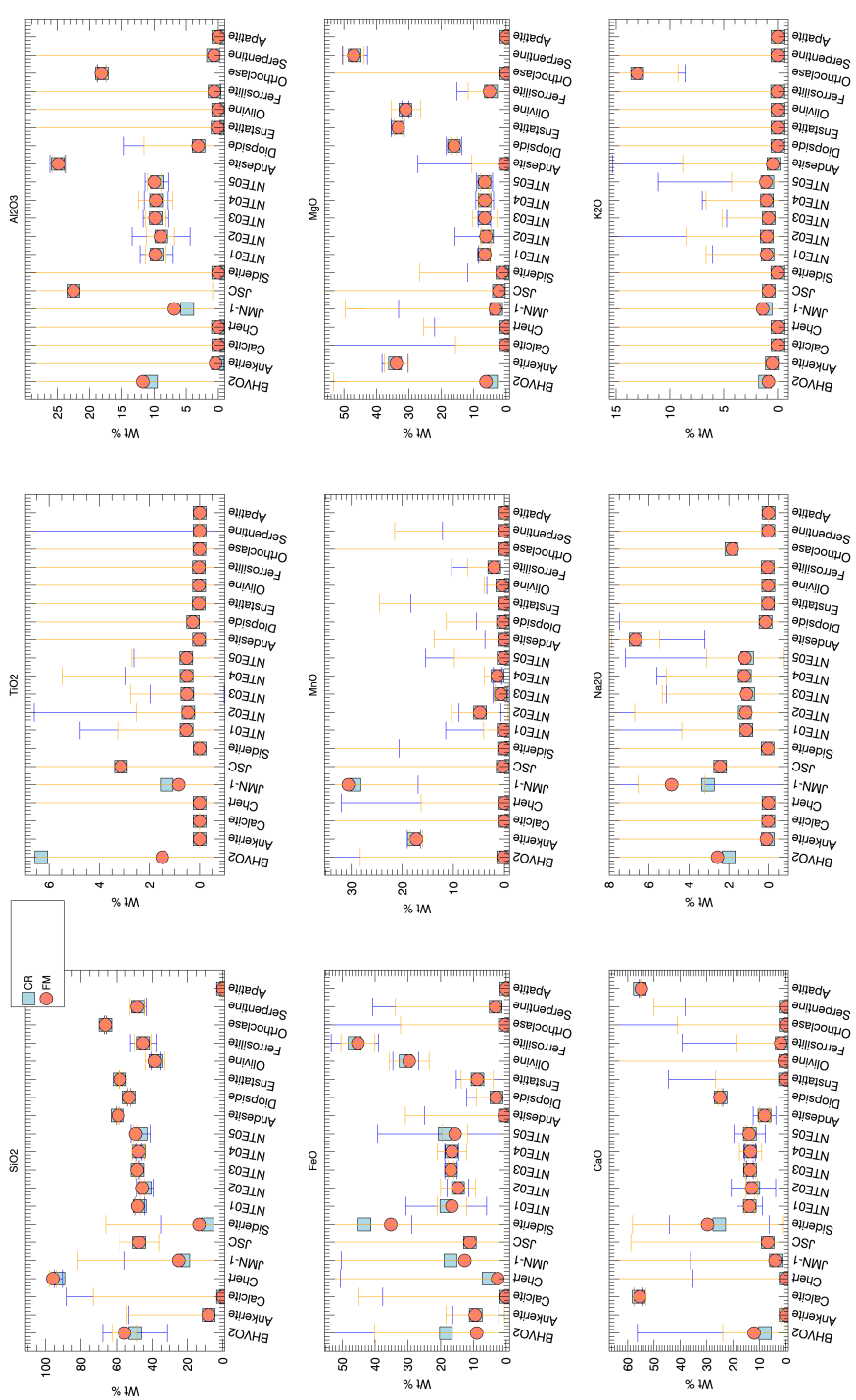

Figure 17: Average values from EPMA technique for the FM (orange) and CU (blue) replicates of the SCCTs. Error bars represent the RSDs obtained from EMPA. The RMSE obtained from ChemCam LIBS quantitative model can be found in [30].

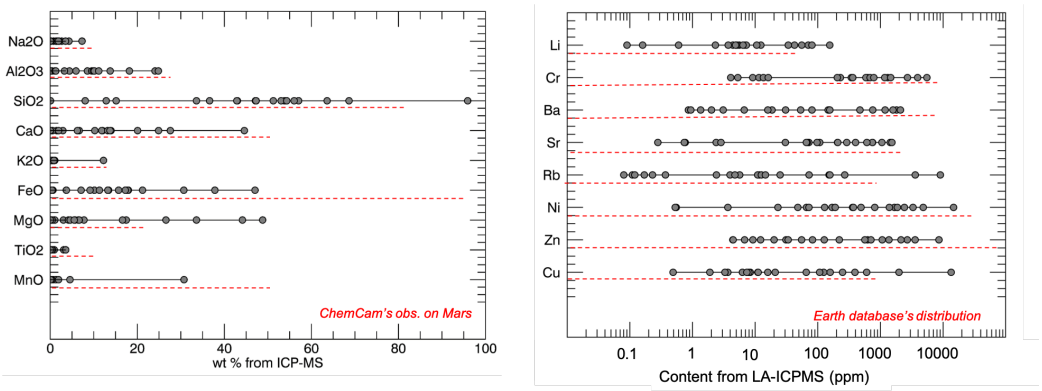

Figure 18: Quantitative compositional range of the SCCTs onboard Perseverance, for major and minor elements. The TSRICH target is not included here, as its composition is theoritical only. Dashed red line represents the range observed at Gale crater from ChemCam for the major elements (left), and the distribution of minor elements from SuperCam's Earth database on the right.

and therefore will be of great help if uncommonly high values are observed on Mars. Compared to ChemCam's observations at Gale crater for Ba, Rb, Sr and Li (minor elements that are quantified), the SCCT are covering their distribution well (Figure S2 for details). Moreover, these calibration targets are covering a sufficient range in terms of minor element to build calibration curves. This is not discussed in this study but can be found in supplementary material as well, part 5, Figure S3. Finally, these on-board calibration targets are nearly identical in terms of composition to the replicate calibration targets. They are of great importance to verify the quantitative models performed on Earth.

7. Use of the SCCT on Mars

Concerning the LIBS technique, calibration activities must fit within the overall operational scenario. One of the restrictions encountered for the operational activities is sequence duration, which needs to be kept relatively short in order to accommodate all of the high-priority science and engineering activities on the rover. In order to avoid any activity longer than 30 minutes, we have developed four different activities. Each activity will perform one point analysis on 5 to 8 different SCCTs. Each point analysis uses only 10 shots, even though usually 30 shots per point are performed on martian targets. This is because of the proximity of the calibration targets to an optical keep-out zone with the instrument [2, 9]. Mast movement is more efficient when raster sequences proceed from bottom to top, and also from right to left. With these constraints, each calibration activity has been strategically planned in order to sample a wide variety of compositions each time. Each activity consists of 1 RMI observation and 1 point of 10 shots on each of the targets included in each series, as described below.

Series 1 comprises 8 targets: Shergottite (ChemCam replicate), NTE05, Siderite, Ankerite, serpentine, enstatite, andesine and the TSRICH. As the choice of parameters on Mars will be done using only the brightest and darkest targets in terms of LIBS spectral signature (TSRICH for the brightest, Chert for the darkest), this combination will allow a check for saturation of the spectra, as the second most bright (andesine) as well as the second lowest one (shergottite) are included. This combination also allows a wide range of compositions, from mafic igneous minerals and overall basaltic composition more or less altered, to the andesine plagioclase, with carbonates and the

S-rich target.

Series 2 contains 7 targets: NTE04, NTE03, JSC-1, BHVO-2, olivine, diopside, and orthoclase. This series mainly contains mafic compositions (NTE04, NTE03, JSC-1, BHVO-2, olivine, diopside), including olivine and Ca-rich pyroxene diopside, but also includes the K feldspar, orthoclase.

Series 3 also contains 7 targets: NTE02, NTE01, JMn-1, Apatite, Ferrosilite, Calcite and Chert. This series has probably the widest range in terms of rock type, with a phosphate, a carbonate and diverse silicates such as the Chert (Si-rich) and the ferrosilite (Fe-rich orthopyroxene).

These three series constitute recurrent activities, with the aim of sampling all of the calibration targets every two months at the beginning of the mission. These data will be of prime importance in order to validate different aspects, like the Earth-Mars differences and the quantification models, which are developed using data acquired from laboratory measurements. Also, the recurrence of the activity gives a good opportunity to evaluate the dust deposition on these targets with time. Since landing, these series have been run two times and data are being analysed in details. The Titanium target is not part of these series, but represents a dedicated activity for the wavelength correction. This will be a recurrent activity that will be run monthly, and more often at the beginning of the mission.

For the Raman technique, two activities were built using the dedicated-Raman targets - the diamond and the ertalyte [9]. One activity focuses on the Raman "health check", looking at the diamond, whereas the other one is dedicated to the ertalyte observation in order to understand and better

interpret the detection of organics on Mars, but also to check the ageing of such a component under Mars UV radiations. More details about the science objective of these Raman targets can be found in [9]. The diamond observation will be performed every month, whereas the ertalyte's observation will be done every three months or less, depending on science requests. Through sol 135 of the mission, the diamond and the ertalyte targets were analysed twice.

Two series are dedicated to the Raman fingerprints of the geological targets. As seen in part 5.3, not all the targets have a detectable signal using Raman spectroscopy. Therefore, one series contains the apatite, calcite, TSRICH and the white paint, which are the geological targets showing the best Raman signal. The second series contains targets that have shown some signal from lab measurements, but to a smaller extent: the enstatite and olivine. The first series will be obtained every year, whereas the second series' cadence will depend on the signal obtained.

For the VISIR technique, the SCCT White target is to be used frequently for calibration of radiance spectra to relative reflectance and to track instrument performance and monitor its behaviour with the always evolving environmental conditions. The Black target assists with confirming instrument fields-of-view, whereas the white paint on the calibration target housing (target 34) is used to assist with wavelength calibration.

A selection of the SCCT targets shown in Figure 2 will be monitored throughout the mission to determine instrument stability and for comparison to observations of martian materials. The meteorite (target 36) can be viewed for comparison to mafic-rich materials, although no laboratory VISIR spectra

exist for this target. Care is taken to avoid the darkened LIBS laser spots on the LIBS targets.

Some of the SCCT have been analysed on Mars with the VISIR techniques (see part 5.2), at several times of day, in order to have different illumination and instrument temperature conditions.

8. Conclusions

On-board the *Perseverance* rover, the SuperCam instrument is being used as a remote-sensing facility to analyze the surface at Jezero crater using a suite of five coaligned techniques: the LIBS technique to determine the elementary composition of the targets, Raman and VISIR spectroscopy for the mineralogy and structural information, a microphone to give access to some physical parameters of the sampled rocks along with atmospheric science, and a color remote micro imager to give the context of the analyses. Supercam requires constant monitoring of the signal acquired from each technique, and this is why a set of 36 calibration targets have been developed. A dedicated set of 22 geological samples mimic the martian composition previously observed in Gale crater but also at Jezero from orbit. These targets were derived from igneous minerals, standards, natural rocks, basaltic glasses doped with minor elements and synthesised targets. A Titanium plate, a former ChemCam shergottite target and a martian meteorite thin section are also on-board as calibration support. Thus, all of the target compositions cover a wide range of major (Si, Ti, Al, Fe, Mg, Ca, Na and K) and minor elements' (Ba, Sr, Li, Zn, Mn, Ni, Cr, Cu, Rb) contents. These targets can be specifically dedicated to LIBS analysis or/and to non-destructive anal-

ysis for mineralogical studies. Replicates as well as the flight unit targets have been heavily analysed by various analytical techniques (LA-ICP-MS, EMPA, XRF, LIBS, Raman, VISIR) to check their compositional homogeneity. These analyses demonstrate that these geological calibration targets display a very homogeneous composition between the replicates and within each specimen, even for the trace elements. This allows the use of the flight unit targets for the establishment of future *in situ* calibration curves, and for validation of quantitative models. Considering that the thousands of analyses performed by ChemCam since 2012 allowed multiple discoveries and insight on Mars geological history, SuperCam will be able to provide essential clues about Jezero's geological settings in order to better choose the samples to drill and for eventual return to Earth on Mars Sample Return.

9. Acknowledgements

The authors would like to acknowledge Jéremy Guignard for his advice concerning the sample preparation for the EMPA analyses, as well as the Centre Castaing in Toulouse and the IsTep facility (UMR 7193) and ALIPP6 at Sorbonne University in Paris for their help, support and reactivity for the quantitative characterization of the samples. Authors would also like to acknowledge the SAP facility in Aude, France, for their help and professionalism concerning the machining of most of the targets, as well as Geoffroy Chevallier for the sintering of most targets in Toulouse, Florian Mercier (MATEIS, Lyon) for the SPS and Guillaume Servin (SCERAM, Lyon) for the machining done in Lyon. Also, the authors would like to thank the "Ecole des Mines", for the natural diopside that comes from their collection.

Authors would like to acknowledge Adrian Brown for his very useful inputs concerning orbital observations at Jezero crater. Authors would also like to thank all the engineering and technical team of SuperCam. The SuperCam project is supported in the US by NASA's Mars Exploration Program, and in France by CNES. Last, authors would also like to acknowledge the support of the International Space Science Institute (ISSI).

References

[1] K. Farley, K. Williford, K. Stack, R. Bhartia, A. Chen, M. de la Torre, K. Hand, Y. Goreva, C. Herd, R. Hueso, Y. Liu, J. Maki, G. Martinez, R. Moeller, A. Nelessen, C. Newman, D. Nunes, A. Ponce, N. Spanovich, P. Willis, L. Beegle, J. Bell, A. Brown, S. Hamran, J. Hurowitz, S. Maurice, D. Paige, J. Rodriguez-Manfredi, M. Schulte, R. Wiens, Mars 2020 mission overview, Space Science Reviews 216 (2020). doi:10.1007/s11214-020-00762-y, publisher Copyright: © 2020, Springer Nature B.V.

[2] S. Maurice, R. C. Wiens, P. Bernardi, P. Caïs, S. Robinson, T. Nelson, O. Gasnault, J. M. Reess, M. Deleuze, F. Rull, J. A. Manrique, S. Abbaki, R. B. Anderson, Y. André, S. M. Angel, G. Arana, T. Battault, P. Beck, K. Benzerara, S. Bernard, J. P. Berthias, O. Beyssac, M. Bonafous, B. Bousquet, M. Boutillier, A. Cadu, K. Castro, F. Chapron, B. Chide, K. Clark, E. Clavé, S. Clegg, E. Cloutis, C. Collin, E. C. Cordoba, A. Cousin, J. C. Dameury, W. D'Anna, Y. Daydou, A. Debus, L. Deflores, E. Dehouck, D. Delapp, G. De Los Santos, C. Donny, A. Doressoundiram, G. Dromart, B. Dubois,

A. Dufour, M. Dupieux, M. Egan, J. Ervin, C. Fabre, A. Fau, W. Fischer, O. Forni, T. Fouchet, J. Frydenvang, S. Gauffre, M. Gauthier, V. Gharakanian, O. Gilard, I. Gontijo, R. Gonzalez, D. Granena, J. Grotzinger, R. Hassen-Khodja, M. Heim, Y. Hello, G. Hervet, O. Humeau, X. Jacob, S. Jacquinod, J. R. Johnson, D. Kouach, G. Lacombe, N. Lanza, L. Lapauw, J. Laserna, J. Lasue, L. Le Deit, S. Le Mouélic, E. Le Comte, Q. M. Lee, C. Legett, R. Leveille, E. Lewin, C. Leyrat, G. Lopez-Reyes, R. Lorenz, B. Lucero, J. M. Madariaga, S. Madsen, M. Madsen, N. Mangold, F. Manni, J. F. Mariscal, J. Martinez-Frias, K. Mathieu, R. Mathon, K. P. McCabe, T. McConnochie, S. M. McLennan, J. Mekki, N. Melikechi, P. Y. Meslin, Y. Micheau, Y. Michel, J. M. Michel, D. Mimoun, A. Misra, G. Montagnac, C. Montaron, F. Montmessin, J. Moros, V. Mousset, Y. Morizet, N. Murdoch, R. T. Newell, H. Newsom, N. Nguyen Tuong, A. M. Ollila, G. Orttner, L. Oudda, L. Pares, J. Parisot, Y. Parot, R. Pérez, D. Pheav, L. Picot, P. Pilleri, C. Pilorget, P. Pinet, G. Pont, F. Poulet, C. Quantin-Nataf, B. Quertier, D. Rambaud, W. Rapin, P. Romano, L. Roucayrol, C. Royer, M. Ruellan, B. F. Sandoval, V. Sautter, M. J. Schoppers, S. Schröder, H. C. Seran, S. K. Sharma, P. Sobron, M. Sodki, A. Sournac, V. Sridhar, D. Standarovsky, S. Storms, N. Striebig, M. Tatat, M. Toplis, I. Torre-Fdez, N. Toulemont, C. Velasco, M. Veneranda, D. Venhaus, C. Virmontois, M. Viso, P. Willis, K. W. Wong, The SuperCam Instrument Suite on the Mars 2020 Rover: Science Objectives and Mast-Unit Description, 217 (2021) 47. doi:10.1007/s11214-021-00807-w.

[3] R. C. Wiens, S. Maurice, S. H. Robinson, A. E. Nelson, P. Cais, P. Bernardi, R. T. Newell, S. Clegg, S. K. Sharma, S. Storms, J. Deming, D. Beckman, A. M. Ollila, O. Gasnault, R. B. Anderson, Y. André, S. Michael Angel, G. Arana, E. Auden, P. Beck, J. Becker, K. Benzerara, S. Bernard, O. Beyssac, L. Borges, B. Bousquet, K. Boyd, M. Caffrey, J. Carlson, K. Castro, J. Celis, B. Chide, K. Clark, E. Cloutis, E. C. Cordoba, A. Cousin, M. Dale, L. Deflores, D. Delapp, M. Deleuze, M. Dirmyer, C. Donny, G. Dromart, M. George Duran, M. Egan, J. Ervin, C. Fabre, A. Fau, W. Fischer, O. Forni, T. Fouchet, R. Fresquez, J. Frydenvang, D. Gasway, I. Gontijo, J. Grotzinger, X. Jacob, S. Jacquinod, J. R. Johnson, R. A. Klisiewicz, J. Lake, N. Lanza, J. Laserna, J. Lasue, S. Le Mouélic, C. Legett, R. Leveille, E. Lewin, G. Lopez-Reyes, R. Lorenz, E. Lorigny, S. P. Love, B. Lucero, J. M. Madariaga, M. Madsen, S. Madsen, N. Mangold, J. A. Manrique, J. P. Martinez, J. Martinez-Frias, K. P. McCabe, T. H. McConnochie, J. M. McGlown, S. M. McLennan, N. Melikechi, P.-Y. Meslin, J. M. Michel, D. Mimoun, A. Misra, G. Montagnac, F. Montmessin, V. Mousset, N. Murdoch, H. Newsom, L. A. Ott, Z. R. Ousnamer, L. Pares, Y. Parot, R. Pawluczyk, C. Glen Peterson, P. Pilleri, P. Pinet, G. Pont, F. Poulet, C. Provost, B. Quertier, H. Quinn, W. Rapin, J.-M. Reess, A. H. Regan, A. L. Reyes-Newell, P. J. Romano, C. Royer, F. Rull, B. Sandoval, J. H. Sarrao, V. Sautter, M. J. Schoppers, S. Schröder, D. Seitz, T. Shepherd, P. Sobron, B. Dubois, V. Sridhar, M. J. Toplis, I. Torre-Fdez, I. A. Trettel, M. Underwood, A. Valdez, J. Valdez, D. Venhaus, P. Willis, The SuperCam Instrument Suite on the NASA

Mars 2020 Rover: Body Unit and Combined System Tests, 217 (2021) 4. doi:10.1007/s11214-020-00777-5.

[4] S. Maurice, R. C. Wiens, M. Saccoccio, B. Barraclough, O. Gasnault, O. Forni, N. Mangold, D. Baratoux, S. Bender, G. Berger, J. Bernardin, M. Berthé, N. Bridges, D. Blaney, M. Bouyé, P. Caïs, B. Clark, S. Clegg, A. Cousin, D. Cremers, A. Cros, L. DeFlores, C. Derycke, B. Dingler, G. Dromart, B. Dubois, M. Dupieux, E. Durand, L. d'Uston, C. Fabre, B. Faure, A. Gaboriaud, T. Gharsa, K. Herkenhoff, E. Kan, L. Kirkland, D. Kouach, J. L. Lacour, Y. Langevin, J. Lasue, S. Le Mouélic, M. Lescure, E. Lewin, D. Limonadi, G. Manhès, P. Mauchien, C. McKay, P. Y. Meslin, Y. Michel, E. Miller, H. E. Newsom, G. Orttner, A. Paillet, L. Parès, Y. Parot, R. Pérez, P. Pinet, F. Poitrasson, B. Quertier, B. Sallé, C. Sotin, V. Sautter, H. Séran, J. J. Simmonds, J. B. Sirven, R. Stiglich, N. Striebig, J. J. Thocaven, M. J. Toplis, D. Vaniman, The ChemCam Instrument Suite on the Mars Science Laboratory (MSL) Rover: Science Objectives and Mast Unit Description, 170 (2012) 95–166. doi:10.1007/s11214-012-9912-2.

[5] R. C. Wiens, S. Maurice, B. Barraclough, M. Saccoccio, W. C. Barkley, J. F. Bell, S. Bender, J. Bernardin, D. Blaney, J. Blank, M. Bouyé, N. Bridges, N. Bultman, P. Caïs, R. C. Clanton, B. Clark, S. Clegg, A. Cousin, D. Cremers, A. Cros, L. DeFlores, D. Delapp, R. Dingler, C. D'Uston, M. Darby Dyar, T. Elliott, D. Enemark, C. Fabre, M. Flores, O. Forni, O. Gasnault, T. Hale, C. Hays, K. Herkenhoff, E. Kan, L. Kirkland, D. Kouach, D. Landis, Y. Langevin,

N. Lanza, F. LaRocca, J. Lasue, J. Latino, D. Limonadi, C. Lindensmith, C. Little, N. Mangold, G. Manhes, P. Mauchien, C. McKay, E. Miller, J. Mooney, R. V. Morris, L. Morrison, T. Nelson, H. Newsom, A. Ollila, M. Ott, L. Pares, R. Perez, F. Poitrasson, C. Provost, J. W. Reiter, T. Roberts, F. Romero, V. Sautter, S. Salazar, J. J. Simmonds, R. Stiglich, S. Storms, N. Striebig, J.-J. Thocaven, T. Trujillo, M. Ulibarri, D. Vaniman, N. Warner, R. Waterbury, R. Whitaker, J. Witt, B. Wong-Swanson, The ChemCam Instrument Suite on the Mars Science Laboratory (MSL) Rover: Body Unit and Combined System Tests, 170 (2012) 167–227. doi:10.1007/s11214-012-9902-4.

[6] B. Chide, S. Maurice, A. Cousin, B. Bousquet, D. Mimoun, O. Beyssac, P.-Y. Meslin, R. C. Wiens, Recording laser-induced sparks on mars with the supercam microphone, Spectrochimica Acta Part B: Atomic Spectroscopy 174 (2020) 106000. doi:https://doi.org/10.1016/j.sab.2020.106000.

[7] B. Chide, N. Murdoch, Y. Bury, S. Maurice, X. Jacob, J. P. Merrison, J. J. Iversen, P.-Y. Meslin, M. Bassas-PortÃºs, A. Cadu, A. Sournac, B. Dubois, R. D. Lorenz, D. Mimoun, R. C. Wiens, Experimental wind characterization with the supercam microphone under a simulated martian atmosphere, Icarus (2020) 114060. doi:https://doi.org/10.1016/j.icarus.2020.114060.

[8] Fouchet T.., VISIR atmosphere, ?? ? (2020) ? doi:?

[9] J. A. Manrique, G. Lopez-Reyes, A. Cousin, F. Rull, S. Maurice, R. C. Wiens, M. B. Madsen, J. M. Madariaga, O. Gasnault, J. Aramendia,

G. Arana, P. Beck, S. Bernard, P. Bernardi, M. H. Bernt, A. Berrocal, O. Beyssac, P. Caïs, C. Castro, K. Castro, S. M. Clegg, E. Cloutis, G. Dromart, C. Drouet, B. Dubois, D. Escribano, C. Fabre, A. Fernandez, O. Forni, V. Garcia-Baonza, I. Gontijo, J. Johnson, J. Laserna, J. Lasue, S. Madsen, E. Mateo-Marti, J. Medina, P. Y. Meslin, G. Montagnac, A. Moral, J. Moros, A. M. Ollila, C. Ortega, O. Prieto-Ballesteros, J. M. Reess, S. Robinson, J. Rodriguez, J. Saiz, J. A. Sanz-Arranz, I. Sard, V. Sautter, P. Sobron, M. Toplis, M. Veneranda, SuperCam Calibration Targets: Design and Development, 216 (2020) 138. doi:10.1007/s11214-020-00764-w.

[10] G. Montagnac, G. Dromart, P. Beck, F. Mercier, B. Reynard, A. Cousin, S. Maurice, R. Wiens, Spark plasma sintering preparation of reference targets for field spectroscopy on mars, Journal of Raman Spectroscopy 49 (2018) 1419–1425. doi:10.1002/jrs.5406.

[11] G. H. Howarth, A. Udry, Trace elements in olivine and the petrogenesis of the intermediate, olivine-phyric shergottite nwa 10170, Meteoritics & Planetary Science 52 (2017) 391–409. doi:10.1111/maps.12799.

[12] Bouvier A., The Meteoritical Bulletin, No. 104, Meteorics and Planetary Science 1 (2017) ? doi:10.1111/maps.12930.

[13] C. Royer, F. Poulet, J.-M. Reess, C. Pilorget, V. Hamm, T. Fouchet, S. Maurice, O. Forni, P. Bernardi, F. Montmessin, L. Lapauw, J. Parisot, M. Bonafous, O. Gasnault, R. C. Wiens, Pre-launch radiometric calibration of the infrared spectrometer onboard supercam

for the mars2020 rover, Review of Scientific Instruments 91 (2020) 063105. doi:10.1063/1.5145390.

[14] G. Lopez-Reyes, C. Pilorget, A. G. Moral, J. A. Manrique, A. Sanz, A. Berrocal, M. Veneranda, F. Rull, J. Medina, V. Hamm, J.-P. Bibring, J. A. Rodriguez, C. Perez Canora, E. Mateo-Marti, O. Prieto-Ballesteros, E. Lalla, J. L. Vago, Raman laser spectrometer (rls) calibration target design to allow onboard combined science between the rls and micromega instruments on the exomars rover, Journal of Raman Spectroscopy 51 (2020) 1718–1730. doi:10.1002/jrs.5832.

[15] R. B. Anderson, O. Forni, S. M. Clegg, A. Cousin, J. Frydenvang, P. Pilleri, C. Legett, R. C. Wiens, S. Maurice, G. Arana, O. Beyssac, B. Bousquet, B. Chide, E. Clave, D. Delapp, A. Essunfeld, T. Fouchet, C. Garcia-Florentino, O. Gasnault, E. Gibbons, J. Laserna, J. Lasue, J. A. Manrique, J. M. Madariaga, R. Newell, A. Ollila, S. Sharma, J. Simon, P. Sobron, SuperCam Laser Induced Breakdown Spectroscopy (LIBS) Data Processing, Calibration, and First Results, in: Lunar and Planetary Science Conference, Lunar and Planetary Science Conference, 2021, p. 1606.

[16] O. Forni, A. Anderson, R. B. Cousin, , S. M. Clegg, J. Frydenvang, P. Pilleri, C. Legett, R. C. Wiens, S. Maurice, G. Arana, O. Beyssac, B. Bousquet, B. Chide, E. Clave, D. Delapp, A. Essunfeld, T. Fouchet, C. Garcia-Florentino, O. Gasnault, E. Gibbons, J. Laserna, J. Lasue, J. A. Manrique, J. M. Madariaga, R. Newell, A. Ollila, S. Sharma, J. Simon, P. Sobron, Supercam Laser Induced Breakdown Spectroscopy

Calibration, Data Processing, and First Results,, in: EGU General Assembly 2021, 2021, p. 1081.

[17] N. L. Lanza, W. W. Fischer, R. C. Wiens, J. Grotzinger, A. M. Ollila, A. Cousin, R. B. Anderson, B. C. Clark, R. Gellert, N. Mangold, S. Maurice, S. Le Mouelic, M. Nachon, M. Schmidt, J. Berger, S. M. Clegg, O. Forni, C. Hardgrove, N. Melikechi, H. E. Newsom, V. Sautter, High manganese concentrations in rocks at gale crater, mars, Geophysical Research Letters 41 (2014) 5755–5763. doi:10.1002/2014GL060329.

[18] N. L. Lanza, R. C. Wiens, R. E. Arvidson, B. C. Clark, W. W. Fischer, R. Gellert, J. P. Grotzinger, J. A. Hurowitz, S. M. McLennan, R. V. Morris, M. S. Rice, J. F. Bell III, J. A. Berger, D. L. Blaney, N. T. Bridges, F. Calef III, J. L. Campbell, S. M. Clegg, A. Cousin, K. S. Edgett, C. Fabre, M. R. Fisk, O. Forni, J. Frydenvang, K. R. Hardy, C. Hardgrove, J. R. Johnson, J. Lasue, S. Le Mouelic, M. C. Malin, N. Mangold, J. MartÃ¬n-Torres, S. Maurice, M. J. McBride, D. W. Ming, H. E. Newsom, A. M. Ollila, V. Sautter, S. Schroeder, L. M. Thompson, A. H. Treiman, S. VanBommel, D. T. Vaniman, M.-P. Zorzano, Oxidation of manganese in an ancient aquifer, kimberley formation, gale crater, mars, Geophysical Research Letters 43 (2016) 7398–7407. doi:10.1002/2016GL069109.

[19] R. E. Arvidson, S. W. Squyres, J. F. Bell, J. G. Catalano, B. C. Clark, L. S. Crumpler, P. A. de Souza, A. G. Fairén, W. H. Farrand, V. K. Fox, R. Gellert, A. Ghosh, M. P. Golombek, J. P. Grotzinger, E. A. Guinness, K. E. Herkenhoff, B. L. Jolliff, A. H. Knoll, R. Li, S. M.

McLennan, D. W. Ming, D. W. Mittlefehldt, J. M. Moore, R. V. Morris, S. L. Murchie, T. J. Parker, G. Paulsen, J. W. Rice, S. W. Ruff, M. D. Smith, M. J. Wolff, Ancient aqueous environments at endeavour crater, mars, Science 343 (2014). doi:10.1126/science.1248097.

[20] B. C. Clark, R. V. Morris, K. E. Herkenhoff, W. H. Farrand, R. Gellert, B. L. Jolliff, R. E. Arvidson, S. W. Squyres, D. W. Mittlefehldt, D. W. Ming, A. S. Yen, Esperance: Multiple episodes of aqueous alteration involving fracture fills and coatings at Matijevic Hill, Mars, American Mineralogist 101 (2016) 1515–1526. doi:10.2138/am-2016-5575.

[21] S. W. Squyres, R. E. Arvidson, S. Ruff, R. Gellert, R. V. Morris, D. W. Ming, L. Crumpler, J. D. Farmer, D. J. D. Marais, A. Yen, S. M. McLennan, W. Calvin, J. F. Bell, B. C. Clark, A. Wang, T. J. McCoy, M. E. Schmidt, P. A. de Souza, Detection of silica-rich deposits on mars, Science 320 (2008) 1063–1067. doi:10.1126/science.1155429.

[22] S. W. Ruff, J. D. Farmer, W. M. Calvin, K. E. Herkenhoff, J. R. Johnson, R. V. Morris, M. S. Rice, R. E. Arvidson, J. F. Bell III, P. R. Christensen, S. W. Squyres, Characteristics, distribution, origin, and significance of opaline silica observed by the spirit rover in gusev crater, mars, Journal of Geophysical Research: Planets 116 (2011). doi:https://doi.org/10.1029/2010JE003767.

[23] S. W. Ruff, K. A. Campbell, M. J. Van Kranendonk, M. S. Rice, J. D. Farmer, The case for ancient hot springs in gusev crater, mars, Astrobiology 20 (2020) 475–499. doi:10.1089/ast.2019.2044, pMID: 31621375.

[24] A. Yen, D. Ming, D. Vaniman, R. Gellert, D. Blake, R. Morris, S. Morrison, T. Bristow, S. Chipera, K. Edgett, A. Treiman, B. Clark, R. Downs, J. Farmer, J. Grotzinger, E. Rampe, M. Schmidt, B. Sutter, L. Thompson, Multiple stages of aqueous alteration along fractures in mudstone and sandstone strata in gale crater, mars, Earth and Planetary Science Letters 471 (2017) 186 – 198. doi:https://doi.org/10.1016/j.epsl.2017.04.033.

[25] J. Frydenvang, P. J. Gasda, J. A. Hurowitz, J. P. Grotzinger, R. C. Wiens, H. E. Newsom, K. S. Edgett, J. Watkins, J. C. Bridges, S. Maurice, M. R. Fisk, J. R. Johnson, W. Rapin, N. T. Stein, S. M. Clegg, S. P. Schwenzer, C. C. Bedford, P. Edwards, N. Mangold, A. Cousin, R. B. Anderson, V. Payre, D. Vaniman, D. F. Blake, N. L. Lanza, S. Gupta, J. Van Beek, V. Sautter, P.-Y. Meslin, M. Rice, R. Milliken, R. Gellert, L. Thompson, B. C. Clark, D. Y. Sumner, A. A. Fraeman, K. M. Kinch, M. B. Madsen, I. G. Mitrofanov, I. Jun, F. Calef, A. R. Vasavada, Diagenetic silica enrichment and late-stage groundwater activity in gale crater, mars, Geophysical Research Letters 44 (2017) 4716–4724. doi:https://doi.org/10.1002/2017GL073323.

[26] W. Rapin, B. Chauvire, T. S. J. Gabriel, A. C. McAdam, B. L. Ehlmann, C. Hardgrove, P.-Y. Meslin, B. Rondeau, E. Dehouck, H. B. Franz, N. Mangold, S. J. Chipera, R. C. Wiens, J. Frydenvang, S. Schroeder, In situ analysis of opal in gale crater, mars, Journal of Geophysical Research: Planets 123 (2018) 1955–1972. doi:https://doi.org/10.1029/2017JE005483.

[27] C. Fabre, S. Maurice, A. Cousin, R. C. Wiens, O. Forni, V. Sautter, D. Guillaume, Onboard calibration igneous targets for the Mars Science Laboratory Curiosity rover and the Chemistry Camera laser induced breakdown spectroscopy instrument, Spectrochimica Acta 66 (2011) 280–289. doi:10.1016/j.sab.2011.03.012.

[28] D. Vaniman, M. D. Dyar, R. Wiens, A. Ollila, N. Lanza, J. Lasue, J. M. Rhodes, S. Clegg, H. Newsom, Ceramic ChemCam Calibration Targets on Mars Science Laboratory, 170 (2012) 229–255. doi:10.1007/s11214-012-9886-0.

[29] D. Vaniman, M. D. Dyar, R. Wiens, A. Ollila, N. Lanza, J. Lasue, J. M. Rhodes, S. Clegg, H. Newsom, Erratum: Erratum to: Ceramic ChemCam Calibration Targets on Mars Science Laboratory, 170 (2012) 257–258. doi:10.1007/s11214-012-9929-6.

[30] S. M. Clegg, R. C. Wiens, R. Anderson, O. Forni, J. Frydenvang, J. Lasue, A. Cousin, V. Payré, T. Boucher, M. D. Dyar, S. M. McLennan, R. V. Morris, T. G. Graff, S. A. Mertzman, B. L. Ehlmann, I. Belgacem, H. Newsom, B. C. Clark, N. Melikechi, A. Mezzacappa, R. E. McInroy, R. Martinez, P. Gasda, O. Gasnault, S. Maurice, Recalibration of the Mars Science Laboratory ChemCam instrument with an expanded geochemical database, Spectrochimica Acta 129 (2017) 64–85. doi:10.1016/j.sab.2016.12.003.

[31] J. Lasue, A. Cousin, P.-Y. Meslin, N. Mangold, R. C. Wiens, G. Berger, E. Dehouck, O. Forni, W. Goetz, O. Gasnault, W. Rapin, S. Schroeder, A. Ollila, J. Johnson, S. Le Mouelic, S. Maurice, R. Anderson,

D. Blaney, B. Clark, S. M. Clegg, C. d'Uston, C. Fabre, N. Lanza, M. B. Madsen, J. Martin-Torres, N. Melikechi, H. Newsom, V. Sautter, M. P. Zorzano, Martian eolian dust probed by chemcam, Geophysical Research Letters 45 (2018) 10,968–10,977. doi:10.1029/2018GL079210.

[32] N. Melikechi, A. Mezzacappa, A. Cousin, N. Lanza, J. Lasue, S. Clegg, G. Berger, R. Wiens, S. Maurice, R. Tokar, S. Bender, O. Forni, E. Breves, M. Dyar, J. Frydenvang, D. Delapp, O. Gasnault, H. Newsom, A. Ollila, E. Lewin, B. Clark, B. Ehlmann, D. Blaney, C. Fabre, Correcting for variable laser-target distances of laser-induced breakdown spectroscopy measurements with chemcam using emission lines of martian dust spectra, Spectrochimica Acta Part B: Atomic Spectroscopy 96 (2014) 51–60. doi:10.1016/j.sab.2014.04.004.

[33] A. Mezzacappa, N. Melikechi, A. Cousin, R. Wiens, J. Lasue, S. Clegg, R. Tokar, S. Bender, N. Lanza, S. Maurice, G. Berger, O. Forni, O. Gasnault, M. Dyar, T. Boucher, E. Lewin, C. Fabre, Application of distance correction to chemcam laser-induced breakdown spectroscopy measurements, Spectrochimica Acta Part B: Atomic Spectroscopy 120 (2016) 19 – 29. doi:https://doi.org/10.1016/j.sab.2016.03.009.

[34] Introduction, John Wiley Sons, Ltd, 2013, pp. 1–27. doi:10.1002/9781118567371.ch1.

[35] C. Chaleard, P. Mauchien, N. Andre, J. Uebbing, J. L. Lacour, C. Geertsen, Correction of Matrix Effects in Quantitative Elemental Analysis With Laser Ablation Optical Emission Spectrometry, Journal of Analytical Atomic Spectrometry 12 (1997).

[36] C. Fabre, A. Cousin, R. Wiens, A. Ollila, O. Gasnault, S. Maurice, V. Sautter, O. Forni, J. Lasue, R. Tokar, D. Vaniman, N. Melikechi, In situ calibration using univariate analyses based on the onboard chemcam targets: first prediction of martian rock and soil compositions, Spectrochimica Acta Part B: Atomic Spectroscopy 99 (2014) 34 – 51. doi:https://doi.org/10.1016/j.sab.2014.03.014.

[37] B. L. Ehlmann, J. F. Mustard, S. L. Murchie, F. Poulet, J. L. Bishop, A. J. Brown, W. M. Calvin, R. N. Clark, D. J. Des Marais, R. E. Milliken, L. H. Roach, T. L. Roush, G. A. Swayze, J. J. Wray, Orbital Identification of Carbonate-Bearing Rocks on Mars, Science 322 (2008) 1828. doi:10.1126/science.1164759.

[38] T. A. Goudge, J. F. Mustard, J. W. Head, C. I. Fassett, S. M. Wiseman, Assessing the mineralogy of the watershed and fan deposits of the Jezero crater paleolake system, Mars, Journal of Geophysical Research (Planets) 120 (2015) 775–808. doi:10.1002/2014JE004782.

[39] C. I. Fassett, J. W. Head III, Fluvial sedimentary deposits on mars: Ancient deltas in a crater lake in the nili fossae region, Geophysical Research Letters 32 (2005). doi:10.1029/2005GL023456.

[40] S. C. Schon, J. W. Head, C. I. Fassett, An overfilled lacustrine system and progradational delta in jezero crater, mars: Implications for noachian climate, Planetary and Space Science 67 (2012) 28 – 45. doi:https://doi.org/10.1016/j.pss.2012.02.003.

[41] K. H. Williford, K. A. Farley, K. M. Stack, A. C. Allwood, D. Beaty,

L. W. Beegle, R. Bhartia, A. J. Brown, M. de la Torre Juarez, S.-E. Hamran, M. H. Hecht, J. A. Hurowitz, J. A. Rodriguez-Manfredi, S. Maurice, S. Milkovich, R. C. Wiens, Chapter 11 - the nasa mars 2020 rover mission and the search for extraterrestrial life, in: N. A. Cabrol, E. A. Grin (Eds.), From Habitability to Life on Mars, Elsevier, 2018, pp. 275–308. doi:https://doi.org/10.1016/B978-0-12-809935-3.00010-4.

[42] N. Mangold, G. Dromart, V. Ansan, F. Salese, M. G. Kleinhans, M. MassÃ©, C. Quantin-Nataf, K. M. Stack, Fluvial regimes, morphometry, and age of jezero crater paleolake inlet valleys and their exobiological significance for the 2020 rover mission landing site, Astrobiology 20 (2020) 994–1013. doi:10.1089/ast.2019.2132, pMID: 32466668.

[43] P. Pinet, S. Chevrel, Spectral identification of geological units on the surface of Mars related to the presence of silicates from Earth-based near-infrared telescopic charge-coupled device imaging., 95 (1990) 14435–14446. doi:10.1029/JB095iB09p14435.

[44] T. A. Goudge, D. Mohrig, B. T. Cardenas, C. M. Hughes, C. I. Fassett, Stratigraphy and paleohydrology of delta channel deposits, Jezero crater, Mars, 301 (2018) 58–75. doi:10.1016/j.icarus.2017.09.034.

[45] K. M. Stack, N. R. Williams, F. Calef, V. Z. Sun, K. H. Williford, K. A. Farley, S. Eide, D. Flannery, C. Hughes, S. R. Jacob, L. C. Kah, F. Meyen, A. Molina, C. Q. Nataf, M. Rice, P. Russell, E. Scheller, C. H. Seeger, W. J. Abbey, J. B. Adler, H. Amundsen, R. B. Anderson, S. M. Angel, G. Arana, J. Atkins, M. Barrington, T. Berger, R. Borden, B. Boring, A. Brown, B. L. Carrier, P. Conrad, H. Dypvik,

S. A. Fagents, Z. E. Gallegos, B. Garczynski, K. Golder, F. Gomez, Y. Goreva, S. Gupta, S.-E. Hamran, T. Hicks, E. D. Hinterman, B. N. Horgan, J. Hurowitz, J. R. Johnson, J. Lasue, R. E. Kronyak, Y. Liu, J. M. Madariaga, N. Mangold, J. McClean, N. Miklusicak, D. Nunes, C. Rojas, K. Runyon, N. Schmitz, N. Scudder, E. Shaver, J. SooHoo, R. Spaulding, E. Stanish, L. K. Tamppari, M. M. Tice, N. Turenne, P. A. Willis, R. Aileen Yingst, Photogeologic Map of the Perseverance Rover Field Site in Jezero Crater Constructed by the Mars 2020 Science Team, 216 (2020) 127. doi:10.1007/s11214-020-00739-x.

[46] J. F. Mustard, F. Poulet, J. W. Head, N. Mangold, J.-P. Bibring, S. M. Pelkey, C. I. Fassett, Y. Langevin, G. Neukum, Mineralogy of the nili fossae region with omega/mars express data: 1. ancient impact melt in the isidis basin and implications for the transition from the noachian to hesperian, Journal of Geophysical Research: Planets 112 (2007). doi:10.1029/2006JE002834.

[47] J. F. Mustard, B. L. Ehlmann, S. L. Murchie, F. Poulet, N. Mangold, J. W. Head, J.-P. Bibring, L. H. Roach, Composition, morphology, and stratigraphy of noachian crust around the isidis basin, Journal of Geophysical Research: Planets 114 (2009). doi:10.1029/2009JE003349.

[48] N. Mangold, F. Poulet, J. F. Mustard, J.-P. Bibring, B. Gondet, Y. Langevin, V. Ansan, P. Masson, C. Fassett, J. W. Head III, H. Hoffmann, G. Neukum, Mineralogy of the nili fossae region with omega/mars express data: 2. aqueous alteration of the crust, Journal of Geophysical Research: Planets 112 (2007). doi:10.1029/2006JE002835.

[49] T. A. Goudge, R. E. Milliken, J. W. Head, J. F. Mustard, C. I. Fassett, Sedimentological evidence for a deltaic origin of the western fan deposit in jezero crater, mars and implications for future exploration, Earth and Planetary Science Letters 458 (2017) 357 – 365. doi:https://doi.org/10.1016/j.epsl.2016.10.056.

[50] A. J. Brown, C. E. Viviano, T. A. Goudge, Olivine-carbonate mineralogy of the jezero crater region, Journal of Geophysical Research: Planets 125 (2020) e2019JE006011. doi:https://doi.org/10.1029/2019JE006011, e2019JE006011 2019JE006011.

[51] L. Mandon, C. Quantin-Nataf, P. Thollot, N. Mangold, L. Lozac'h, G. Dromart, P. Beck, E. Dehouck, S. Breton, C. Millot, M. Volat, Refining the age, emplacement and alteration scenarios of the olivine-rich unit in the nili fossae region, mars, Icarus 336 (2020) 113436. doi:https://doi.org/10.1016/j.icarus.2019.113436.

[52] B. L. Ehlmann, J. F. Mustard, G. A. Swayze, R. N. Clark, J. L. Bishop, F. Poulet, D. J. Des Marais, L. H. Roach, R. E. Milliken, J. J. Wray, O. Barnouin-Jha, S. L. Murchie, Identification of hydrated silicate minerals on Mars using MRO-CRISM: Geologic context near Nili Fossae and implications for aqueous alteration, Journal of Geophysical Research (Planets) 114 (2009) E00D08. doi:10.1029/2009JE003339.

[53] A. J. Brown, S. J. Hook, A. M. Baldridge, J. K. Crowley, N. T. Bridges, B. J. Thomson, G. M. Marion, C. R. de Souza Filho, J. L. Bishop, Hydrothermal formation of clay-carbonate alteration assemblages in

the nili fossae region of mars, Earth and Planetary Science Letters 297 (2010) 174–182. doi:https://doi.org/10.1016/j.epsl.2010.06.018.

[54] B. H. Horgan, R. B. Anderson, G. Dromart, E. S. Amador, M. S. Rice, The mineral diversity of jezero crater: Evidence for possible lacustrine carbonates on mars, Icarus 339 (2020) 113526. doi:https://doi.org/10.1016/j.icarus.2019.113526.

[55] S. Werner, The early martian evolution. constraints from basin formation ages, Icarus 195 (2008) 45 – 60. doi:https://doi.org/10.1016/j.icarus.2007.12.008.

[56] A. Cousin, V. Sautter, V. Payré, O. Forni, N. Mangold, O. Gasnault, L. Le Deit, J. Johnson, S. Maurice, M. Salvatore, R. C. Wiens, P. Gasda, W. Rapin, Classification of igneous rocks analyzed by ChemCam at Gale crater, Mars, 288 (2017) 265–283. doi:10.1016/j.icarus.2017.01.014.

[57] V. Payre, K. L. Siebach, R. Dasgupta, A. Udry, E. B. Rampe, S. M. Morrison, Constraining ancient magmatic evolution on mars using crystal chemistry of detrital igneous minerals in the sedimentary bradbury group, gale crater, mars, Journal of Geophysical Research: Planets 125 (2020) e2020JE006467. doi:10.1029/2020JE006467, e2020JE006467 2020JE006467.

[58] C. Bedford, J. Bridges, S. Schwenzer, R. Wiens, E. Rampe, J. Frydenvang, P. Gasda, Alteration trends and geochemical source region characteristics preserved in the fluviolacustrine sedimentary record of

gale crater, mars, Geochimica et Cosmochimica Acta 246 (2019) 234–266. doi:https://doi.org/10.1016/j.gca.2018.11.031.

[59] F. Baron, A. Gaudin, J.-P. Lorand, N. Mangold, New constraints on early mars weathering conditions from an experimental approach on crust simulants, Journal of Geophysical Research: Planets 124 (2019) 1783–1801. doi:10.1029/2019JE005920.

[60] A. M. Ollila, H. E. Newsom, B. Clark, R. C. Wiens, A. Cousin, J. G. Blank, N. Mangold, V. Sautter, S. Maurice, S. M. Clegg, O. Gasnault, O. Forni, R. Tokar, E. Lewin, M. D. Dyar, J. Lasue, R. Anderson, S. M. McLennan, J. Bridges, D. Vaniman, N. Lanza, C. Fabre, N. Melikechi, G. M. Perrett, J. L. Campbell, P. L. King, B. Barraclough, D. Delapp, S. Johnstone, P.-Y. Meslin, A. Rosen-Gooding, J. Williams, Trace element geochemistry (Li, Ba, Sr, and Rb) using Curiosity's ChemCam: Early results for Gale crater from Bradbury Landing Site to Rocknest, Journal of Geophysical Research (Planets) 119 (2014) 255–285. doi:10.1002/2013JE004517.

[61] V. Payré, C. Fabre, A. Cousin, V. Sautter, R. C. Wiens, O. Forni, O. Gasnault, N. Mangold, P. Y. Meslin, J. Lasue, A. Ollila, W. Rapin, S. Maurice, M. Nachon, L. Le Deit, N. Lanza, S. Clegg, Alkali trace elements in Gale crater, Mars, with ChemCam: Calibration update and geological implications, Journal of Geophysical Research (Planets) 122 (2017) 650–679. doi:10.1002/2016JE005201.

[62] P. Y. Meslin, J. R. Johnson, O. Forni, P. Beck, A. Cousin, J. Bridges, W. Rapin, B. Cohen, H. Newsom, V. Sautter, E. Lewin, M. Na-

chon, R. C. Wiens, V. Payré, O. Gasnault, S. Maurice, A. G. Fairén, S. Schröder, N. Mangold, N. Thomas, Egg Rock Encounter: Analysis of an Iron-Nickel Meteorite Found in Gale Crater by Curiosity, in: Lunar and Planetary Science Conference, Lunar and Planetary Science Conference, 2017, p. 2258.

[63] P. Y. Meslin, D. Wellington, R. C. Wiens, J. R. Johnson, J. Van Beek, O. Gasnault, V. Sautter, I. Maroger, J. Lasue, P. Beck, J. C. Bridges, B. Cohen, J. W. Ashley, A. G. Fairén, H. Newsom, A. Cousin, O. Forni, F. Calef, W. Rapin, S. Maurice, B. Chide, S. Schröder, W. Goetz, N. Mangold, T. Gabriel, N. Lanza, P. Pinet, Diversity and Areal Density of Iron-Nickel Meteorites Analyzed by Chemcam in Gale Crater, in: Lunar and Planetary Science Conference, Lunar and Planetary Science Conference, 2019, p. 3179.

[64] W. S.A., Data compilation for USGS reference material BHVO-2, Hawaiian Basalt, U.S. Geol. Surv. Open File Rep (1997).

[65] C. C. Allen, R. V. Morris, K. M. Jager, D. C. Golden, D. J. Lindstrom, M. M. Lindstrom, J. P. Lockwood, Martian Regolith Simulant JSC Mars-1, in: Lunar and Planetary Science Conference, Lunar and Planetary Science Conference, 1998, p. 1690.

[66] S. Terashima, A. Osui, N. Imai, TWO NEW GSJ GEOCHEMICAL REFERENCE SAMPLES: SYENITE JSY-1 AND MANGANESE NODULE JMN-1, Geostandards Newsletter 19 (1995) 221–229. doi:https://doi.org/10.1111/j.1751-908X.1995.tb00160.x.

[67] C. Chaleard, P. Mauchien, N. Andre, J. Uebbing, J. L. Lacour, C. Geertsen, Correction of matrix effects in quantitative elemental analysis with laser ablation optical emission spectrometry, J. Anal. At. Spectrom. 12 (1997) 183–188. doi:10.1039/A604456E.

[68] P. Y. Meslin, P. Gasda, J. L'Haridon, O. Forni, N. Lanza, S. Lamm, J. R. Johnson, R. C. Wiens, L. Thompson, W. Rapin, O. Gasnault, A. Cousin, N. Mangold, E. Dehouck, S. Maurice, J. Frydenvang, J. Lasue, Detection of Hydrous Manganese and Iron Oxides with Variable Phosphorus and Magnesium Contents in the Lacustrine Sediments of the Murray Formation, Gale, Mars, in: Lunar and Planetary Science Conference, Lunar and Planetary Science Conference, 2018, p. 1447.

[69] N. L. Lanza, W. W. Fischer, R. C. Wiens, J. Grotzinger, A. M. Ollila, A. Cousin, R. B. Anderson, B. C. Clark, R. Gellert, N. Mangold, S. Maurice, S. Le Mouélic, M. Nachon, M. Schmidt, J. Berger, S. M. Clegg, O. Forni, C. Hardgrove, N. Melikechi, H. E. Newsom, V. Sautter, High manganese concentrations in rocks at Gale crater, Mars, 41 (2014) 5755–5763. doi:10.1002/2014GL060329.

[70] N. L. Lanza, R. C. Wiens, R. E. Arvidson, B. C. Clark, W. W. Fischer, R. Gellert, J. P. Grotzinger, J. A. Hurowitz, S. M. McLennan, R. V. Morris, M. S. Rice, J. F. Bell, J. A. Berger, D. L. Blaney, N. T. Bridges, F. Calef, J. L. Campbell, S. M. Clegg, A. Cousin, K. S. Edgett, C. Fabre, M. R. Fisk, O. Forni, J. Frydenvang, K. R. Hardy, C. Hardgrove, J. R. Johnson, J. Lasue, S. Le Mouélic, M. C. Malin, N. Mangold, J. Martın-Torres, S. Maurice, M. J. McBride, D. W. Ming,

H. E. Newsom, A. M. Ollila, V. Sautter, S. Schröder, L. M. Thompson, A. H. Treiman, S. VanBommel, D. T. Vaniman, M.-P. Zorzano, Oxidation of manganese in an ancient aquifer, Kimberley formation, Gale crater, Mars, 43 (2016) 7398–7407. doi:10.1002/2016GL069109.

[71] S. Cady, J. Farmer, Fossilization processes in siliceous thermal springs: Trends in preservation along thermal gradients (1996).

[72] P. B. Niles, D. C. Catling, G. Berger, E. Chassefière, B. L. Ehlmann, J. R. Michalski, R. Morris, S. W. Ruff, S. Brad, Geochemistry of carbonates on mars: Implications for climate history and nature of aqueous environments, Space Science Review 174 (2013) 301–328. doi:https://doi.org/10.1007/s11214-012-9940-y.

[73] J. L. Bandfield, T. D. Glotch, P. R. Christensen, Spectroscopic identification of carbonate minerals in the martian dust, Science 301 (2003) 1084–1087. doi:10.1126/science.1088054.

[74] R. V. Morris, S. W. Ruff, R. Gellert, D. W. Ming, R. E. Arvidson, B. C. Clark, D. C. Golden, K. Siebach, G. Klingelhöfer, C. Schröder, I. Fleischer, A. S. Yen, S. W. Squyres, Identification of carbonate-rich outcrops on mars by the spirit rover, Science 329 (2010) 421–424. doi:10.1126/science.1189667.

[75] B. Sutter, A. C. McAdam, P. R. Mahaffy, D. W. Ming, K. S. Edgett, E. B. Rampe, J. L. Eigenbrode, H. B. Franz, C. Freissinet, J. P. Grotzinger, A. Steele, C. H. House, P. D. Archer, C. A. Malespin, R. Navarro-González, J. C. Stern, J. F. Bell, F. J. Calef, R. Gellert,

D. P. Glavin, L. M. Thompson, A. S. Yen, Evolved gas analyses of sedimentary rocks and eolian sediment in Gale Crater, Mars: Results of the Curiosity rover's sample analysis at Mars instrument from Yellowknife Bay to the Namib Dune, Journal of Geophysical Research (Planets) 122 (2017) 2574–2609. doi:10.1002/2016JE005225.

[76] P. D. Archer, E. Rampe, B. Clarck, V. Tu, B. Sutter, D. Vaniman, H. Franz, A. McAdam, Detection Of Siderite (FeCO3) In Glen Torridon Samples By The Mars Science Laboratory Rover, in: Lunar and Planetary Science Conference, Lunar and Planetary Science Conference, 2020, p. 2709.

[77] P. Beck, O. Forni, J. Lasue, E. Lewin, A. Cousin, S. Maurice, P. Y. Meslin, W. Rapin, O. Gasnault, R. C. Wiens, N. Mangold, V. Sautter, P. Coll, C. Szopa, T. Dequaire, J. G. Blank, Carbon Detection with ChemCam: Laboratory Studies and Mars Results, in: Lunar and Planetary Science Conference, Lunar and Planetary Science Conference, 2016, p. 1826.

[78] P. Beck, A. Fau, P. Y. Meslin, O. Forni, J. Lasue, E. Lewin, A. Cousin, S. Maurice, W. Rapin, O. Gasnault, R. C. Wiens, N. Mangold, V. Sautter, P. Coll, C. Szopa, T. Dequaire, B. Garcia, S. Schwartz, Searching for Carbon on Mars with MSL/ChemCam, in: Lunar and Planetary Science Conference, Lunar and Planetary Science Conference, 2017, p. 1216.

[79] E. S. Amador, J. L. Bandfield, N. H. Thomas, A search for minerals associated with serpentinization across mars us-

ing crism spectral data, Icarus 311 (2018) 113 – 134. doi:https://doi.org/10.1016/j.icarus.2018.03.021.

[80] L. Gomez-Nubla, J. Aramendia, G. Arana, F. Rull, A. Cousin, S. Fedez-Ortiz de Vallejuelo, K. Castro, M. Maguregui, J. A. Manrique, G. Lopez-Reyes, J. M. Madariaga, J. Medina, V. Garcia-Baonza, J. Laserna, S. Maurice, R. Wiens, Evaluation of the Elemental and Molecular Homogeneity of the Supercam Calibration Targets, in: Lunar and Planetary Science Conference, Lunar and Planetary Science Conference, 2018, p. 2813.

[81] B. E. e. a. J. Skok, J. Mustard, Silica deposits in the nili patera caldera on the syrtis major volcanic complex on mars, Nature Geosciences 3 (2010) 838–841. doi:https://doi.org/10.1038/ngeo990.

[82] R. Milliken, G. Swayze, R. Arvidson, J. Bishop, R. Clark, B. Ehlmann, R. Green, J. Grotzinger, R. Morris, S. Murchie, J. Mustard, C. Weitz, Opaline silica in young deposits on Mars, Geology 36 (2008) 847–850. doi:10.1130/G24967A.1.

[83] Mars reconnaissance orbiter observations of light-toned layered deposits and associated fluvial landforms on the plateaus adjacent to valles marineris, Icarus 205 (2010) 73 – 102. doi:https://doi.org/10.1016/j.icarus.2009.04.017, mRO/HiRISE Studies of Mars.

[84] M. Rice, J. Bell, E. Cloutis, A. Wang, S. Ruff, M. Craig, D. Bailey, J. Johnson, P. de Souza, W. Farrand, Silica-rich deposits and

hydrated minerals at gusev crater, mars: Vis-nir spectral characterization and regional mapping, Icarus 205 (2010) 375 – 395. doi:https://doi.org/10.1016/j.icarus.2009.03.035.

[85] A. Brown, M. Walter, T. Cudahy, Short-wave infrared reflectance investigation of sites of paleobiological interest: Applications for mars exploration, Astrobiology 4 (2004) 359–376. doi:10.1089/ast.2004.4.359, pMID: 15383240.

[86] S. L. Cady, J. R. Skok, V. G. Gulick, J. A. Berger, N. W. Hinman, Chapter 7 - siliceous hot spring deposits: Why they remain key astrobiological targets, in: N. A. Cabrol, E. A. Grin (Eds.), From Habitability to Life on Mars, Elsevier, 2018, pp. 179 – 210. doi:https://doi.org/10.1016/B978-0-12-809935-3.00007-4.

[87] S. McMahon, T. Bosak, J. P. Grotzinger, R. E. Milliken, R. E. Summons, M. Daye, S. A. Newman, A. Fraeman, K. H. Williford, D. E. G. Briggs, A field guide to finding fossils on mars, Journal of Geophysical Research: Planets 123 (2018) 1012–1040. doi:https://doi.org/10.1029/2017JE005478.

[88] N. Olivier, G. Dromart, N. Coltice, N. Flament, P. Rey, R. Sauvestre, A deep subaqueous fan depositional model for the palaeoarchaean (3.46 ga) marble bar cherts, warrawoona group, western australia, Geological Magazine 149 (2012) 743–749. doi:10.1017/S0016756812000131.

[89] A. Gendrin, N. Mangold, J.-P. Bibring, Y. Langevin, B. Gondet, F. Poulet, G. Bonello, C. Quantin, J. Mustard, R. Arvidson,

S. Le Mouélic, Sulfates in Martian Layered Terrains: The OMEGA/Mars Express View, Science 307 (2005) 1587–1591. doi:10.1126/science.1109087.

[90] J.-P. Bibring, Y. Langevin, A. Gendrin, B. Gondet, F. Poulet, M. Berthé, A. Soufflot, R. Arvidson, N. Mangold, J. Mustard, P. Drossart, OMEGA Team, S. Erard, O. Forni, M. Combes, T. Encrenaz, T. Fouchet, R. Merchiorri, G. Belluci, F. Altieri, V. Formisano, G. Bonello, F. Capaccioni, P. Cerroni, A. Coradini, S. Fonti, V. Kottsov, N. Ignatiev, V. Moroz, D. Titov, L. Zasova, M. Mangold, P. Pinet, S. Douté, B. Schmitt, C. Sotin, E. Hauber, H. Hoffmann, R. Jaumann, U. Keller, T. Duxbury, F. Forget, Mars Surface Diversity as Revealed by the OMEGA/Mars Express Observations, Science 307 (2005) 1576–1581. doi:10.1126/science.1108806.

[91] B. L. Ehlmann, C. S. Edwards, Mineralogy of the Martian Surface, Annual Review of Earth and Planetary Sciences 42 (2014) 291–315. doi:10.1146/annurev-earth-060313-055024.

[92] R. E. Milliken, J. P. Grotzinger, B. J. Thomson, Paleoclimate of Mars as captured by the stratigraphic record in Gale Crater, 37 (2010) L04201. doi:10.1029/2009GL041870.

[93] M. Nachon, S. M. Clegg, N. Mangold, S. Schröder, L. C. Kah, G. Dromart, A. Ollila, J. R. Johnson, D. Z. Oehler, J. C. Bridges, S. Le Mouélic, O. Forni, R. C. Wiens, R. B. Anderson, D. L. Blaney, J. F. Bell, B. Clark, A. Cousin, M. D. Dyar, B. Ehlmann, C. Fabre,

O. Gasnault, J. Grotzinger, J. Lasue, E. Lewin, R. Léveillé, S. McLennan, S. Maurice, P. Y. Meslin, W. Rapin, M. Rice, S. W. Squyres, K. Stack, D. Y. Sumner, D. Vaniman, D. Wellington, Calcium sulfate veins characterized by ChemCam/Curiosity at Gale crater, Mars, Journal of Geophysical Research (Planets) 119 (2014) 1991–2016. doi:10.1002/2013JE004588.

[94] M. Nachon, N. Mangold, O. Forni, L. C. Kah, A. Cousin, R. C. Wiens, R. Anderson, D. Blaney, J. G. Blank, F. Calef, S. M. Clegg, C. Fabre, M. R. Fisk, O. Gasnault, J. P. Grotzinger, R. Kronyak, N. L. Lanza, J. Lasue, L. Le Deit, S. L. Mouélic, S. Maurice, P. Y. Meslin, D. Z. Oehler, V. Payré, W. Rapin, S. Schröder, K. Stack, D. Sumner, Chemistry of diagenetic features analyzed by ChemCam at Pahrump Hills, Gale crater, Mars, 281 (2017) 121–136. doi:10.1016/j.icarus.2016.08.026.

[95] R. E. Kronyak, L. C. Kah, N. B. Miklusicak, K. S. Edgett, V. Z. Sun, A. B. Bryk, R. M. E. Williams, Extensive Polygonal Fracture Network in Siccar Point group Strata: Fracture Mechanisms and Implications for Fluid Circulation in Gale Crater, Mars, Journal of Geophysical Research (Planets) 124 (2019) 2613–2634. doi:10.1029/2019JE006125.

[96] W. Rapin, P.-Y. Meslin, S. Maurice, D. Vaniman, M. Nachon, N. Mangold, S. Schroeder, O. Gasnault, O. Forni, R. Wiens, G. Martinez, A. Cousin, V. Sautter, J. Lasue, E. Rampe, D. Archer, Hydration state of calcium sulfates in gale crater, mars: Identification of bassan-

ite veins, Earth and Planetary Science Letters 452 (2016) 197 – 205. doi:https://doi.org/10.1016/j.epsl.2016.07.045.

[97] E. Rampe, D. Blake, T. Bristow, D. Ming, D. Vaniman, R. Morris, C. Achilles, S. Chipera, S. Morrison, V. Tu, A. Yen, N. Castle, G. Downs, R. Downs, J. Grotzinger, R. Hazen, A. Treiman, T. Peretyazhko, D. Des Marais, R. Walroth, P. Craig, J. Crisp, B. Lafuente, J. Morookian, P. Sarrazin, M. Thorpe, J. Bridges, L. Edgar, C. Fedo, C. Freissinet, R. Gellert, P. Mahaffy, H. Newsom, J. Johnson, L. Kah, K. Siebach, J. Schieber, V. Sun, A. Vasavada, D. Wellington, R. Wiens, Mineralogy and geochemistry of sedimentary rocks and eolian sediments in gale crater, mars: A review after six earth years of exploration with curiosity, Geochemistry 80 (2020) 125605. doi:https://doi.org/10.1016/j.chemer.2020.125605.

[98] W. Rapin, B. Ehlmann, G. Dromart, J. Schieber, N. Thomas, W. Fischer, V. Fox, N. Stein, M. Nachon, B. Clark, L. Kah, L. Thompson, H. Meyer, T. Gabriel, C. Hardgrove, N. Mangold, F. Rivera-Hernandez, R. Wiens, A. Vasavada, An interval of high salinity in ancient gale crater lake on mars (2019).

[99] A. E. P. Douce, M. F. Roden, J. Chaumba, C. Fleisher, G. Yogodzinski, Compositional variability of terrestrial mantle apatites, thermodynamic modeling of apatite volatile contents, and the halogen and water budgets of planetary mantles, Chemical Geology 288 (2011) 14 – 31. doi:https://doi.org/10.1016/j.chemgeo.2011.05.018.

[100] F. M. McCubbin, A. Smirnov, H. Nekvasil, J. Wang, E. Hauri, D. H.

Lindsley, Hydrous Magmatism on Mars: A Source for Water on the Ancient Martian Surface and the Current Martian Subsurface?, in: Lunar and Planetary Science Conference, Lunar and Planetary Science Conference, 2009, p. 2207.

[101] F. M. McCubbin, S. M. Elardo, C. K. Shearer Jr., A. Smirnov, E. H. Hauri, D. S. Draper, A petrogenetic model for the comagmatic origin of chassignites and nakhlites: Inferences from chlorine-rich minerals, petrology, and geochemistry, Meteoritics & Planetary Science 48 (2013) 819–853. doi:https://doi.org/10.1111/maps.12095.

[102] J. Filiberto, A. H. Treiman, The effect of chlorine on the liquidus of basalt: First results and implications for basalt genesis on mars and earth, Chemical Geology 263 (2009) 60–68. doi:https://doi.org/10.1016/j.chemgeo.2008.08.025.

[103] O. Forni, M. Gaft, M. J. Toplis, S. M. Clegg, S. Maurice, R. C. Wiens, N. Mangold, O. Gasnault, V. Sautter, S. Le Mouélic, P.-Y. Meslin, M. Nachon, R. E. McInroy, A. M. Ollila, A. Cousin, J. C. Bridges, N. L. Lanza, M. D. Dyar, First detection of fluorine on Mars: Implications for Gale Crater's geochemistry, 42 (2015) 1020–1028. doi:10.1002/2014GL062742.

[104] O. Forni, P. Y. Meslin, A. Cousin, S. M. Clegg, N. Mangold, L. Le Deit, O. Gasnault, G. David, M. Nachon, D. Blaney, H. Newson, S. Maurice, R. C. Wiens, M. Gaft, Fluorine on Mars: Seven Years of Detection with ChemCam On-Board MSL, LPI Contributions 2089 (2019) 6095.

[105] P. R. Christensen, M. B. Wyatt, T. D. Glotch, A. D. Rogers, S. Anwar, R. E. Arvidson, J. L. Band field, D. L. Blaney, C. Budney, W. M. Calvin, A. Fallacaro, R. L. Fergason, N. Gorelick, T. G. Graff, V. E. Hamilton, A. G. Hayes, J. R. Johnson, A. T. Knudson, H. Y. McSween, G. L. Mehall, L. K. Mehall, J. E. Moersch, R. V. Morris, M. D. Smith, S. W. Squyres, S. W. Ruff, M. J. Wolff, Mineralogy at Meridiani Planum from the Mini-TES Experiment on the Opportunity Rover, Science 306 (2004) 1733–1739. doi:10.1126/science.1104909.

[106] S. W. Squyres, R. E. Arvidson, J. F. Bell, J. Brückner, N. A. Cabrol, W. Calvin, M. H. Carr, P. R. Christensen, B. C. Clark, L. Crumpler, D. J. Des Marais, C. d'Uston, T. Economou, J. Farmer, W. Farrand, W. Folkner, M. Golombek, S. Gorevan, J. A. Grant, R. Greeley, J. Grotzinger, L. Haskin, K. E. Herkenhoff, S. Hviid, J. Johnson, G. Klingelhöfer, A. H. Knoll, G. Landis, M. Lemmon, R. Li, M. B. Madsen, M. C. Malin, S. M. McLennan, H. Y. McSween, D. W. Ming, J. Moersch, R. V. Morris, T. Parker, J. W. Rice, L. Richter, R. Rieder, M. Sims, M. Smith, P. Smith, L. A. Soderblom, R. Sullivan, H. Wänke, T. Wdowiak, M. Wolff, A. Yen, The Opportunity Rover's Athena Science Investigation at Meridiani Planum, Mars, Science 306 (2004) 1698–1703. doi:10.1126/science.1106171.

[107] M. Biesuz, V. M. Sglavo, Flash sintering of ceramics, Journal of the European Ceramic Society 39 (2019) 115 – 143. doi:https://doi.org/10.1016/j.jeurceramsoc.2018.08.048.

[108] G. Cao, C. Estournes, J. Garay, R. Orru, Spark Plasma Sintering:

Current Status, New Developments and Challenges, Elsevier Science, 2019.

[109] M. Nygren, Z. Shen, Spark plasma sintering: Possibilities and limitations, in: Euro Ceramics VIII, volume 264 of *Key Engineering Materials*, Trans Tech Publications Ltd, 2004, pp. 719–724. doi:10.4028/www.scientific.net/KEM.264-268.719.

[110] R. Chaim, G. Chevallier, A. Weibel, C. Estournes, Grain growth during spark plasma and flash sintering of ceramic nanoparticles: a review, Journal of Materials Science 53 (2018). doi:10.1007/s10853-017-1761-7.

[111] C. Maniere, U. Kus, G. Chevallier, A. Weibel, L. Durand, J. Huez, D. Delagnes, C. EstournÃšs, Chapter 3 - how to overcome the main challenges of sps technology: Reproducibility, multi-samples and elaboration of complex shapes, in: G. Cao, C. Estournes, J. Garay, R. Orra (Eds.), Spark Plasma Sintering, Elsevier, 2019, pp. 77 – 108. doi:https://doi.org/10.1016/B978-0-12-817744-0.00003-9.

[112] Z. A. Munir, U. Anselmi-Tamburini, M. Ohyanagi, The effect of electric field and pressure on the synthesis and consolidation of materials: A review of the spark plasma sintering method, Journal of Materials Science 41 (2006). doi:10.1007/s10853-006-6555-2.

[113] A. Cousin, O. Forni, S. Maurice, O. Gasnault, C. Fabre, V. Sautter, R. Wiens, J. Mazoyer, Laser induced breakdown spectroscopy library for the martian environment, Spectrochim-

ica Acta Part B: Atomic Spectroscopy 66 (2011) 805 – 814. doi:https://doi.org/10.1016/j.sab.2011.10.004.

[114] R. Wiens, S. Maurice, J. Lasue, O. Forni, R. Anderson, S. Clegg, S. Bender, D. Blaney, B. Barraclough, A. Cousin, L. Deflores, D. Delapp, M. Dyar, C. Fabre, O. Gasnault, N. Lanza, J. Mazoyer, N. Melikechi, P.-Y. Meslin, H. Newsom, A. Ollila, R. Perez, R. Tokar, D. Vaniman, Pre-flight calibration and initial data processing for the chemcam laser-induced breakdown spectroscopy instrument on the mars science laboratory rover, Spectrochimica Acta Part B: Atomic Spectroscopy 82 (2013) 1 – 27. doi:https://doi.org/10.1016/j.sab.2013.02.003.

[115] G. C, Concentration and dependency ratios, Rivista di Politica Economica 87 (1997) 769–789.

[116] P. Comon, Independent Component Analysis, in: J-L.Lacoume (Ed.), Higher-Order Statistics, Elsevier, 1992, pp. 29–38.

[117] P. Comon, Independent component analysis, a new concept?, Signal Processing 36 (1994) 287 – 314. doi:https://doi.org/10.1016/0165-1684(94)90029-9, higher Order Statistics.

[118] O. Forni, S. Maurice, O. Gasnault, R. C. Wiens, A. Cousin, S. M. Clegg, J.-B. Sirven, J. Lasue, Independent component analysis classification of laser induced breakdown spectroscopy spectra, Spectrochimica Acta Part B: Atomic Spectroscopy 86 (2013) 31 – 41. doi:https://doi.org/10.1016/j.sab.2013.05.003.

[119] S. Potin, O. Brissaud, P. Beck, B. Schmitt, Y. Magnard, J.-J. Correia, P. Rabou, L. Jocou, Shadows: a spectro-gonio radiometer for bidirectional reflectance studies of dark meteorites and terrestrial analogs: design, calibrations, and performances on challenging surfaces, Appl. Opt. 57 (2018) 8279–8296. doi:10.1364/AO.57.008279.

[120] N. Bonnefoy, Développement d'un spectrophoto-goniomètre pour l'étude de la réflectance bidirectionnelle de surfaces géophysiques : application au soufre et perspectives pour le satellite Io, Ph.D. thesis, 2001. Thèse de doctorat dirigée par Schmitt, Bernard Physique Grenoble 1 2001.

[121] E. A. Cloutis, M. J. Gaffey, Pyroxene spectroscopy revisited: Spectral-compositional correlations and relationship to geothermometry, Journal of Geophysical Research: Planets 96 (1991) 22809–22826. doi:https://doi.org/10.1029/91JE02512.

[122] C. E. Viviano, J. E. Moersch, H. Y. McSween, Implications for early hydrothermal environments on mars through the spectral evidence for carbonation and chloritization reactions in the nili fossae region, Journal of Geophysical Research: Planets 118 (2013) 1858–1872. doi:https://doi.org/10.1002/jgre.20141.

[123] O. Beyssac, M. Gauthier, A. Fau, S. Bernard, K. Benzerara, M. Morand, P. Rosier, P. Y. Meslin, S. Maurice, SuperCam Science Team, Nanosecond Time-Resolved Raman and Fluorescence Spectroscopy: Insights for Mineral and Organics Characterization, in: Lu-

nar and Planetary Science Conference, Lunar and Planetary Science Conference, 2017, p. 1545.

[124] A. Fau, O. Beyssac, M. Gauthier, P. Meslin, A. Cousin, K. Benzerara, S. Bernard, J. Boulliard, O. Gasnault, O. Forni, R. Wiens, M. Morand, P. Rosier, Y. Garino, S. Pont, S. Maurice, Pulsed laser-induced heating of mineral phases: Implications for laser-induced breakdown spectroscopy combined with raman spectroscopy, Spectrochimica Acta Part B: Atomic Spectroscopy 160 (2019) 105687. doi:https://doi.org/10.1016/j.sab.2019.105687.

[125] F. M. . D. L. . G. Y. Jones, R. H. ; McCubbin, Phosphate Minerals in Type 4-6 LL Chondrites: The Nature of Fluids on the LL Chondrite Parent Body, in: Lunar and Planetary Science Conference, Lunar and Planetary Science Conference, 2011, p. 2464.

[126] F. M. . G. Y. Jones, R. H. ; McCubbin, Phosphate Mineralogy and the Role of Fluids in the Zag H Chondrite , in: Lunar and Planetary Science Conference, Lunar and Planetary Science Conference, 2011, p. 2435.

[127] F. M. McCubbin, A. Steele, E. H. Hauri, H. Nekvasil, S. Yamashita, R. J. Hemley, Nominally hydrous magmatism on the moon, Proceedings of the National Academy of Sciences 107 (2010) 11223–11228. doi:10.1073/pnas.1006677107.

[128] F. M. McCubbin, B. L. Jolliff, H. Nekvasil, P. K. Carpenter, R. A. Zeigler, A. Steele, S. M. Elardo, D. H. Lindsley, Flu-

orine and chlorine abundances in lunar apatite: Implications for heterogeneous distributions of magmatic volatiles in the lunar interior, Geochimica et Cosmochimica Acta 75 (2011) 5073–5093. doi:https://doi.org/10.1016/j.gca.2011.06.017.

[129] F. M. McCubbin, M. A. Riner, K. E. Vander Kaaden, L. K. Burkemper, Is mercury a volatile-rich planet?, Geophysical Research Letters 39 (2012). doi:https://doi.org/10.1029/2012GL051711.

[130] A. R. Santos, C. B. Agee, F. M. McCubbin, C. K. Shearer, Z. D. Sharp, M. Zimmer, Apatite and Merrillite from Martian Meteorite NWA 7034, in: Lunar and Planetary Science Conference, Lunar and Planetary Science Conference, 2013, p. 2601.

[131] P. Y. Meslin, J. R. Johnson, O. Forni, P. Beck, A. Cousin, J. Bridges, W. Rapin, B. Cohen, H. Newsom, V. Sautter, E. Lewin, M. Nachon, R. C. Wiens, V. Payré, O. Gasnault, S. Maurice, A. G. Fairén, S. Schröder, N. Mangold, N. Thomas, Egg Rock Encounter: Analysis of an Iron-Nickel Meteorite Found in Gale Crater by Curiosity, in: Lunar and Planetary Science Conference, Lunar and Planetary Science Conference, 2017, p. 2258.

[132] G. David, A. Cousin, O. Forni, P.-Y. Meslin, E. Dehouck, N. Mangold, J. L'Haridon, W. Rapin, O. Gasnault, J. R. Johnson, A. M. Ollila, A. R. Newell, M. Salvatore, T. S. J. Gabriel, R. C. Wiens, S. Maurice, Analyses of high-iron sedimentary bedrock and diagenetic features observed with chemcam at vera rubin ridge, gale crater, mars: Calibration and characterization, Journal of Geophysical Research: Planets 125

(2020) e2019JE006314. doi:https://doi.org/10.1029/2019JE006314, e2019JE006314 2019JE006314.

[133] G. David, A. Cousin, O. Forni, P.-Y. Meslin, E. Dehouck, N. Mangold, J. L'Haridon, W. Rapin, O. Gasnault, J. R. Johnson, A. M. Ollila, A. R. Newell, M. Salvatore, T. S. J. Gabriel, R. C. Wiens, S. Maurice, Analyses of high-iron sedimentary bedrock and diagenetic features observed with chemcam at vera rubin ridge, gale crater, mars: Calibration and characterization, Journal of Geophysical Research: Planets 125 (2020) e2019JE006314. doi:https://doi.org/10.1029/2019JE006314.